An Investigation into the Use of Scattered Photons to Improve 2D Positron Emission Tomography (PET) Functional Imaging Quality

by

Hongyan Sun

A Thesis submitted to the Faculty of Graduate Studies of

The University of Manitoba

in partial fulfillment of the requirements for the degree of

DOCTOR OF PHILOSOPHY

Department of Physics and Astronomy

University of Manitoba

Winnipeg, Manitoba

ABSTRACT

Positron emission tomography (PET) is a powerful metabolic imaging modality, which is designed to detect two anti-parallel 511 keV photons origniating from a positron-electron annihilation. However, it is possible that one or both of the annihilation photons undergo a Compton scattering in the object. This is more serious for a scanner operated in 3D mode or with large patients, where the scatter fraction can be as high as 40-60%. When one or both photons are scattered, the line of response (LOR) defined by connecting the two relevant detectors no longer passes through the annihilation position. Thus, scattered coincidences degrade image contrast and compromise quantitative accuracy. Various scatter correction methods have been proposed but most of them are based on estimating and subtracting the scatter from the measured data or incorporating it into an iterative reconstruction algorithm.

By accurately measuring the scattered photon energy and taking advantage of the kinematics of Compton scattering, two circular arcs (TCA) in 2D can be identified, which describe the locus of all the possible scattering positions and encompass the point of annihilation. In the limiting case where the scattering angle approaches zero, the TCA approach the LOR for true coincidences. Based on this knowledge, a Generalized Scatter (GS) reconstruction algorithm has been developed in this thesis, which can use both true and scattered coincidences to extract the activity distribution in a consistent way. The annihilation position within the TCA can be further confined by adding a patient outline as a constraint into the GS algorithm. An attenuation correction method for the scattered coincidences was also developed in order to remove the imaging artifacts. A geometrical

model that characterizes the different probabilities of the annihilation positions within the TCA was also proposed. This can speed up image convergence and improve reconstructed image quality. Finally, the GS algorithm has been adapted to deal with non-ideal energy resolutions. In summary, an algorithm that implicitly incorporates scattered coincidences into the image reconstruction has been developed. Our results demonstrate that this eliminates the need for scatter correction and can improve system sensitivity and image quality.

CONTRIBUTIONS

This thesis presents the implementation of the scattering reconstruction project in PET systems developed by the Medical Physics group at University of Manitoba. The original idea of this work was developed by my supervisor, Dr. Stephen Pistorius. The author, as the lead investigator in this work, has solely accomplished the contributions listed below:

- Setting up simulations and collecting data, developing the reconstruction algorithms for reconstructing the activity distribution from scattered coincidences in 2D non-time-of-flight (non-TOF) PET, as well as analyzing results;
- Evaluating the feasibility and developing the algorithms for reconstructing the electron density map from scattered coincidences in PET;
- Introducing the patient outline as a constraint into the scattering reconstruction algorithm to further improve the image quality;
- Developing the attenuation correction methods for the GS reconstruction algorithms;
- Characterizing the different probability of the annihilation positions within TCA and introducing this map into the imaging reconstruction;
- Developing the methods for implementing the proposed reconstruction algorithms in the non-ideal energy resolution scenarios.

Timothy Van Beek has kindly provided his ray tracing code in developing the attenuation correction methods. Dr. Andrew Goertzen, Dr. Harry Ingleby, and Mohammadreza Teimoorisichani also have provided some technical issues and good suggestions.

ACKNOWLEDGEMENTS

First, I would like to express my deepest gratitude to my supervisor Dr. Stephen Pistorius for taking me as his student. His insightful guidance and advice have made substantial differences in my work, as well as in my life. This dissertation would not have been possible without his guidance, input, patience, dedication and encouragement. It is his vision that stimulated the development of this exciting project.

I would also like to thank Dr. Stephen Pistorius, Dr. Andrew L. Goertzen, Dr. Francis Lin, Dr. Sherif Sherif, and Dr. Roger Lecomte from Université de Sherbrooke, for serving on my committee and for their time, support, and helpful advice during my research and academic development.

I would also like to thank the entire Division of Medical Physics, CancerCare Manitoba, special thanks to Alana Dahlin and Luanne Scott for their assistance in my graduate study.

I would also like to thank the Department of Physics and Astronomy, University of Manitoba, especially to Susan Beshta, Wanda Klassen, Christine McInnis, and Maiko Langelaar for their support in my graduate study.

I would also like to express my appreciation to all present and former fellow students in Medical Physics at University of Manitoba for their constant suggestions and friendship, including Dr. Jorge Alpuche, Dr. Krista Chytyk, Tamar Chighvinadze, Dr. Ganiyu Asuni, Dr. Fazal Ur-Rehman, Troy Teo, Mike Hebb, Heather Champion, Peter McCowan, Bryan McIntosh, Mohammadreza Teimoorisichani, Graham Schellenberg, Geng Zhang, Hongwei Sun, Azeez Omotayo, Pawel Siciarz, Parandoush Abbasian and Princess Anusionwu.

I am very grateful to Dr. Norm Davison, Noella Rosenthal for their generous assistance, which made my new life in Winnipeg much easier.

I would like to extend my deepest gratitude to my parents Yupeng Sun and Shu'ai Feng, and my family for their encouragement, inspiration and support through the years.

Finally, I would like to acknowledge the sources of funding that I had over these years, these including CancerCare Manitoba Foundation, the University of Manitoba.

To my beloved parents

LIST OF ABBREVIATIONS

APD	Avalanche Photo Diode
CdTe	Cadmium-tellurium
CRC	Contrast recovery coefficient
CT	Computed Tomography
E-PDF	Energy probability density function
FBP	Filtered Backprojection
FDG	^{18}F-fluorodeoxyglucose
FOV	Field of view
FORE	Fourier rebinning
FWHM	Full width at half maximum
GATE	Geant4 Application for Emission Tomography
G-APD	Geiger-mode Avalanche Photo Diode
GPU	Graphics processing unit
GS	Generalized Scatter
GSO	Gadolinium oxyorthosilicate
GTM	Geometric transfer matrix
$LaBr_3$:Ce	Cerium-doped lanthanum bromide
LOR	Line of response
LSO	Lutetium oxy-orthosilicate
LYSO	Lutetium-yttrium oxyorthosilicate
MC	Monte Carlo
MLEM	Maximum-likelihood expectation maximization
MRI	Magnetic resonance imaging
NEMA	National Electrical Manufacturers Association

OSEM	Ordered Subset expectation maximization
PET	Positron emission tomography
PHA	Pulse height analyzer
PMTs	Photo-multiplier tubes
PSF	Point spread function
QE	Quantum Efficiency
ROI	Region of interest
RSD	Relative standard deviation
SI	The International System of Units
SNR	Signal to noise ratio
SPECT	Single photon emission Computed Tomography
SSRB	Single slice rebinning algorithm
SSS	Single-scatter simulation
TCA	Two circular arcs
TOF	Time of flight
US	Ultrasound

TABLE OF CONTENTS

LIST OF FIGURES

LIST OF TABLES

Chapter 1: Rationale

Various non-invasive diagnostic imaging modalities, such as computed tomography (CT), ultrasound (US), magnetic resonance imaging (MRI), single photon emission computed tomography (SPECT), and positron emission tomography (PET), can provide anatomical and/or functional information about the object being scanned. PET, which evolved from traditional planar nuclear medicine, was developed around the unique decay characteristic of radionuclides known as positron emitters (e.g.^{11}C, ^{13}N, ^{15}O, ^{18}F, ^{64}Cu, etc.). These radionuclides can be produced in a cyclotron and then used to label compounds of biological interest. These positron labeled radiopharmaceuticals are usually injected intravenously into the patients, which will concentrate within the body based on the metabolic activity being explored. The principle of PET is based on the simultaneous detection of two 511 keV anti-parallel photons produced when an emitted positron loses its kinetic energy and annihilates with an electron. If the photons produced by such an annihilation do not interact, the annihilation position can be found along the straight line known as the line of response (LOR), defined by connecting the position of the two detectors that record the annihilation photons.

Current clinical application of PET, almost exclusively with ^{18}F-fluorodeoxyglucose (FDG) at present, is being used in three important areas of clinical diagnosis and management [1]: 1) Cancer diagnosis and management, since PET can provide an earlier diagnosis and more accurate staging of malignant diseases than can conventional anatomical imaging modalities; 2) Cardiology and cardiac surgery [2], and 3) Neurology and psychiatry [3]. Figure 1.1 gives an example of a PET scanner and PET/CT images for a thyroid cancer patient. As shown in this figure, the tumor can be localized in PET images while this information has been obscured in the CT images.

(a)

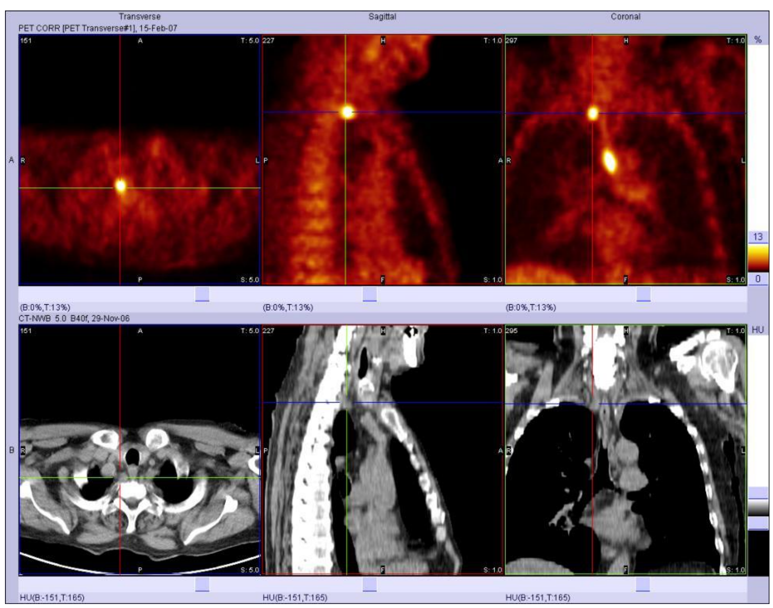

(b)

Figure 1.1 (a) Siemens Biograph 16 PET/CT Scanner; (b) 50 years old female patient with thyroid cancer. (Upper: PET image. Lower: CT image.) (Figure 1.1 (b) courtesy of Dr. A. L. Goertzen, University of Manitoba)

When a positron annihilates in the body, it is possible that one or both of the photons from the same annihilation undergo a Compton scatter interaction in the body or in the detectors. The scatter fraction typically ranges from about 10-20% in 2D mode with slice-defining septa. This issue becomes more serious for 3D tomography or for large patients, where the scatter fraction can be as high as 40-60% [4-6].

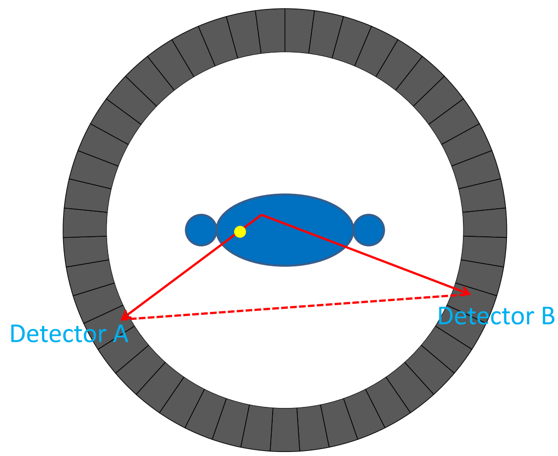

Figure 1.2 A diagram of a Compton scattering event in the patient. The two annihilation photons are generated at the yellow dot with one photon observed at A, the other undergoes a Compton scattering and is observed at B.

When one or both of the annihilation photons scatter, the defined LOR is no longer collinear with the site of annihilation and the real activity distribution is misrepresented as shown in Figure 1.2. If an image is reconstructed without effective scatter correction, there will be an apparent migration of activity from hot to cold regions, and this results in a loss of resolution and image contrast. Scattered coincidences, which are generally taken as noise in the conventional PET imaging reconstruction algorithms, degrade image contrast and compromise quantitative accuracy. Thus, various approaches for estimating and correcting scattered events from the measured data have been proposed [4, 7-9].

These approaches can be broadly classified into four categories: 1) empirical approaches; 2) multiple-energy-windows (or spectral-analytic) approaches [10-16]; 3) convolution/deconvolution-based approaches [17, 18]; 4) simulation-based scatter correction approaches [19-25]. Most of these techniques are based on estimating and subtracting the scatter from the measured data or incorporated it in the projector of an iterative reconstruction algorithm. Inaccuracy in the estimation of the scatter sinogram will introduce significant biases in the activity distribution [6]. The subtraction based correction methods destroy the Poisson nature of the data, reduce the system's sensitivity and amplify image noise [4].

The limited spatial resolution (~6-8 mm) of PET images, as well as a lack of anatomic context, makes attenuation correction and the interpretation of the precise location of the radiotracer, difficult. Attenuation corrections can be carried out using simplistic and often inaccurate approaches or by coupling the PET to an x-ray CT or MRI system [26, 27]. Although the combination of PET and CT is used in commercial scanners, PET-CT has several limitations. Its main drawback is that the imaging is performed sequentially rather than simultaneously, which may introduce artifacts when registering the functional and anatomical imaging content. In addition, radiation dose to patients is increased because of the CT scanning. Combining PET and MRI is challenging, as the detectors used in the conventional PET systems are sensitive to the magnetic fields, and it is difficult to relate MRI images to the coefficients required to correct for attenuation of the PET annihilation photons.

Improvements in PET detector technology make it feasible to use the energy of individual photon in the imaging reconstruction process. The energy of the detected photons carries some probabilistic information about the spatial distribution of the annihilation positions. By taking advantage of the photon energy and the kinematics of Compton scattering, the scattered coincidences can be used to extract the PET activity distribution and build an anatomical map. To achieve these goals, this scattering reconstruction project intends to develop methods to estimate the activity distribution and to build an anatomical map from scattered coincidences. This thesis will focus on developing, optimizing and evaluating a 2D Generalized Scatter (GS) reconstruction algorithm to extract activity distribution. The approach to build an anatomical map from scattered coincidences is given in Appendix A.

The second chapter of this thesis will provide the physics background needed for this project. Chapter 3 evaluates the feasibility of reconstructing PET images from scattered coincidences in a 2D simulated small animal PET system with ideal energy resolution. Chapter 4 investigates further improvements to PET image quality by adding a patient/phantom outline as a constraint in the GS algorithm. Chapter 5 develops the attenuation correction method for the scattered coincidences in the PET GS reconstruction algorithm. Chapter 6 describes a geometrical model to characterize the different probabilities of annihilation positions associated with scattered coincidences based on Monte-Carlo (MC) simulations. Chapter 7 explores the dependency of the image quality on the energy resolution, and adapts the proposed method for non-ideal energy resolution scenarios. The final chapter summarizes and concludes this work and identifies future areas of research.

Chapter 2: Introduction to Positron Emission Tomography

The successful development of the PET system would be impossible without the innovations from various fields, including physics, engineering, and biology. In the 1950's, a group at the Massachusetts General Hospital finished the first development of PET technology and the demonstration of annihilation radiation for medical imaging. In the late 1950s, David E. Kuhl, Luke Chapman, and Roy Edwards introduced the concept of emission and transmission tomography. The early design of a PET system consisting of two 2-dimenional detector arrays was completed and reported in the late 1960s and the early 1970s. To maximize the efficiency of detecting annihilation photons, the ring system design was proposed by James Robertson and Zang-Hee Cho and became the prototype of the current geometry for PET scanners. The development of positron emission radiopharmaceuticals by the Brookhaven group has expanded the scope of PET imaging rapidly [28].

The protocol for generating a PET image is firstly to inject a positron emitting radiopharmaceutical into the patient. The labeled radionuclides are unstable and prone to emit a positron to achieve a more stable state. PET is designed to detect the two annihilation photons that are created when the positron loses its kinetic energy and combines with an electron. The measured coincidences are processed and reconstructed by a computer to generate the activity distributions. This process is illustrated in Figure 2.1.

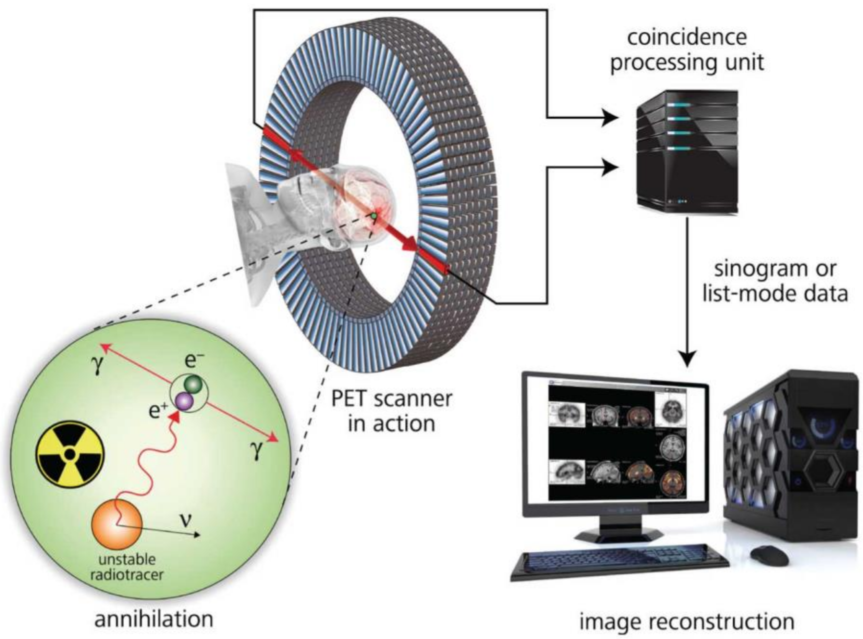

Figure 2.1 Schema of a PET imaging acquisition process.

(http://www.sepscience.com/Sectors/Pharma/Articles/429-/Radio-IC-for-Quality-Control-in-PET Diagnostics)

This chapter introduces the physical principles behind positron decay and annihilation, radiation interactions and detection, data processing, and tomographic imaging reconstruction principles. An overview of the physical principles, basic features and performance parameters of nuclear medicine instrumentation, and the practical issues can be found in [1, 29, 30].

2.1 Positron decay and Annihilation

The atom is a basic unit of matter that consists of a dense central nucleus surrounded by a cloud of negatively charged electrons each with a mass of 9.11×10^{-31} kg and an electric charge of 1.6×10^{-19} Coulomb (C). The nucleus is generally composed of positively charged protons (each with a mass of 1.67×10^{-27} kg (or 938.27 MeV) and an electric charge of 1.6×10^{-19} C) and electrically neutral neutrons (each with a mass of 1.67×10^{-27} kg (or 939.57 MeV) and an electric charge of 0 C). When a nucleus has either an excess number of protons or neutrons, it is unstable and prone to decay and reach a more stable configuration by changing the number of protons or neutrons. The amount of activity of a radionuclide can be characterized by the number of decays per unit time. The unit of radioactive activity in the International System of Units (SI) is the becquerel (Bq), which is defined as one transformation (or decay or disintegration) per second. An older unit of radioactivity is the Curie (Ci), which is equal, by definition, to a disintegration rate of 3.7×10^{10} Bq, so that 1 Ci=3.7×10^{10} Bq. The nuclei spontaneously undergo radioactive decay in an exponential fashion given by the decay equation:

$$N(t) = N_0 e^{-\lambda t} \ldots\ldots\ldots\ldots\ldots\ldots(2.1)$$

where N_0 is the initial number of active radionuclides, $N(t)$ is the number of radionuclides at time t, and λ is the decay constant. The decay constant can be related to the half-life ($T_{1/2}$), which is the time it takes for the activity of a given amount of a radioactive substance to decay to half of its initial value, as following:

$$\lambda = \frac{ln2}{T_{1/2}} = \frac{0.693}{T_{1/2}} \ldots\ldots\ldots\ldots\ldots\ldots(2.2)$$

Among the various kinds of radionuclide decay, one common mechanism for a proton-rich atom X to achieve stability is by converting a proton into a neutron and ejecting a positron ${}^{0}_{1}\beta^{+}$, which is the antiparticle to the electron with the same mass but opposite electric charge.

$${}^{A}_{Z}X \rightarrow {}_{Z-1}^{\;\;\,A}Y + {}^{0}_{1}\beta^{+} + v + Q \ldots\ldots\ldots\ldots\ldots(2.3)$$

where v is a neutrino and Q is the energy. This energy will be shared between the daughter nucleus, the positron, and the neutrino. Therefore, the energy of the emitted positron ranges from zero up to a maximum endpoint energy E_{max}. This endpoint energy corresponds to the mass difference between the parent and the daughter nucleus as required by the conservation of energy. The average energy of the emitted positrons is approximately 1/3 of the maximum energy E_{max} [30]. Table 2.1 shows a selected list of these radionuclides that commonly decay by positron emission and encountered in relation to PET imaging. This table also contains the maximum ranges R_{max} for the emitted positrons, and the root mean square ranges R_{rms} [31]. The β^+ branching ratio is the percentage of total decays resulting in positron emission instead of electron capture.

Table 2.1 A list of radionuclides that decay by positron emission and are relevant to PET imaging [31].

Radionuclide	$T_{1/2}$	E_{max} (MeV)	R_{max} (mm)	R_{rms} (mm)	β^+ branching ratio (%)
^{11}C	20.4 min	0.96	3.9	0.4	99
^{13}N	9.97 min	1.20	5.1	0.6	100
^{15}O	122 s	1.73	8.0	0.9	100
^{18}F	109.8 min	0.63	2.3	0.2	97
^{22}Na	2.60 y	0.55	15	1.6	98
^{62}Cu	9.74 min	2.93	15	1.6	98
^{64}Cu	12.7 h	0.58	2.0	0.2	18
^{68}Ga	67.6 min	1.89	9.0	1.2	88
^{76}Br	16.2 h	3.7	19	3.2	54
^{82}Rb	1.27 min	3.38	18	2.6	95
^{86}Y	14.7 h	1.4	6.0	0.7	32
^{124}I	4.17 d	1.5	7.0	0.8	22

An alternate decay mode by which a proton-rich radionuclide can achieve a stable state is through electron capture, in which the nuclide absorbs an inner atomic electron, changes a nuclear proton into a neutron, and simultaneously causes the emission of an electron neutrino. Decay by positron emission and electron capture compete with one another, with positron emission usually being more likely in low Z nuclei, and electron capture being the dominant process in higher Z nuclei. This thesis will focus on the radionuclides that decay predominantly by positron emission, which is preferred for PET imaging.

Following a positron decay the ejected positron travels a short distance and loses most of its kinetic energy and combines with an electron and forms a positronium, which is a hydrogen-like state. This state is unstable, and the positronium will generate two antiparallel 511 keV photons after an average lifetime of 125 picoseconds. This process as illustrated in Figure 2.2 is called annihilation and forms the basis for PET imaging.

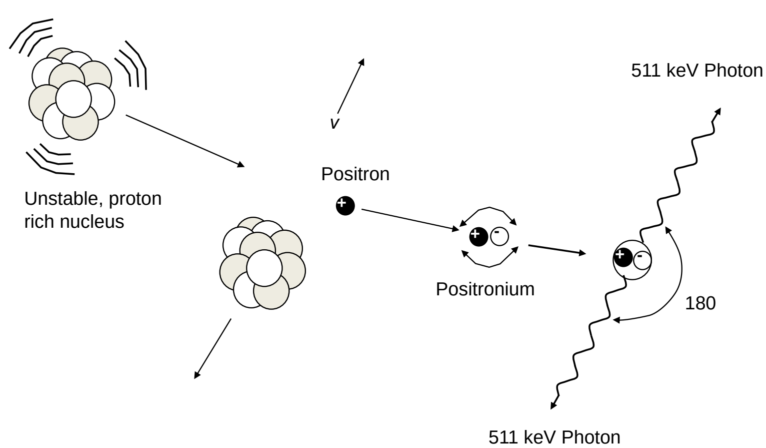

Figure 2.2 The diagram of positron emission and subsequent positron-electron annihilation resulting in generating two 511 keV antiparallel photons.

The high energy photons produced in the annihilation process gives some advantages for imaging in PET [29]. Firstly, these photons with high energy have a higher probability of escaping the body. Secondly, a precise anti-parallel relationship (referred to as electronic collimation) increases the detection efficiency leading to the capability of rapid tomographic imaging. Thirdly, all positron-emitting radionuclides, independent of the elements involved, can generate the same back-to-back 511 keV photons. However, this also limits the ability to perform simultaneous dual-radionuclide studies in PET.

A PET scanner is designed to detect these two anti-parallel annihilation photons simultaneously from which a straight line of response known as the LOR is used to localize the position of the radionuclide. However, the ability of PET imaging systems to accurately determine the source position is limited by two characteristics. The first of these characteristics is the positron range. Since the positron is emitted with non-zero kinetic energy, it will travel a tortuous path to dissipate this energy before annihilating with an electron as shown in Figure 2.3. The distance from the site of positron emission to the site of its annihilation is known as the positron range, which can be up to several millimeters. The effective positron range, or error due to the positron range, which is defined as the perpendicular distance from the emission site to the line defined by connecting the two annihilation photons, causes mis-positioning and blurring in the PET images.

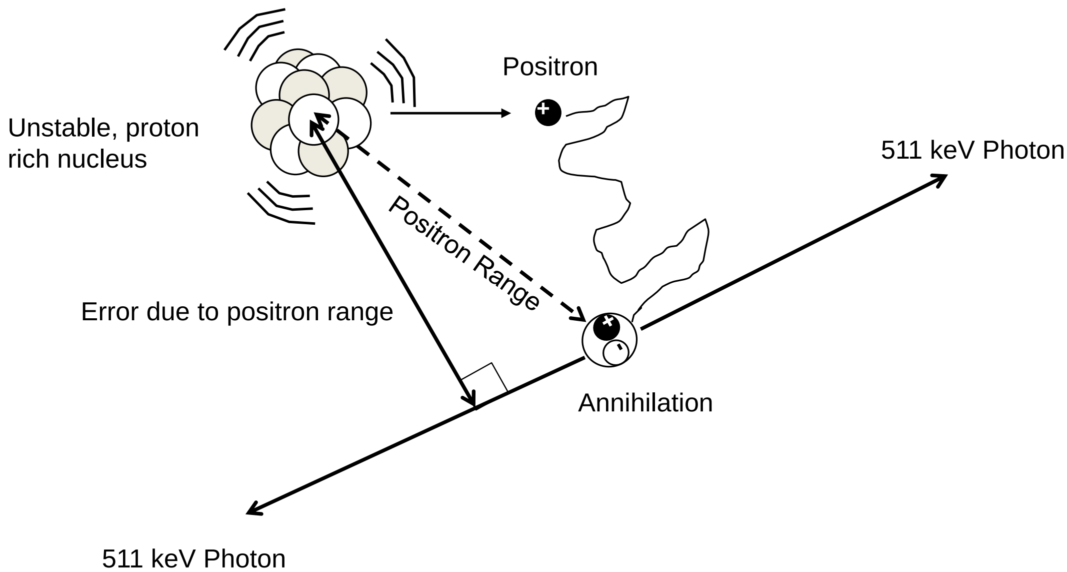

Figure 2.3 The process of positron emission and subsequent annihilation results in two 511 keV annihilation photons emitted. Since the positron is emitted with non-zero kinetic energy, it will travel in a tortuous path before annihilating with an electron. The distance from the positron emission site to the annihilation site is known as the positron range, which is dependent on the energy of the emitted positron.

The second effect is the non-colinearity that occurs when the positron and electron are not completely at rest when they annihilate. As a result, the law of conservation of momentum dictates that the two 511 keV photons will not be exactly 180^{o} apart, as is illustrated in Figure 2.4. Since the positron typically loses most of its kinetic energy before it can annihilate, this effect is independent of radionuclide and the initial energy of the positron. Statistically, the distribution of the emitted photons angles roughly fit a Gaussian function, with a full width at half maximum (FWHM) of 0.5^{o} [31, 32]. However, PET systems still assume the measured two annihilation photons with an exact back-to-back relationship, resulting in a small error in locating the line of annihilation.

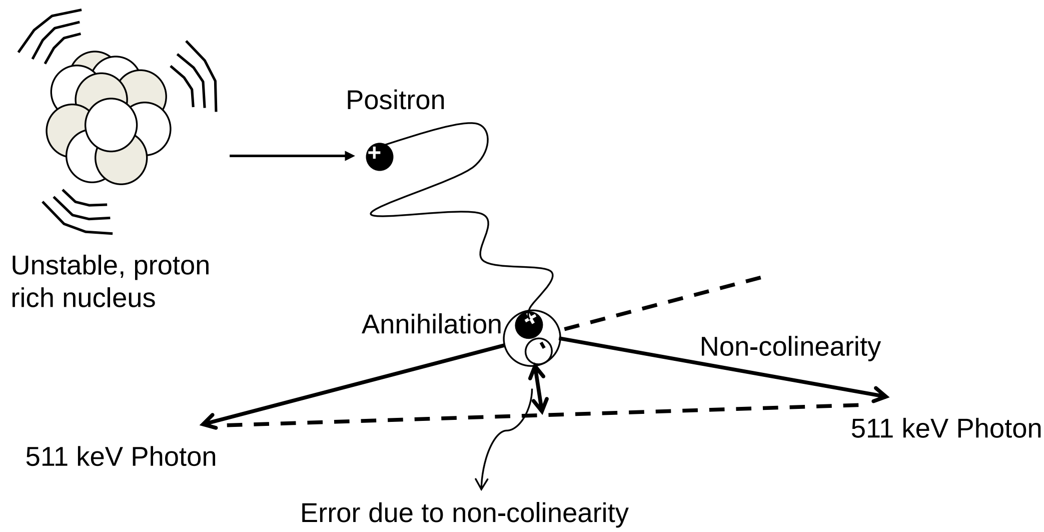

Figure 2.4 The diagram of non-colinearity of the two 511 keV annihilation photons emitted following a positron annihilating with an electron. Because of some residual momentum associated with the positron, the two annihilation photons are not emitted with exactly 180°, but with a small deviation.

2.2 Radiation Interactions and Attenuation

2.2.1 Radiation interactions

When the two 511 keV anti-parallel photons are generated following an annihilation, they will travel some distance in the object before being detected. In this process, they may interact with the surrounding substances. Depending on the energy of the electromagnetic radiation, high-energy photons interact with matter by three main mechanisms. They are (i) photoelectric effect, (ii) Compton scattering, and (iii) pair production. Other mechanisms such as coherent (Rayleigh) scattering, an interaction between a photon and a whole atom which predominates at energies less than 50 keV; triplet production and photonuclear reactions, where high energy gamma rays induce decay in the nucleus, and which require energies of greater than ~10 MeV, are not discussed here. This thesis will focus on the three main mechanisms, which dominate at the energies of interest in imaging in nuclear medicine.

Photoelectric Effect

The photoelectric effect is an interaction of photons with inner orbital electrons in an atom as illustrated in Figure 2.5. The photon transfers all of its energy to the electron, which is used by the electron to overcome the binding energy of the electron and the remaining energy is transferred to the electron as kinetic energy. When an outer orbital electron occupies the vacancy of the ejected electron, the differences in the binding energy lead to the emission of a characteristic X-ray or a second electron (Auger electron). The photoelectric effect dominates in human tissues at energies less than approximately 100 keV, which is particularly important for X-ray imaging, and photon detection. The probability of photoelectric interaction per unit distance strongly depends on the atomic number of the medium and is roughly proportional to Z^3 at 511 keV.

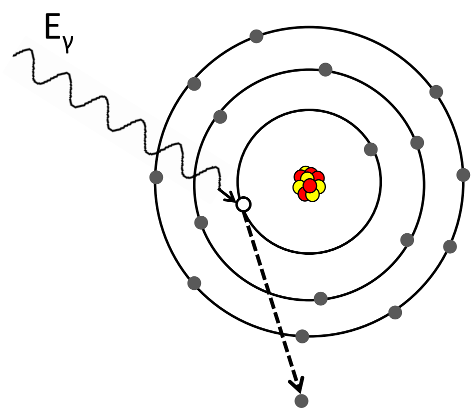

Figure 2.5 A schematic of the photoelectric effect. The incident photon transfers all of its energy to an inner shell electron, the electron then is ejected with some kinetic energy equal to the energy of the incident gamma ray diminished by the binding energy of the electron.

Compton Scattering

Compton scattering is the interaction between a photon and a loosely bound orbital electron as shown in Figure 2.6. The electron can be considered to be essentially free due to being so loosely connected to the atom.

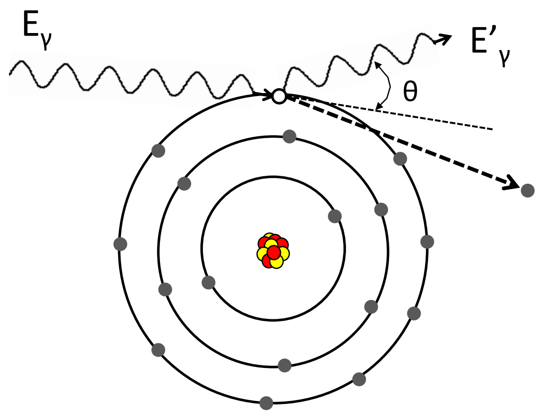

Figure 2.6 The schematic of Compton scattering in which the incident photon transfers part of its energy to an electron, deviating its initial direction, and the electron is ejected from the atom.

In this process, the photon transfers some of its energy to the electron and deviates from its initial direction, and the electron is ejected from the atom. The scattered photon energy (E_γ') can be related to the scattering angle ($\boldsymbol{\theta}$) by Compton equation:

$$E_\gamma' = \frac{E_\gamma}{1+\frac{E_\gamma}{m_e c^2}(1-\cos\theta)} \quad \text{................}(2.4)$$

where E_γ is the energy of the incoming photon, m_e is the electron rest mass and c is the speed of light (299,792,458 m/s). In terms of units of electron volts for energy, $m_e c^2$ equals to 511 keV.

The scattered photon energy as a function of the scattering angle for a primary photon with energy 511 keV is plotted in Figure 2.7.

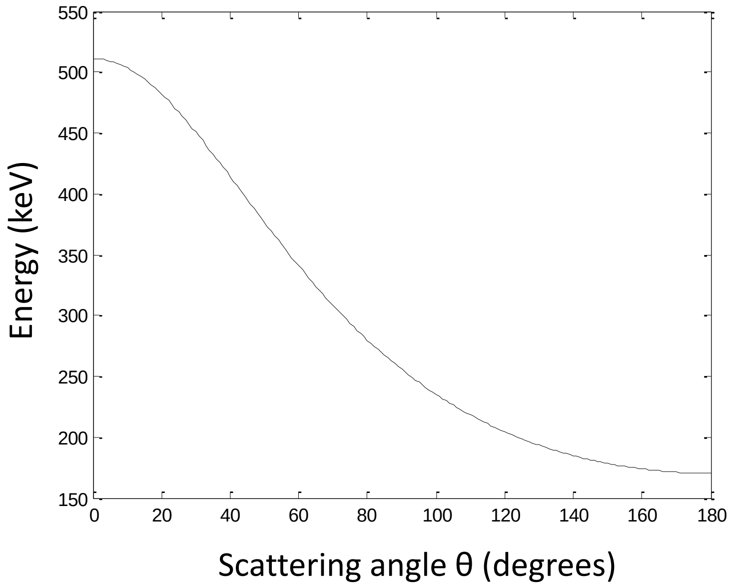

Figure 2.7 The scattered photon energy as a function of the scattering angle for an annihilation photon with a primary energy of 511 keV.

Compton scattering dominates in human tissue at energies above approximately 100 keV and less than ~2 MeV. This effect is not equally probable at all energies or scattering angles. The probability of Compton scattering per unit length of the absorbing medium is linearly proportional to the electron density of the medium. The angular distribution of the scatter photons is described by the Klein-Nishina equation as shown in Figure 2.8.

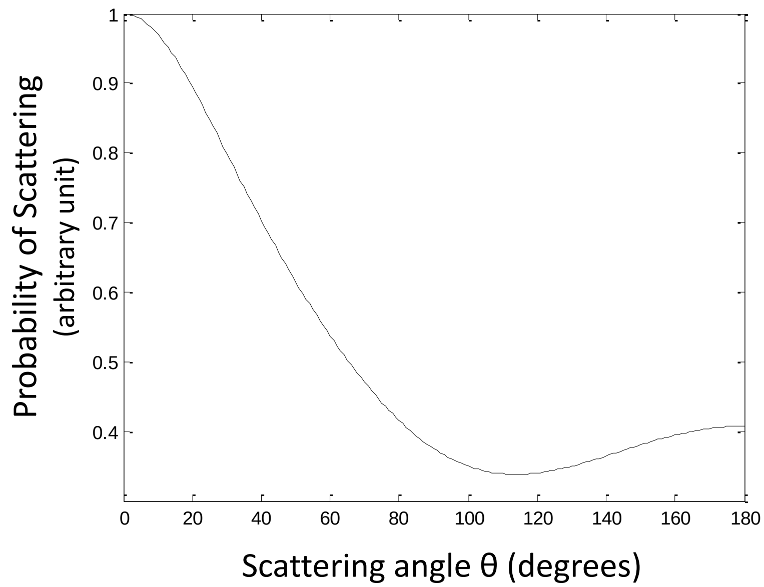

Figure 2.8 The angular probability distribution vs. the scattering angle for the 511keV annihilation photons.

Among the detected scattered events within a tissue-equivalent material in PET, Monte Carlo results have shown that more than 80% of the scattered photons have only undergone a single scattering interaction [1, 33].

Pair Production

In pair production, photons with an energy greater than 1.022 MeV will, in the vicinity of a nucleus, spontaneously convert to an e^-/e^+ pair as shown in Figure 2.9. Above the threshold of 1.022 MeV, the probability of pair production increases as the incident photon energy increases.

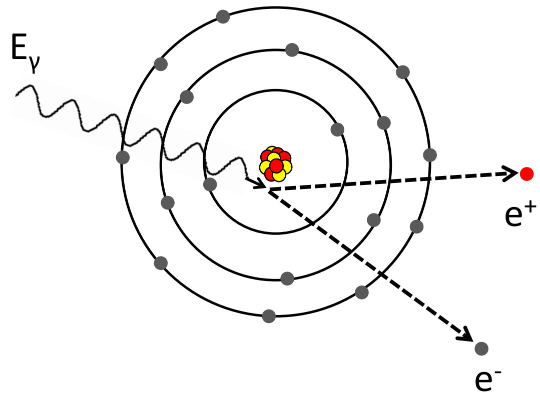

Figure 2.9 The schematic of pair production in which a photon passes in the vicinity of a nucleus and spontaneously forms a positron and an electron.

2.2.2 Photon attenuation

The aforementioned photon interactions with matter will lead to fewer photons being detected, caused by the phenomenon known as photon attenuation. The photon attenuation can take the form of a simple exponential relationship for a well-collimated source of photons and detector:

$$I_x = I_0 e^{-\mu x} \quad \ldots\ldots\ldots\ldots(2.5)$$

where I_0 and I_x refer respectively to the unattenuated and measured beam intensity after passing through a material of thickness x with the linear attenuation coefficient μ. The attenuation coefficient accounts for the probability per unit distance that an interaction will occur. For the 511 keV photons in PET, the attenuation coefficient is a function of the photon energy and the electron density of the medium, which is largely made up of components due to photoelectric absorption (τ) and Compton scattering (σ_C).

$$\mu \approx \tau + \sigma_C \quad \ldots\ldots\ldots\ldots\ldots(2.6)$$

The linear attenuation coefficient for some common materials at 140 keV and 511 keV are listed in Table 2.2.

Table 2.2 The linear attenuation coefficients for some common materials at 140 keV and 511 keV [1].

Material	Density (ρ) ($g.cm^{-3}$)	μ (140 keV) (cm^{-1})	μ (511 keV) (cm^{-1})
Adipose tissue	0.95	0.142	0.090
Water	1.0	0.150	0.095
Lung	1.05*	~0.04-0.06	~0.025-0.04
Smooth muscle	1.05	0.155	0.101
Perspex (Lucite)	1.19	0.173	0.112
Cortical bone	1.92	0.284	0.178
Pyrex glass	2.23	0.307	0.194
NaI(Tl)	3.67	2.23	0.34
Bismuth germanate (BGO)	7.13	~5.5	0.95
Lead	11.35	40.8	1.75

* This is the density of non-inflated lung.

As PET uses coincident detection to assign a LOR to describe the possible source position, a valid event should result in the simultaneous measurement of the two annihilation photons as shown in Figure 2.10.

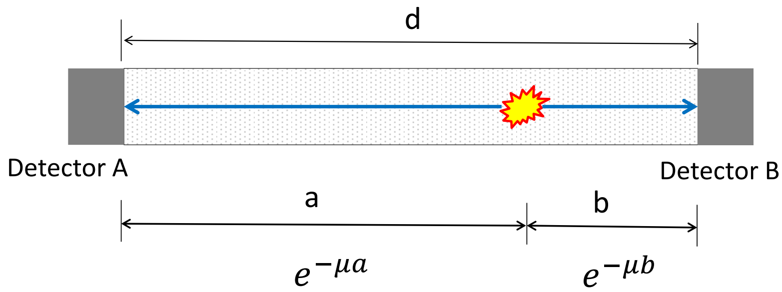

Figure 2.10 A successful coincident event in which the two annihilation photons are measured by Detector A and B respectively.

As shown in this figure, the probability P_a for an incident photon measured by Detector A from the source is $e^{-\mu a}$, and the probability P_b measured by Detector B is $e^{-\mu b}$. The coincident count rate C_t for the source with intensity C_0 is given by the product of the probability of measuring the two annihilation photons simultaneously:

$$C_t = C_0 P_a P_b = C_0 e^{-\mu a} e^{-\mu b} = C_0 e^{-\mu a} e^{-\mu(d-a)} = C_0 e^{-\mu d} \quad \text{.......(2.7)}$$

where d is the total thickness of the object. As shown in the Equation (2.7), the total count rate observed for a true coincidence is independent of the position of the source in the object, and only depends on the total thickness of the object.

2.3 Radiation detection

By making use of the interactions of the annihilation photons with matter, PET detectors measure the photons that escape from the object. The detectors convert the total energy lost or deposited by the high-energy photons into a measurable electrical signal or charge, as they pass through the detector. The integral of the signal is, therefore, proportional to the total energy deposited in the detector by the radiation. The ability of the radiation detector to accurately measure the deposited energy and provide precise information on the spatial location of the interaction as well as timing information is of importance for most of its uses.

Based on the different design and operating principles, radiation detectors can be classified into three broad categories: proportional (gas) chambers, semiconductor detectors, and scintillation detectors.

2.3.1 Proportional Chambers

The proportional chamber is a type of gaseous ionization detector, which can be used to measure the ionization produced by radiation as it passes through a gas chamber. To collect the particles of ionizing radiation, a high strength electric field is applied within this chamber to accelerate the electrons produced by the ionizing radiation. Subsequently, these highly energetic electrons collide with the neutral gas atoms resulting in secondary ionization. Hence, a cascade of electrons is eventually collected at the cathode after some initial energy deposition by the incident radiation. The disadvantage of these detectors for use in PET is the low density of the gas, leading to a reduced stopping efficiency for 511 keV photons, as well as poor energy resolution.

2.3.2 Semiconductor

Semiconductor or solid-state detectors are a class of radiation detectors, which consist of a *p-n* junction within such a device. When an incident photon strikes the detector, it may have sufficient energy to liberate electrons so that they are free to migrate within the crystal. The vacancy left behind by the electrons, known as holes, have the properties of a net positive charge. An applied electric field will then result in a flow of charge through the detector after the initial energy deposition by the photons. Semiconductor detectors have excellent energy resolution, but the low stopping efficiency for the 511 keV photons may limit their use in PET.

2.3.3 Scintillation detectors

The third category of radiation detector is a scintillation device, which forms the basis for almost all PET scanners in use today. These detectors consist of a dense crystalline scintillator material, which emits visible (scintillation) light photons after the interaction of photons within the scintillator. A photo-detector is used to detect and measure the number of scintillation photons emitted by an interaction, which is generally proportional to the energy deposited within the crystal.

Scintillator

The selection of a scintillator for PET detector application depends on its four main properties: 1) the stopping power for 511 keV photons, 2) signal decay time, 3) light output, and 4) the intrinsic energy resolution. The stopping power is the efficiency of a scintillator to stop (or absorb) a photon, which is characterized by the mean distance (attenuation length=$1/\mu$) before it undergoes an interaction . The stopping power of a scintillator depends on its density and the effective atomic number. Heavier nuclei will stop photons better than light nuclei. Besides, the photoelectric effect goes up with the Z-number as well. Crystals are often made from a few different elements. Denser materials have higher stopping power since they have more elements packed in the same amount of space. The decay constant is the time required for scintillation emission to decrease to e^{-1}

of its maximum, which affects the timing characteristics of the scanner. A short decay time is needed to process each pulse individually at high counting rates, as well as to reduce the number of random coincidences. Light output is the coefficient of conversion of ionizing radiation into light energy. A high-output scintillator can help achieve good spatial resolution with a high encoding ratio and attain good energy resolution. The energy resolution of a PET scanner depends on the scintillator light output as well as the intrinsic energy resolution of a scintillator. The intrinsic energy resolution arises due to inhomogeneities in the crystal growth process as well as non-uniform light output for interactions within it. Table 2.3 [1] lists some of the properties of scintillators that have application in PET.

Table 2.3 The Physical properties of commonly used scintillators in PET [1].

Property	Sodium iodide [NaI(TI)]	Bismuth Germanate (BGO)	Lutetium Oxyorthosilicate (LSO:Ce)	Yttrium Oxyorthosilicate (YSO:Ce)	Gadolinium Oxyorthosilicate (GSO:Ce)	Barium Fluoride (BaF_2)
Density (g/cm^3)	3.67	7.13	7.4	4.53	6.71	4.89
Effective Z	50.6	74.2	65.5	34.2	58.6	52.2
Attenuation length	2.88	1.05	1.16	2.58	1.43	2.2
Decay constant (ns)	230	300	40	70	60	0.6
Light output (photons/keV)	38	6	29	46	10	2
Relative light output to NaI(TI)	100%	15%	75%	118%	25%	5%
Wavelength (λ)	410	480	420	420	440	220
Intrinsic ΔE/E (%)	5.8	3.1	9.1	7.5	4.6	4.3
Energy resolution (%) at 511 keV	6.6	10.2	10	12.5	8.5	11.4
Index of refraction	1.85	2.15	1.82	1.8	1.91	1.56
Hygroscopic?	Yes	No	No	No	No	No
Rugged?	No	Yes	Yes	Yes	No	Yes
μ (cm^{-1}) at 511 keV	0.3411	0.9496	0.8658	0.3875	0.6978	0.4545
μ/ρ (cm^{-1}/gm) at 511 keV	0.0948	0.1332	0.117	0.853	0.104	0.0929

Photo-detector

A photo-detector is needed to convert the scintillation light into an electrical current. The photo-detectors used in PET scintillation detectors can be generally divided into two categories: 1) photo-multiplier tubes (PMTs) and 2) semiconductor-based photodiodes.

A PMT consists of a thin photocathode layer at the entrance window and a series of dynodes (electrodes) in an evacuated glass tube. Each of the dynodes is coated with an emissive material and held at a greater voltage with a resistor chain. An incoming scintillation photon deposits its energy at the photocathode and triggers the release of a photo-electron into the tube, and these electrons are accelerated by a potential difference to the first dynode. After acceleration, the electron with increased energy will lead to the emission of multiple secondary electrons. The process of acceleration and emission is then repeated through several dynodes structures lying at increasing potentials, leading to a gain of more than a million at the final dynode. This process is illustrated in Figure 2.11.

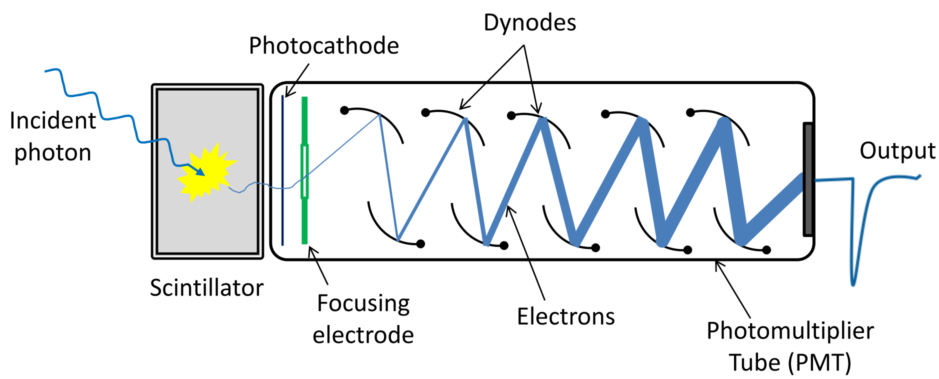

Figure 2.11 Schematic diagram of a photomultiplier tube in a PET scintillation detector.

This high gain obtained from a photomultiplier tube leads to a good signal-to-noise ratio (SNR) and is the primary reason for the success and applicability of photomultiplier tubes for use in scintillation detectors. The other advantages of photomultiplier tubes include their stability and ruggedness, and their fast response. The drawback of a photomultiplier tube is the low efficiency of the emission and the escape of photo-electrons from the cathode after the deposition of energy by a single scintillation photon. This property is called the Quantum Efficiency (QE) and is typically 25% for most of the photomultiplier tubes [1].

Photodiodes, on the other hand, also can be used to detect scintillation photons. Photodiodes are developed typically in the form of PIN diodes, where PIN refers to the three zones of the diode: P-type, Intrinsic, and N-type. Incident scintillation photons produce electron-hole pairs in the detector and an applied electric field then results in a charge flow, which can be measured through an external circuit. This semiconductor-based design has improved the detector's sensitivity for detecting the significantly lower energy scintillation photons. A significant drawback of the photodiode is the low SNR due to the thermally activated charge flow and low intrinsic signal amplification. The Avalanche Photo Diode (APD) is a type of photodiode that provides an internal amplification of the signal, thereby improving the SNR. Even though the gains have been amplified, they are still several orders of magnitude lower than the photomultiplier tube. The APD gains are also sensitive to small temperature variations, as well as to changes in the applied bias voltage. To overcome these drawbacks, a new variant of APD known as Geiger-mode APD (G-APD), which are specifically designed to operate with a reverse-bias voltage well above the breakdown voltage, have been developed. G-APDs are sensitive to single photons and, depending on the intrinsic setup, can have higher photon detection efficiency than PMTs. They are insensitive to magnetic fields and operate at a low voltage but with a high gain [34].

Block detector

The scintillator crystals can be arranged and coupled to photo-detectors for signal readout in a PET scanner in two main ways: one-to-one coupling or block detectors. In the one-to-one coupling design, a single crystal is glued to an individual photo-detector. The spatial resolution of this design is limited by the sizes of discrete crystal and PMTs. The inherent complexity and cost of such PET detectors limits their use, at present, to research tomography. Block detectors consist of a rectangular parallelepiped of scintillator, sectioned by partial saw cuts into discrete detector elements to which usually four PMTs are attached as shown in Figure 2.12.

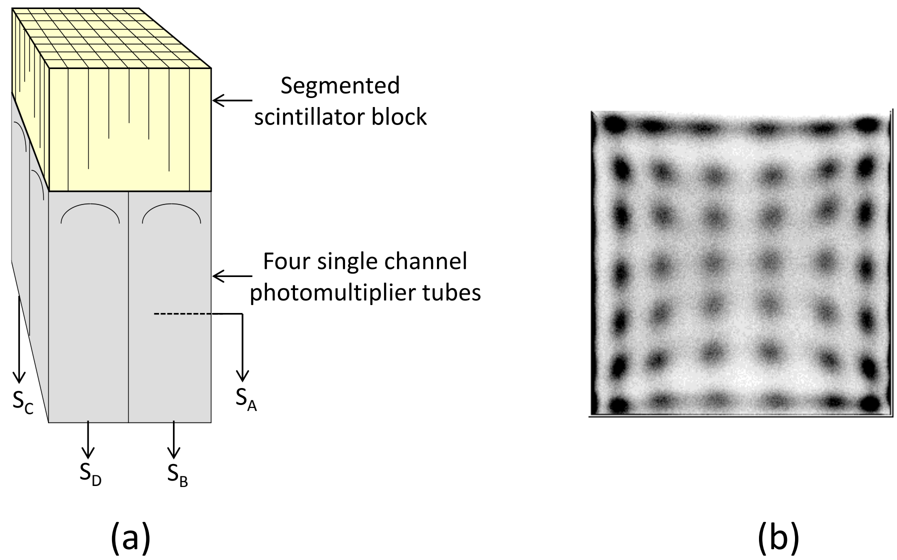

Figure 2.12 A schematic drawing of block detector. The scintillator is segmented into an 8×8 array with a unique saw cuts. By looking at the ratio of signals shared in these four PMTs, the detector element struck by the incident photon can be determined. (b) A flood histogram generated by irradiating the front surface of a block detector [29].

The scintillator crystals are cut with different depths to allow the scintillation light to be shared by varying degrees between the four PMTs, depending upon the position of the crystal in which the interaction took place. By comparing the intensities of signals in the four PMTs, the detector element (X, Y) struck by the incident photon can be calculated using:

$$X = \frac{S_A+S_B-S_C-S_D}{S_A+S_B+S_C+S_D} \quad\ldots\ldots\ldots\ldots\ldots\ldots\ldots (2.8a)$$

$$Y = \frac{S_A+S_C-S_B-S_D}{S_A+S_B+S_C+S_D} \quad\ldots\ldots\ldots\ldots\ldots\ldots\ldots (2.8b)$$

where S_A, S_B, S_C and S_D are the four PMT signals as shown in Figure 2.12 (a). The block detector is a cost-effective approach to the manufacture of a PET detector, as it allows 64 crystals or many more in newer systems to be decoded from four PMTs. A modification of the block design, called a quadrant-sharing block design, can accommodate smaller crystals by straddling a PMT over four block quadrants (see Figure 2.13). Compared with the standard block detector, this design can achieve a better spatial resolution with almost double the encoding ratio, but suffers from increased detector dead time due to the use of nine PMTs for signal readout from an event.

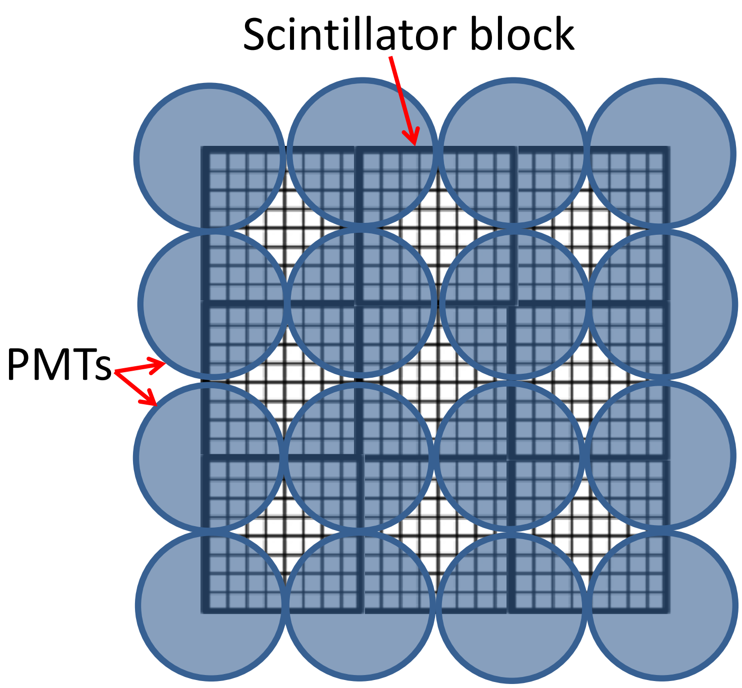

Figure 2.13 The quadrant sharing design as seen from the top through the crystals, which enables detector elements to be decoded using a smaller number of larger diameter PMTs.

2.3.4 PET scanner design

PET uses a pair of radiation detectors to simultaneously measure and identify two incident photons originating from the same annihilation (a coincidence). A straight line (or a tube) known as a Line of Response (LOR) can be defined by connecting the two photon detected positions to describe the possible annihilation position. To detect annihilation photons efficiently, most PET systems place a large number of detectors around the object to be imaged. A simple and low-cost PET scanner can be designed by using two opposing partial ring or large-area flat detectors. To improve overall detection efficiency, a modern PET scanner usually stacks several rings of detectors to create a stationary block ring design that extends 15 cm or more in the axial direction. Because PET systems with ring block detector geometry have become the dominant design, this thesis will focus on full ring PET systems in the following sections.

2.3.5 Coincidence detection

When an incident photon strikes a detector and deposits some or all of its energy, the detector will generate a signal. This signal is amplified by a signal amplifier and analyzed by the pulse height analyzer (PHA) to determine whether the energy of this signal is within the predefined energy window. The energy window used is closely related to the energy resolution of the detector, which is a function of the relative light output and the intrinsic energy resolution for a scintillation detector. A valid event will be passed to a coincidence processor and result in a trigger pulse, which marks the start of the coincidence window with a predetermined width 2τ (where τ is the pulse width). A coincidence (AND) circuit will be open and search for the other valid event during the length of the coincidence window. This process is illustrated in Figure 2.14.

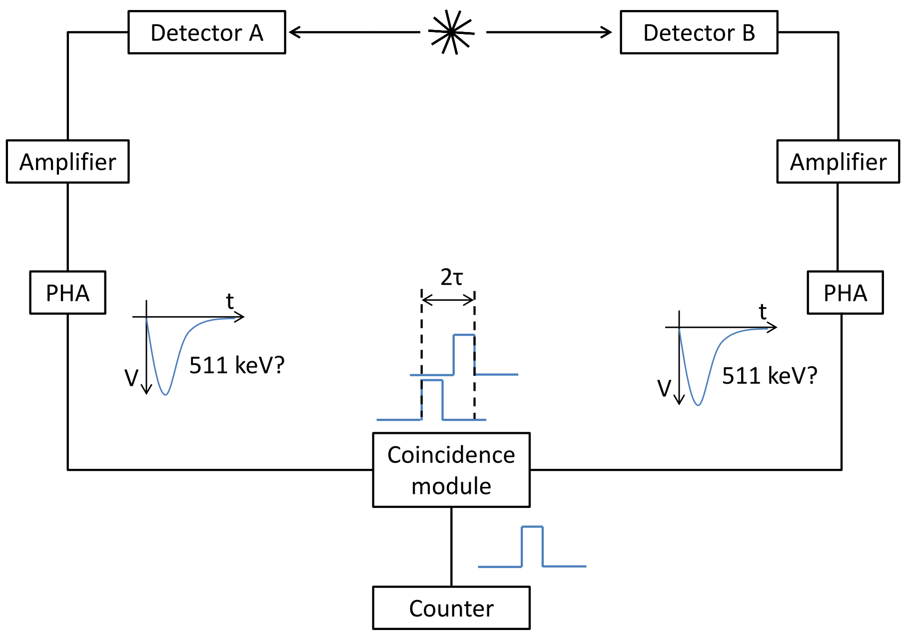

Figure 2.14 Diagram of a basic coincidence circuit. The two photons are observed by Detector A and Detector B individually, and then the two signals will be amplified by signal amplifiers and further processed by the pulse height analyzer to determine whether the energy within the predefined window. If the two pulses are still valid, they will go through the coincidence circuit to check whether these two pulses are measured within the time window (2τ), where τ is the pulse width.

The ability of the detectors to determine the time difference of the arrival of the annihilation photons, known as timing resolution, plays an important role because it affects the ability of the system to identify if two photons originate from a single coincident event. A PET scanner needs to detect two coincident photons emitted from anywhere within the scanner field of view (FOV). The selection of a coincidence timing window needs to consider the distance difference (and corresponding to the time difference) traveled by these two photons. Thus a typical timing window used in PET scanner is set to 2 to 3 times the time resolution (on the order of 2-6 ns), resulting in values ranging from 4 to 18 ns, so as to not reject annihilation photon pairs. With the advent of fast electronics and scintillators, time-of-flight (TOF) PET scanners can achieve a resolution of 0.5 ns or better, thus a much narrower time window (~4 ns) can be employed.

If two incident photons meet both the energy and timing criteria, the coincidence circuit will generate a logic pulse, which will be fed into a counter for registration of the coincidence. A valid coincident event will be written to a file in a list-mode or histogram mode. In list-mode, each coincidence will be individually written to a file, with the information about the measured positions, photon energies and time information of the two photon. In histogram mode, each LOR is assigned to a unique position in the sinogram space as indicated in Figure 2.15. Once a valid event is detected in a LOR, the corresponding position in the sinogram will be increased by one. This integrated number of events detected in each LOR provides an efficient manner to store the coincidences data.

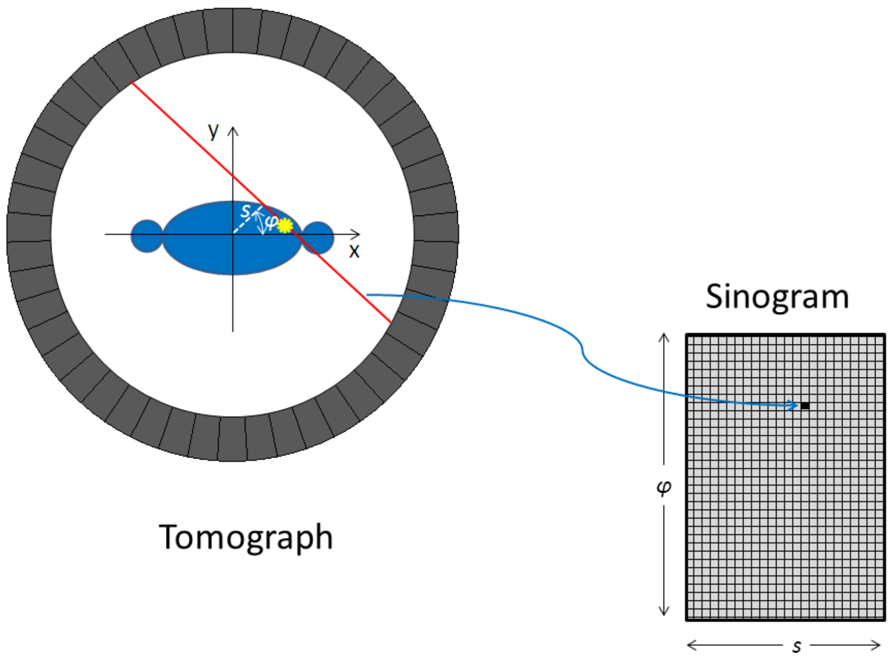

Figure 2.15 Schematic representations of a line projection and its corresponding point in the sinogram.

2.3. 6 Types of measured events

The premise of PET is to simultaneously detect two annihilation photons, derived from a single positron-electron annihilation, that do not interact significantly with surrounding atoms. This is referred to as a true coincidence. Only true coincidences provide the geometrical relationship obtained by assigning a line connecting the two detectors known as LOR, which pass through the annihilation positions. However, the non-ideal detectors used in PET lead to the measured events being contaminated with unwanted events, which includes scattered, random and multiple coincidences as shown in Figure 2.16. Scattered events arise when one or both of the photons from a single positron annihilation that are detected within the coincidence-timing window have undergone a Compton interaction. The Compton Effect causes the photon to lose some of its energy and deviates from its original direction. The inadequate energy resolution limits the system's ability to discriminate scattered events from true events, resulting in inconsistencies in the projection data and decreased contrast and inaccurate quantification of PET images. A random coincidence occurs when two nuclei decay at approximately the same time and only two of these four photons from different annihilations are counted and are considered to have come from the same positron annihilation while the other two are lost. Random coincidences are spatially uncorrelated with the distribution of the tracer. Multiple events are similar to random events, except that three photons from two or more annihilations are detected within the coincidence-timing window. Due to the ambiguity in deciding which two of these three photons are from the same annihilation, this kind of event is usually disregarded.

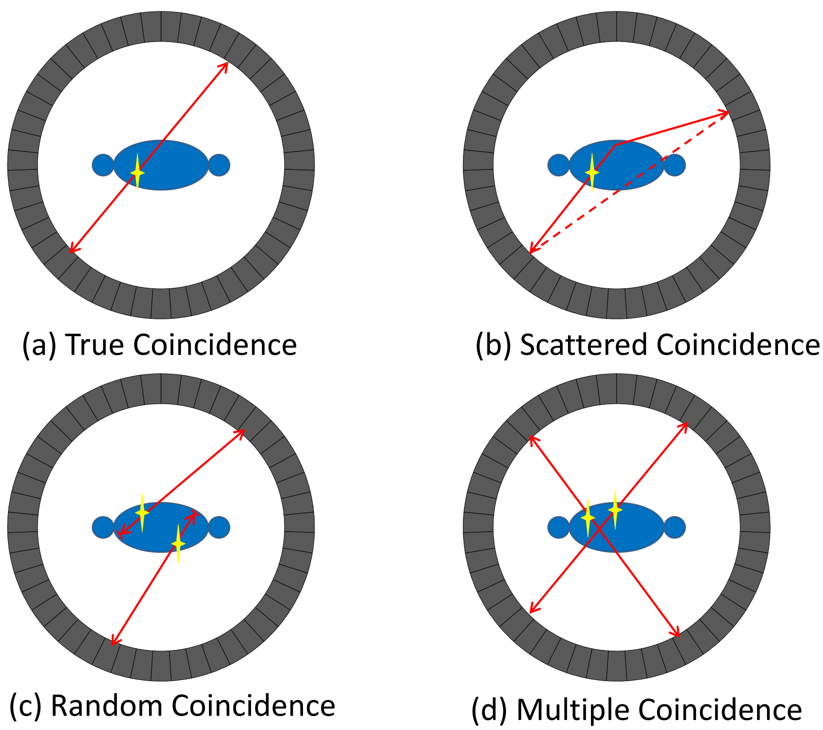

Figure 2.16 The various coincident events that can be recorded in PET are shown diagrammatically for a full-ring PET system.

The coincident events that meet the time and energy criteria and are measured by a PET scanner are called prompt coincidences, which includes true, scattered, and random coincidences. In a conventional PET reconstruction algorithm, the fraction of the scattered, and random events relative to the prompt events for each LOR need to be estimated and subtracted to yield the net true coincidences.

2.4 Data Corrections

To obtain quantitative accurate PET images, a number of sources of measurement errors in PET need to be corrected. These include the normalization, the involvement of random and scattered coincidences, the reduced measured counts due to photon attenuation, the dead time of detectors, and partial volume effect due to the signal dilution from small structures.

2.4.1 Normalization

Different LORs in a PET scanner have different sensitivities due to the variations in detector efficiency, geometrical variations (the different solid angle subtended), detector electronics, and summation of neighboring data elements. Figure 2.17 illustrates the effects of normalization on image uniformity. In order to reconstruct the quantitative accuracy and artefact-free images, these individual detector efficiencies as well as any geometrical efficiency variations should be measured and removed prior to reconstruction. The process of correcting these effects is known as normalization. The normalization correction methods can be classified into the direct normalization method and the component-based model method.

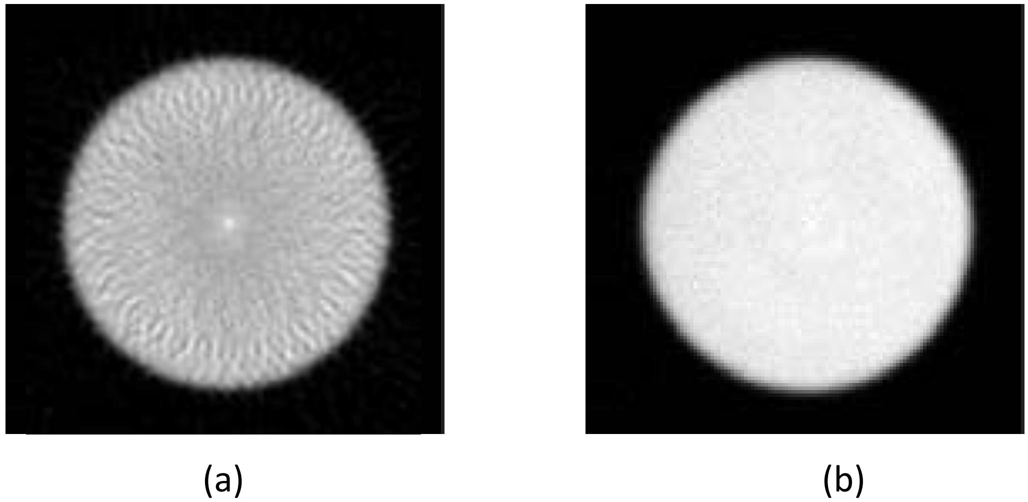

Figure 2.17 The effect of normalization on image uniformity of a uniform cylindrical source (a) without the normalization correction and (b) with the normalization correction [1].

The direct normalization is the simplest and most straightforward method to determine the normalization correction factors. Here all possible LORs are illuminated with a uniform plane source or rotating line source. This method can directly measure the relative variation in coincidence detection efficiencies between all the LORs in a PET scanner. The normalization correction factors are assumed to be proportional to the inverse of the counts in each LOR. To avoid dead time, and pile-up effects, a relatively low activity source is employed. However, the method needs to collect adequate counts per LOR to reduce the statistical noise, resulting in scan time typically lasting several hours.

An alternative method is to model the total normalization factor as the product of several individual components, including individual detector efficiencies ε and geometrical factors g. The normalization correction factors $n_{i,j}$ for detector pair (i, j) can be written as [29]:

$$n_{i,j} = \frac{1}{\varepsilon_i \times \varepsilon_j \times g_{i,j}} \ldots\ldots\ldots\ldots (2.9)$$

The individual detector efficiency is used to account for the intrinsic detector efficiency due to effects such as crystal non-uniformity and variations in PMT gain. The individual detector efficiency can be measured by using a uniform cylindrical source. The geometrical factors in 2.9 include both the transaxial and axial components, which account for different LOR efficiencies, photon incidence angles, and detector positions within the block as well as for different ring combinations. The geometrical factors can be determined by employing a rotating rod source.

2.4.2 Random correction

Due to the finite width of the electronic time window, two uncorrelated single events occurring sufficiently close together in time can be mistakenly identified as a true coincidence. This is known as random coincidences or accidental coincidences. Mathematically the random rate $C_{i,j}$ will be given by

$$C_{i,j} = 2\tau r_i r_j \ldots\ldots\ldots\ldots\ldots\ldots (2.10)$$

where r_i and r_j are the rate of single events on channel i and j. If the small difference between channels is ignored, the randoms are roughly proportional to the square of the activity distribution.

The random coincidences contain no spatial information about the source position and distribute quite uniformly within the FOV, which can degrade image contrast and introduce significant image artifacts without any effective correction. There are three random correction approaches.

The Tail fitting method assumes that the distribution of random coincidences slowly changes in the projection space. Thus, the distribution of random coincidences within the object can be estimated by fitting a function to the tails falling outside the object. This method can be used to correct for both scatter and randoms simultaneously [35].

The second method to estimate the randoms rate can be obtained from single counting rates for a given detector pair and the coincidence time window as indicated by Equation (2.10). Then the estimated random rate can be subtracted from the measured counts for each LOR.

Lastly, the currently most commonly implemented method for estimating random coincidences is the delayed coincidence channel method. A duplicate data stream containing the timing signals from one channel is delayed by several times the duration of the coincidence window before being sent to the coincidence processing circuitry. The delay has removed the correlation between pairs of events arising from actual annihilations so that the detected coincidences are all randoms. The resulting coincidences are then subtracted from the coincidences in the prompt channel to yield the random corrected coincidences rate. However, this method can increase the overall system dead time and amplify the noise in the subtracted data.

2.4.3 Attenuation correction

When the annihilation photons travel through the object, they will interact with surrounding materials and photons will be absorbed or scattered out of the FOV. In such a case, this coincidence will be lost. This photon attenuation phenomenon can cause severe distortions in PET images. Quantitatively accurate and artefact-free PET images require compensation for attenuation.

The probability of detecting a true coincidence depends on the combined path of both photons arising from the same annihilation, which is independent of source position on this combined path as illustrated in Figure 2.10 and Equation (2.7). The attenuation for a given LOR can be corrected by either direct measurement or using a mathematical model.

The first method to determine the attenuation correction is through direct measurements. The attenuation correction factors for each LOR are given by the ratio of the count rate from a transmission scan, obtained by placing a positron-emitting source outside the object, with that of an unattenuated count rate. This is obtained from a blank scan, which uses the same source, but with no patient in the scanner. Either a set of ring sources or a rotating rod source can be used in this measuring process. This method can directly measure the attenuation without any assumptions about the shape of the object or the distribution of attenuation coefficients. Therefore, it is the most accurate method. However, if an adequate number of counts for each LOR is not obtained, the transmission scan will suffer statistical errors.

The calculated attenuation correction method is an alternative approach based on Equation (2.7). This method assumes a regular geometric body outline and constant tissue density within this object. The attenuation factors are calculated for each LOR, based on the constant attenuation coefficient along a chord through the object. This method can produce images that are free of attenuation artifacts, but is prone to underestimating the attenuation [36].

With the advent of dual modality scanners like PET/CT or PET/MR, efforts have been made to use CT or MRI data for PET attenuation correction. The advantages of these approaches are the statistical quality and spatial resolution of CT or MRI images. However, CT scanning may cause substantial artifacts in the reconstructed images because CT provides a snapshot of respiratory motion while PET is a time-averaged image. Since the FOV of CT is typically smaller than that of PET, the truncated CT images may cause additional problems when calculating the attenuation map for PET. Due to the different energies used in PET and CT, the attenuation map measured at CT energies must be rescaled to the appropriate emission energy for PET attenuation correction [37]. For MR there is no a simple scaling relationship between MR images and a PET attenuation map because MR images are dependent on the characteristics of protons while PET attenuation is affected by electron density [38]. This problem may be solved by segmenting MR images into different tissue types and attributing the average tissue-dependent attenuation coefficients for PET attenuation correction.

2.4.4 Scatter correction

When a positron annihilates in the body, it is possible that one or both of the annihilation photons will undergo a Compton scattering in the body or the detector. Compton scattering degrades the image contrast and compromises quantitative accuracy in PET [22, 39]. The scatter fraction refers to the proportion of accepted coincidences which have undergone Compton scattering. The scatter fraction depends on several factors, including the geometry of PET scanners, the energy window and the size and density of scanned object. The scatter fraction typically ranges from 15-20% in a ring tomograph with slice-defining septa, to as high as 40-60% [4-6] when the scanner operates in 3D mode or with large patients.

The goal of this thesis is to investigate whether better use can be made of the scatter coincidences to improve the functional imaging content as well as to extract anatomical information. In order to put the scatter based approach into context, this section will introduce the conventional scatter correction based reconstruction methods. The approaches for estimating and correcting scattered coincidences in PET can be generally divided into four main categories: empirical scatter corrections [40], multiple energy window techniques [10, 11, 15], convolution and deconvolution approaches [18], and simulation-based scatter correction methods.

Empirical scatter correction methods make use of the unique differences between scattered events and true coincidences. These methods include a fitting scatter tail approach and a direct measurement technique. Fitting the scatter tail is the simplest approach to estimating the scattered distribution. This method takes advantage of the observation that coincidences recorded outside the object are entirely due to scattered events, and its distribution varies slowly across the FOV. Thus, the scattered distribution can be estimated by fitting the scatter tail outside the object in the projection space using a smoothly varying function. For example, a second order polynomial and 1D Gaussian curve have been used to fit the scatter tails. Then the scatter corrected data can be obtained by deconvolving or subtracting the fitted function from the measured data. This method can be used to correct for both scatter and randoms simultaneously in some systems. It is simple to implement and computationally very efficient. This method has been used for scatter correction in the neurological PET imaging, in which the scatter recorded outside the object can be reduced to approximately zero. Besides, it inherently corrects for scatter arising from activity outside the axial field of view, while some of the more complex approaches are unable to do. The drawback of this method is that the scatter distribution is not always well approximated by a smooth analytical function, leading to over- or under-subtraction of scatter. Another approach in this category is the direct measurement technique, which takes advantage of the difference between scatter distributions with the septa extended or retracted. Thus this method is only applicable to PET scanners with retractable septa. The first step for this method is to make a measurement of the same object with septa extended and with septa retracted. Then the septa extended projections need to be scaled to account for differences in detection efficiency due to septa shadowing. The scatter contribution for the direct plane can be generated by subtracting the septa extended and retracted projection data. The advantages of this method are that few assumptions are made, and it is relatively simple to implement. It enables to measure the scatter distribution in complex objects, which can help better understanding of scattering in 3D PET or validating other scatter correction methods. However, this method requires an additional measurement, which may be impractical and only applicable to PET scanners with retractable septa. Another problem is that the method ignores the scatter that is already present in the direct planes measured with the septa extended.

Multiple energy window techniques are based on the observation that a greater proportion of Compton scattered events are recorded below the photopeak in the single photon energy spectrum, and above a critical energy only unscattered photons are recorded (see

Figure 2.18). Thus, data recorded in energy windows set below or above the photopeak window, or both, can be used to derive an estimate of the scatter contribution. This method has been widely employed and investigated in SPECT. The dual energy window method uses an upper window that contains scattered and unscattered photons, and a lower window that contains only scattered photons. Then some fraction of the counts recorded in the low-energy window is subtracted from the high-energy window counts. By making use of measurements in auxiliary energy window, two distinct approaches have been developed to the use of dual energy windows for scatter correction. The dual energy window method uses an energy window set below the photopeak and abutting it. The other approach known as the estimation of trues method uses an energy window with the lower level discriminator set above 511 keV and overlaps the upper portion of the photopeak window. The main advantage of the dual energy window methods is that they take into account scatter arising from activity beyond the axial FOV. The drawback of this method is that both the energy windows contain a mixture of both unscattered and scattered events, and the low energy window may contain multiple scattered events. The accuracy of the dual energy window depends on the object sizes. The triple energy window method is a straightforward extension of the dual energy window, which introduces a modification factor to account for source size and distribution dependencies of scattered events. The multiple energy window method is not straightforward to implement and requires specialized hardware and extensive measurement to characterize the scatter component.

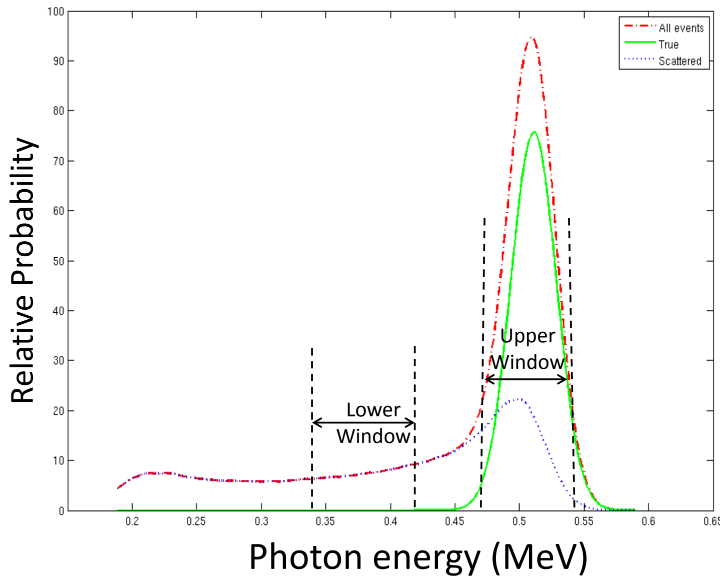

Figure 2. 18 The energy spectra for the total, true and scattered coincidences. The upper and lower energy windows for the dual energy window scatter correction are also illustrated in this figure.

Different from the energy window methods that derive scatter distribution from auxiliary measurements, the convolution and deconvolution approaches model the scatter distribution with an integral transformation of the true activity distribution with a scatter response function. Since the true activity distribution cannot be measured, it is usually substituted by the measured projection data in the photo-peak window to achieve a reasonable degree of accuracy. The scatter response function is assumed to be position-dependent and is measured by using a line source positioned at regular intervals across the scanner's FOV. The scatter corrected data can be obtained by subtracting the scatter estimate from the measured projections. This approach has performed reliably in neurological studies where the scattering medium is relatively homogeneous, and can achieve comparable results to energy window based methods. Since the scatter estimate in this approach is essentially noise-free, it does not contribute additional noise to the scatter-corrected projections. However, the assumptions break down in both the SPECT and PET cases when more complex objects are involved.

Simulation-based scatter correction is the most accurate scatter correction method so far, which is developed based on the well-understood physics principles that govern photon interactions in matter. The first step of this method is to reconstruct the initial estimate of the source distribution with an attenuation map, then the scatter can be simulated, either using a simple single scatter model [24, 33], or using a Monte Carlo simulation [19, 22]. In an analytical simulation, it is assumed that only one of the annihilation photons in a coincidence accepted within the photopeak undergoes a Compton interaction. Then the single scatter coincidence rate at each LOR can be calculated. It has been shown that this method can yield estimates of the scatter distribution that are reasonably accurate under most circumstances. However, the computational demand is very large if the volume is integrated over every possible scattering point and the scatter contribution calculated for every LOR. This problem can be practically solved by sampling the object volume on a regular grid of sparsely spaced scattering points and calculating the scatter for only a subset of all LORs. Then the full scatter distribution can be interpolated from the calculated LORs with little bias. The advantage of this model-based method is that it makes use of the well understood physical principles to produce accurate scatter estimates. The main drawbacks are the complexity of implementation and the high computational demand. The second method in this category is the Monte Carlo simulation method, which can not only accurately estimate the scatter distribution but also allow separation of the simulated scattered and unscattered contributions to the projections. Furthermore, this method can be used for any specified emission and attenuation distribution as well as several different PET scanner geometries. Similar to the analytical simulation, Monte Carlo techniques are based on well understood physical principles that govern photon interactions in matter. In this technique, photon pairs are generated at their point of origin, which is defined by the initial estimate of the activity distribution. Then these photons will travel with random orientation and be “tracked’ as they traverse through the scattering medium, which may be defined by the attenuation map. Tracked photons have a random chance of interaction in each voxel they traverse. The type and the probability of interaction are determined by the different photon interaction cross-sections. To get accurate enough simulation results, sufficient counting statistics should be guaranteed in the Monte Carlo simulations. This method is potentially a very accurate and practical approach to scatter correction in PET.

2.4.5 Dead time correction

In a PET scanner, a minimum amount of time is required to process successive coincidences in order that they can be registered as separate events. This includes the time spent for integrating charge from the photomultiplier tubes arising from a scintillation flash in the detector crystal, the reset time for the detector electronics as well as the time for processing a coincidence event. This effect reduces the number of coincidences counted by the PET scanner, and the linear response of the system is compromised at high-count rates. This phenomenon is characterized by the dead time. The fractional dead time of a system at a given count-rate is defined as the ratio of the measured count-rate and the count-rate that would have been obtained for an ideal system. The most common way to characterize dead time is to separate it into the paralyzable and non-paralyzable components. The paralyzable component models the situation for a system that accepts new events during a fixed amount of time τ after each event, the dead time will extend for every new incoming event and will eventually be paralyzed.. The relationship between the measured event rate *m* and the actual event rate *n* is given by

$$m = ne^{-n\tau} \text{……………………..(2.11)}$$

where τ is the dead time constant.

In contrast to the paralyzing case, the non-paralyzing models situation that the system is rendered dead after each event for a time τ, during which no other event can be accepted. After the fixed dead time, the system will be able to process the next incoming event.. The relationship between the measured count *m* and the actual event rate *n* in the non-paralyzing models is given by

$$m = \frac{n}{1+n\tau} \text{………………………(2.12)}$$

The measured true counts as a function of the actual true counts in the paralyzing and non-paralyzing models can be seen in Figure 2.19 [29].

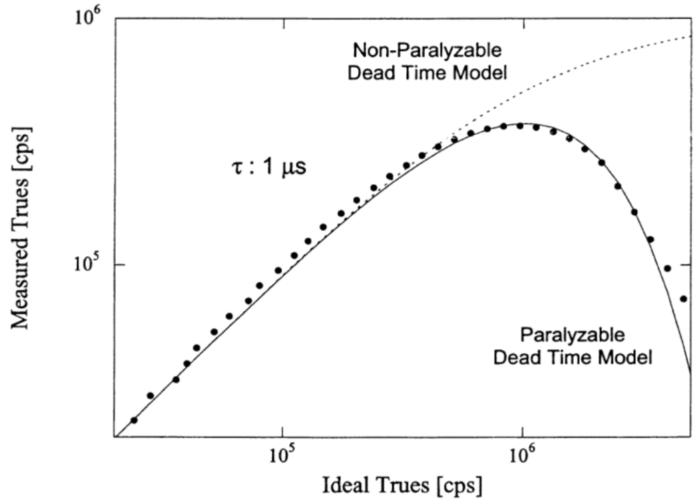

Figure 2.19 The measured counting rate as a function of ideal true event rate. The solid line shows the fit of the data to a paralyzable dead time model. The dashed line shows the corresponding fit for a nonparalyzable dead time model [29].

2.4.6 Partial volume correction

Ideally, a PET image should depict the distribution of the radiotracer uniformly and accurately throughout the FOV. However, due to the limited spatial resolution of PET systems, decays from an infinitely small point source will be smeared out and will appear in the reconstructed image as a finite-sized blob of lower activity concentration. This effect, known as the partial volume effect, reduces the image contrast between high and low uptake regions. The correction for this effect is of particular importance in the quantitative characterization of small lesions or structures. There are several possible approaches to correcting or at least minimizing the partial volume effect. These methods include resolution recovery or using anatomical imaging data. The resolution recovery method attempts to improve the resolution of the reconstructed images by using an inverse filtering in an analytical reconstruction method or by extending the imaging model to include the resolution effects in an iterative reconstruction regime. The anatomical imaging method convolves high-resolution anatomical data with the scanner's point spread function (PSF). The PET images can be divided into a discrete number of tissue domains, each of which contains a uniform radiotracer concentration. The mean value within each tissue domain is modeled as the weighted sum of the true activity values in the surrounding voxels belonging to the same domain. The weights can be determined based on the PSF. Region-based partial volume correction approaches are mainly based on a key study by Rousset et al. [41] in what is commonly referred to as the geometric transfer matrix (GTM) method. In this method, partial volume effect is modeled with the geometric interactions induced by the PET scanner between the regions in which a PVE-corrected mean value is searched. The initial work proposed estimation of the geometric interaction factors through a projection, followed by a tomographic reconstruction of the anatomic regions under study. An alternative approach to that of modeling the PET scanner PSF is to incorporate information from anatomical imaging into the reconstruction model [41, 42].

2.5 Image Reconstruction

A PET image is a quantitative representation of the cross-sectional distribution of the radioactive tracer. The integrated radioactivity along the line joining the two detectors, which is referred to as line integral data, is proportional to the total number of counts measured by a particular detector pair. Image reconstruction converts the line integrals data measured at many different angles around the object into an image that quantitatively reflects the distribution of positron-emitting atoms, and therefore, the molecule to which it is attached. In a 2D reconstruction, the image is a slice through the object parallel to the detector plane. Much attention has been paid to the reconstruction of images from projections, and many analytical and iterative reconstruction schemes exist. Analytic reconstruction methods relate the line integral measurements to the activity distribution in the object by utilizing the mathematics of computed tomography. The iterative methods model the data collection process and attempt, in a series of successive iterations, to find the image that is most consistent with the measured data.

2.5.1 Analytical image reconstruction

The Radon transform is the mathematical operator mapping a function onto its line integrals. If a function *f(x,y)* represents an unknown density, then the Radon transform represents the projection data obtained as the output of a tomographic scan.

$$Rf = \int_{R^2} f(x,y)\delta(x\cos\theta + y\sin\theta - t)dxdy \text{.............}(2.13)$$

Hence the inverse of the Radon transform R*, known as backprojection, can be used to reconstruct the original density from the projection data, and thus it forms the mathematical underpinning for tomographic reconstruction, also known as image reconstruction.

Tomographic reconstruction can be developed using Fourier analysis. The Fourier transform of a function *f(x,y)* is given by

$$(Ff)(v_x, v_y) = F(v_x, v_y) = \int_{R^2} dx\, dy\, f(x,y)e^{-2\pi i(xv_x + yv_y)} \text{......}(2.14)$$

and the inverse Fourier transform *F(x,y)* is obtained by changing the sign of the complex exponential:

$$(F^{-1}F)(x,y) = f(x,y) = \int_{R^2} dv_x\, dv_y\, F(v_x, v_y) e^{2\pi i(xv_x + yv_y)} \text{.........(2.15)}$$

where v_x and v_y are the frequencies associated with x and y respectively.

A key property of the Fourier transform is the convolution theorem, which states that the Fourier transform of the convolution of two functions f and h,

$$(f * h)(x,y) = \int_{R^2} dx'\, dy'\, f(x', y') h(x - x', y - y') \text{...............(2.16)}$$

is equal to the product of their Fourier transforms:

$$\big(F(f * h)\big)(v_x, v_y) = (Ff)(v_x, v_y) \cdot (Fh)(v_x, v_y) \text{....................(2.17)}$$

In signal- or image-processing terms, convolving f with h amounts to filtering f with a shift-invariant PSF h. The convolution theorem simplifies convolution by reducing it to a product in frequency space.

The Central Section Theorem, also called the Projection Slice Theorem, states that the 1D Fourier transform of a projection with respect to the radial variable s is related to the 2D Fourier transform of the image f by

$$P(v,\theta) = F(v_x = v\cos\theta, v_y = v\sin\theta) \text{.........(2.18)}$$

where

$$P(v,\theta) = (Fp)(v,\theta) = \int_R ds\, p(v,\theta) e^{-2\pi i s v} \text{............(2.19)}$$

and v is the frequency associated with the radial variable s. This theorem is illustrated in Figure 2.20.

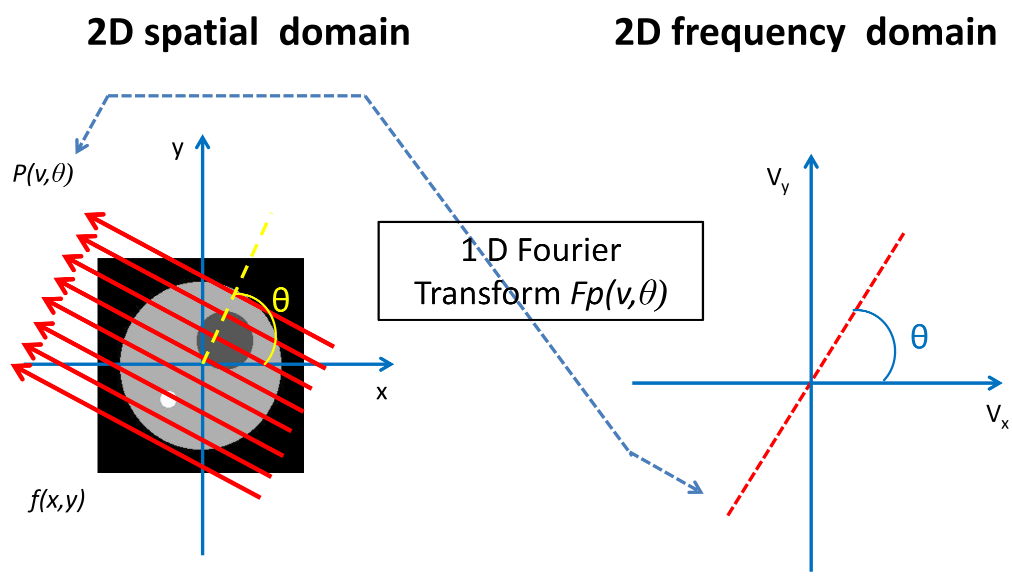

Figure 2.20 The illustration of the Central Section theorem. It states the 1D FT of a projection taken at angle θ equals to the central radial slice at angle θ of the 2D FT of the original object.

The discrete implementation of the inversion formula combining Equations (2.19), (2.18) and (2.14) is referred to as the direct Fourier reconstruction. This algorithm need firstly take the 1D Fourier transform of the first row in a sinogram, then interpolate and add onto a 2D rectangular grid $F(v_x,v_y)$.The same process needs to repeat for all subsequent rows in the sinogram. Lastly an image $f(x,y)$ can be found by taking the inverse 2D Fourier transform. This algorithm is numerically efficient but the interpolation required to map the polar grid onto the square grid before taking the inverse Fourier transform is computationally intensive and sensitive to interpolation errors.

By reformulating the Central Section Theorem in the spatial rather than frequency domain, a more elegant approach known as the Filtered Backprojection (FBP) algorithm can be achieved, which has become the standard algorithm for tomography. It is given by

$$f(x,y) = (X^{*}p^{F})(x,y) = \int_{0}^{\pi} d\theta p^{F}\,(s = x\cos\theta + y\sin\theta\,, \theta)\ldots\ldots\ldots(2.20)$$

where the backprojection operator X^* maps p^F onto f and is the dual of the Radon transform. Geometrically, $(X^*p^F)\,(x, y)$ is the sum of the filtered data p^F for all lines that contain the point (x, y) [1].

The filtered projections p^F are

$$p^{F}(s,\varphi) = \int_{-R_F}^{R_F} ds'\, p(s',\varphi)h(s-s')\ldots\ldots\ldots..(2.21)$$

and the ramp filter kernel $h(s)$ is defined as

$$h(s) = \int_{-\infty}^{\infty} dv|v|e^{2\pi isv}\ldots\ldots\ldots\ldots\ldots\ldots..(2.22)$$

A drawback of ramp filter is that it amplifies the noise associated with high frequencies. To eliminate high-frequency noise, various filters have been designed. All of them are characterized by a maximum frequency, called the Nyquist frequency, which gives an upper limit to the number of frequencies necessary to describe the sine or cosine curves representing an image projection.

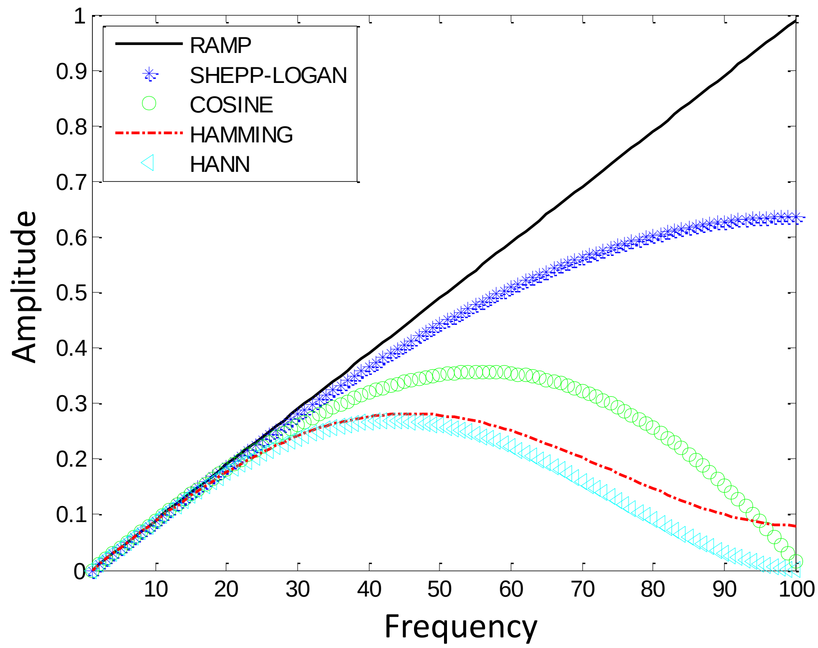

Figure 2.21 Three reconstruction filters that are commonly used in filtered backprojection.

Compared with the direct Backprojection in Equation (2.15), the only difference is that the projections have been modified by a filter, which is where the name "Filtered Backprojection" comes from. FBP is a fast method for PET image reconstruction because it is linear. On the other hand, it is sensitive to the measured data and an arbitrarily small perturbation of projection due to measurement noise can cause a large error in the reconstructed image.

2.5.2 Iterative image reconstruction

Iterative reconstruction is an alternative approach, which is playing an increasingly important role in clinical PET image reconstruction. One of the strengths of iterative algorithms is that they are largely independent of the acquisition geometry. In iterative methods of image reconstruction, an initial estimate of an image is made, and the projections are computed from the image and compared with the measured projection. If there is a difference between the estimated and measured projections, properly formulated adjustments are made to improve the current estimated image, and a new iteration is performed to assess the convergence between the estimated and measured projections. Iterations are continued until the convergence criteria are met. This process is illustrated in Figure 2.22.

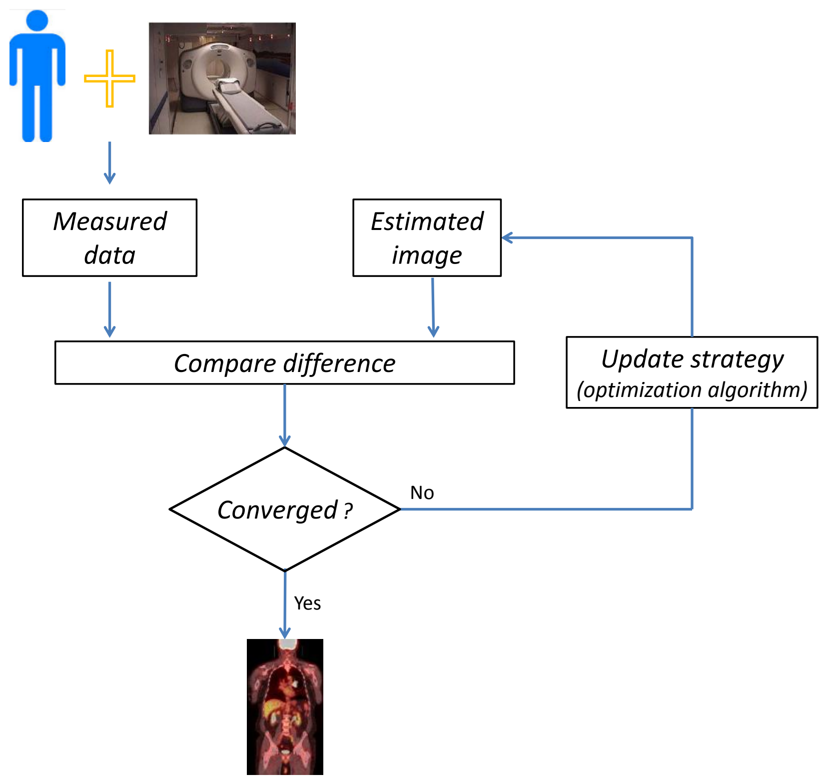

Figure 2.22 a Basic flowchart for iterative image reconstruction process.

An iterative reconstruction algorithm generally includes four ingredients: data model, image model, the system matrix, and the cost function. Instead of using a simple line integral of activity along LOR in an analytical algorithm, any linear physical effects, like attenuation and scatter, gaps in the detectors, non-uniform resolution of the detectors, etc., can be modeled in the sensitivity function for each LOR in the data model. The statistical distribution of the measured raw data around its mean for each LOR is typically modeled using a Poisson distribution. The image model in an iterative algorithm is represented as a linear combination of basis functions. In most algorithms, contiguous and non-overlapping pixels basis functions are used. Combining the data model and the image model, a set of linear equations can be generated which is known as the system matrix. The system matrix characterizes the probabilities that the annihilation photons emitted in pixel *i* are detected in j^{th} LOR. The cost function, also known as optimization algorithm, is a function that gives a measure of the difference (or similarity) between the estimated and measured projections and is the function which will be minimized (or maximized) in an iterative way. The differences between different types of iterative algorithms are how the cost function is defined and how to search or update the cost function to its minimum or maximum as quickly as possible.

The various possible choices for these four ingredients generate many different types of iterative algorithms that differ in some aspect of their formulation and implementation. The most widely used iterative reconstruction algorithm in PET is the maximum-likelihood expectation maximization (ML-EM) algorithm [43, 44] and its accelerated version OSEM (Ordered Subset EM). The cost function in the ML-EM and OSEM algorithms is the Poisson likelihood. The ML-EM algorithm updates the image during each iteration using:

$$\vec{f}_i^{\,n+1} = f_i^n \frac{1}{\sum_{j'=1}^{N_{LOR}} a_{j',i}} \sum_{j=1}^{N_{LOR}} a_{j,i} \frac{p_j}{\sum_{i'=1}^{P} a_{j,i'} f_{i'}^n} \quad i = 1, \ldots, p \ldots\ldots(2.23)$$

Usually, the algorithm starts with an initial estimate of the image f as a uniform distribution. The sum over *i'* in the denominator of the second factor in the right-hand side is a forward projection: therefore, the denominator is the average value $< p_j^n >$ that would be measured if f^n were the true image. The sum over j in the numerator is a multiplication with the transposed system matrix and represents the backprojection of the ratio between the measured and estimated data. Finally, the denominator in the first factor is equal to the sensitivity of the scanner for pixel i. This method requires many iterations to achieve an acceptable agreement between the estimated and the measured image demanding a lengthy computation time. To circumvent this problem, the OSEM algorithm has been introduced, which is a modification of ML-EM, in that projections are grouped into subsets around the object separated by some fixed angle and only one subset is updated in each iteration.

Generally, iterative methods can produce images with better SNR and reduced streak artifacts. One disadvantage of iterative reconstruction is the long computational time involved but this problem can be solved by the increased computer speed and acceleration techniques. Another comment is the nonlinear relationship modeled in the iterative reconstruction, which makes the behaviour of the algorithms and reconstructed image difficult to predict.

2.5.3 3D reconstruction

Reconstruction of images from 3D data is, particularly in a multi-ring scanner, complicated by a large volume of data. Processing and storage of such a large amount of data is challenging for routine clinical applications. FBP can be applied to 3D image reconstruction with some manipulations. The 3D data sinograms are considered as a set of 2D parallel projections, and FBP is applied to these projections by the Fourier method

[45-49]. The iteration methods also can be generally applied to the 3D data. However, the complexity, large volume, and incomplete sampling of the data due to the finite axial length of the scanner are some of the factors that limit the use of the FBP and iterative methods directly in 3D reconstruction.

To circumvent these difficulties, a modified method of handling 3D data is commonly used. This involves the rebinning of the 3D acquisition data into a set of 2D equivalent projections. Rebinning is achieved by assigning axially tilted LORs to transaxial planes intersecting them at their axial midpoints. This is equivalent to collecting data in a multi-ring scanner in 2D mode, and is called the single slice-rebinning algorithm (SSRB) [45, 48]. This method works well along the central axis of the scanner, but steadily becomes worse with increasing radial distance. In another method called the Fourier rebinning (FORE) algorithm [49], rebinning is performed by applying the 2D Fourier method to each oblique sinogram in the frequency domain. This method is more accurate than the SSRB method because of the more accurate estimate of the source axial location. After rebinning of 3D data into 2D data sets, the FBP or iterative method is applied.

Chapter 3: Evaluation of the Feasibility and Quantitative Accuracy of a Generalized Scatter 2D PET Reconstruction Method

The material in this chapter has been reprinted and adapted from ISRN Biomedical Imaging, Volume 2013, Hongyan Sun, Stephen Pistorius, "Evaluation of the Feasibility and Quantitative Accuracy of a Generalized Scatter 2D PET Reconstruction Method," Copyright (2013), with permission from Hindawi Publishing Corporation.

3.1 Introduction

Compton scattering degrades image contrast and compromises quantitative accuracy in PET [22, 39]. Scattered coincidences are typically considered as noise, which reduces PET image quality. This issue is more serious when operating in 3D mode without slice-defining septa and in large patients, where the scatter fraction can be as high as 40-60% [1, 4-6]. Consequently, a number of approaches for estimating and correcting scattered coincidences in PET data have been proposed [4, 7-16, 19, 21, 50], which have been reviewed in Section 2.4.4 in this thesis. Most of these techniques estimate a scatter sinogram, which is used to subtract the scatter from the projection data [18] in pre-correction methods [51] or as a constant additive term incorporated in a iterative reconstruction algorithm [52-54]. Inaccuracy in the estimation of the scatter sinogram will introduce significant biases in the activity distribution [6]. The subtraction based correction methods will destroy the Poisson nature of the data, reduce the system's sensitivity and amplify image noise [4, 55].

With list-mode acquisitions available in modern PET scanners and the improved detector technology, the use of the energy of individual photons becomes feasible and some authors have proposed new approaches that includes the energy information of the measured photons in the estimation of the scatter distribution and image reconstruction process [6, 56-58]. These approaches attempt to improve the accuracy of the rejection of scattered coincidences from the measured data but are limited by the energy resolution of the detectors [59].

Since the energy of detected photons also carries some probabilistic information about the spatial distribution of the annihilation positions and by taking advantage of Compton scattering, scattered coincidences are also a potential source of latent information for PET image reconstruction. Incorporating scattered coincidences directly into reconstruction eliminates the need for scatter correction, and also could improve both image quality and system sensitivity, since a lower energy threshold can be selected. In this work, a reconstruction method has been proposed, which is similar to that of Conti et al. [60] that directly includes scattered photons in the PET image reconstruction algorithm instead of correcting for them as do conventional emission imaging methods.

An important difference between this work and that of Conti et al. [60] is that the method proposed by Conti et al. makes use of both TOF information and the energy of individual photons to reconstruct scattered, and unscattered PET coincidences [61]. This chapter focuses on a non-TOF PET algorithm, which does not make use of the time difference between the two detected annihilation photons. Another difference is that this work uses the Compton kinematics to predict the locus of all possible scattering positions to confine the annihilation position instead of using a pixel-driven approach, which can reduce the computational workload. This work has been presented, in part, at the World Congress on Medical Physics and Biomedical Engineering in 2012 [62].

This chapter will evaluate the feasibility, the effects of the scatter fraction and the choice of a new coincidence selection threshold, which uses both the scatter photon energy and detector position for each coincidence, on the image quality obtained using a novel PET scattering reconstruction algorithm.

3.2 Methods and Materials

3.2.1 Reconstruction Theory

In clinical PET scans, more than 99.7% of the interacted events in water are Compton scattering events [63]. Coherent scattering is neglected because of its small contribution to the total cross section for the energies of interest in nuclear medicine [55]. In approximately 80% of detected scattered coincidences, only one of the two annihilation photons undergoes a single Compton interaction [1, 8, 64]. This assumption has been validated by both MC simulations and experiment measurements in the single-scatter simulation (SSS) technique [24, 25].

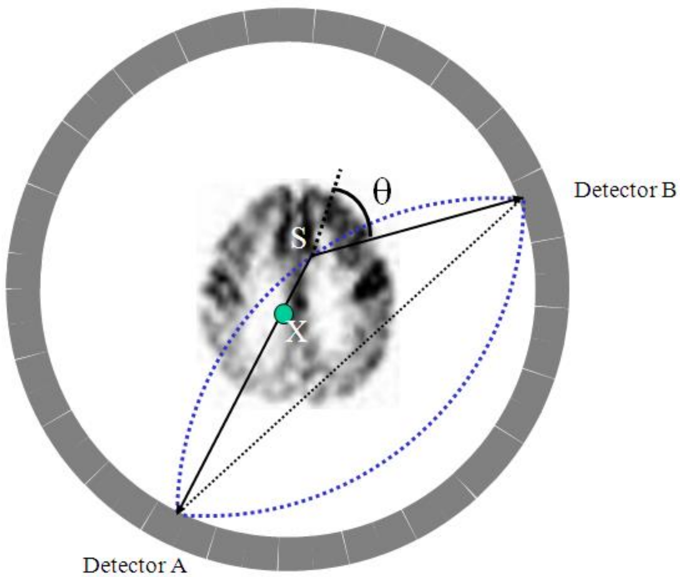

Figure 3.1 A diagram of a Compton scattering event in a patient. The two anti-parallel photons are generated at the annihilation position X shown by the green dot. The unscattered photon is observed by detector A while the other photon suffers a Compton scattering event at S, deviates from its initial path by an angle θ and is detected by detector B. This figure also illustrates the two circular arcs (TCA), shown as blue dotted curves, which describe the locus of possible scattering locations and also enclose the annihilation position.

Figure 3.1 illustrates a scattered coincidence in a patient. The two annihilation photons are generated at source X, the unscattered photon is detected at A while the other photon undergoes a Compton scattering interaction at S and is detected at B with energy E'. The scattering angle θ can be related to the scattered photon energy E' by the Compton equation:

$$\cos\theta = 1 + \frac{m_e c^2}{E} - \frac{m_e c^2}{E'} \qquad (3.1)$$

where the scattering angle θ is defined as the angle between the directions of the incident and the scattered photon, $m_e c^2$ is the electron rest mass energy equal to 511 keV; E is the incident photon energy and E' is the scattered photon energy in keV. The energy of the scattered photon decreases as the scattering angle increases with the energy of the scattered photon ranging from ~170 to 511 keV, corresponding to backscatter and forward scatter respectively. By taking advantages of the kinematics of Compton scattering, a 2D surface described by two circular arcs (TCA) connecting the coincidence detectors (rather than the conventional straight-line assumption which is true only for true coincidences), which scribes the possible scattering locus and encompasses the annihilation position, can be identified as illustrated in Figure 3.1. The accuracy of the locus defined above ignores the positron range and is closely related to the energy resolution of the detectors.

The size and shape of the TCA is a function of the scattering angle, and the two coincident photon detected positions. As shown in Figure 3.2, in the limit where the scattering angle approaches zero and the energy of the scattered photon approaches 511 keV, the shape of TCA approaches the LOR for true coincidences. Thus, the true coincidences can be considered as a subset of the scattered coincidences with zero scattering angles. We therefore, propose a Generalized Scatter (GS) approach that generalizes the concept of the conventional meaning of scatter and can include both true and scattered events into the PET imaging reconstruction in a consistent way.

The work in this thesis is carried out in two dimensions, although the same approach can, in general, be implemented in three dimensions where it will ultimately be of greater value.

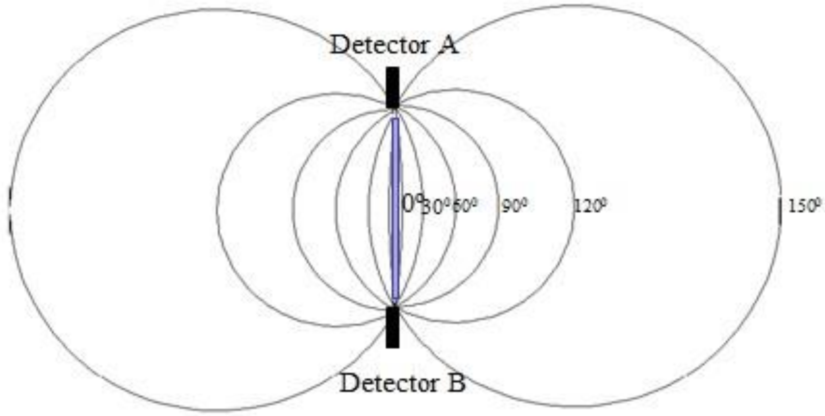

Figure 3.2 The TCA shapes versus the scattering angles for the same two detectors. Each TCA consists of two symmetrically circular arcs. The inner to the outer arcs correspond to scattering angles of 0, 30, 60, 90, 120, 150 degrees respectively. When the scattering angle is smaller than 90 degrees, the TCA is made up of two minor arcs; when the scattering angle is 90 degrees the TCA is a circle; when the scattering angle is larger than 90 degrees the TCA is made up of two major arcs. As the area encompassed by the TCA increases with scattering angle, the ability to accurately determine the annihilation position decreases.

3.2.2 The generalized scatter algorithm

$<P_{AB}(\theta)>$ represents the mean number of coincidences, where the unscattered photon is observed at A while the other annihilation photon undergoes a Compton scattering through an angle θ and is observed at B (see Figure 3.1). It can be calculated using the following equation:

$$\langle P_{AB}(\theta)\rangle = \tau \oint_A^B \left[\int_A^S f_x\, dx\right] \cdot \rho_e(S) \cdot \frac{d\sigma_C^{KN}}{d\theta} \frac{1}{4\pi} e^{-\left(\int_A^S \mu dl + \int_S^B \mu' dl\right)} ds \ldots\ldots\ldots\ldots\ldots\ldots (3.2)$$

The inner integral in the above expression calculates the total photon flux that can reach one of the possible scattering points (say S) due to the source f_x lying on the line segment

AS. Once these photons arrive at one of the possible scattering positions S, the possibility of photons suffering a Compton interaction with a scattering angle θ is linearly proportional to the differential Klein-Nishina electronic cross section $\frac{d\sigma_C^{KN}}{d\theta}$ and the electron density ρ_e at this point. The outer integral sums the scattered coincidences over all the possible scattering positions along the TCA. Tau (τ) is the acquisition time, μ and μ' are the linear attenuation coefficients for the unscattered and scattered photons.

Considering the sparse number of coincidences contributing to each $<P_{AB}(\theta)>$, the maximum-likelihood expectation maximization (ML-EM) [43, 44, 65] in a list-mode form was derived, in which each coincidence will be stored and calculated successively. Thus:

$$\vec{f_i}^{n+1} = f_i^n \frac{1}{\sum_{j'=1}^{N} a_{j',i}} \sum_{j=1}^{N} a_{j,i} \frac{1}{\sum_{i'=1}^{p} a_{j,i'} f_{i'}^n} \quad i = 1, \ldots, p \ldots\ldots\ldots\ldots\ldots(3.3)$$

where p is the total number of pixels in the image, N is the total number of detected coincidences and $a_{j,i}$ is the element of system matrix representing the probability, weighted by the Compton differential cross section that the annihilation photons detected in the j^{th} coincidence (whether scattered or not) were emitted from Pixel i. In practice $a_{i,j}$ is proportional to the Compton cross section if the i^{th} pixel falls within the j^{th} TCA and is zero if Pixel i is outside the TCA. The main difference between this GS method based ML-EM algorithm (GS-MLEM) and the conventional ML-EM algorithm (LOR-MLEM) is that the summation for each coincidence is over the area confined by the TCA, instead of along the LOR. This algorithm also can account for random coincidences R by adding them to the projector as follows: $\sum_{i'=1}^{p} a_{j,i'} f_{i'}^n + R_j$. The GS-MLEM was implemented as shown in Figure 3.3. The ratio of the measured number of coincident events (which is

1 with a list-mode algorithm) to the sum of the pixel values within each TCA for the current estimate is back projected into a "ratio" matrix. This backprojection is repeated for all coincident events. The "ratio" matrix is used to modify the current estimate. This process is repeated in an iterative fashion, updating the current image until a good convergence is obtained.

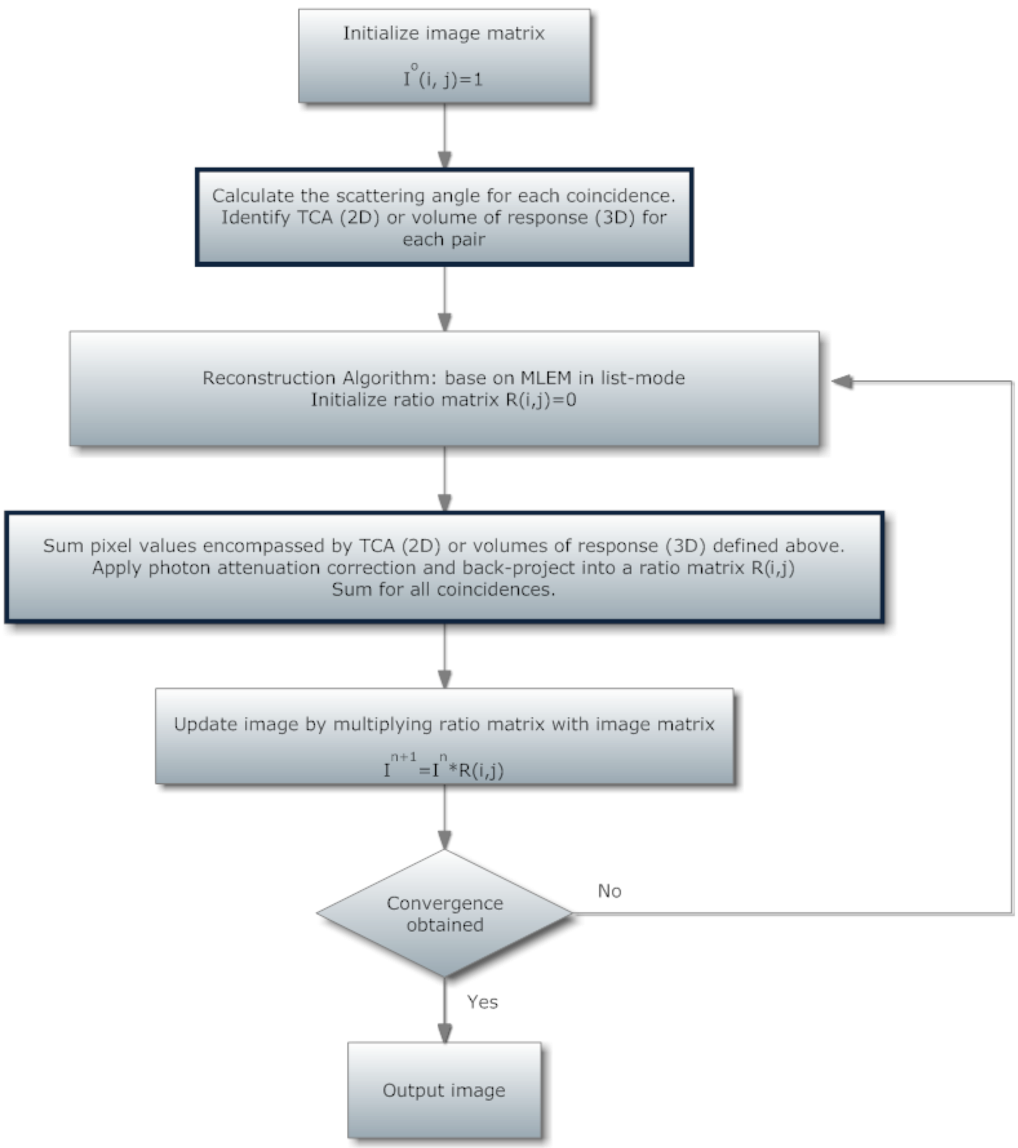

Figure 3.3 The GS-MLEM algorithm flow chart. The additions and changes to the conventional MLEM (LOR-MLEM) algorithm are highlighted by the boxes with a black thick outline.

3.2.3 The GATE platform and Phantom measurements

The proposed algorithm was evaluated on a 2D small animal PET system simulated by the Geant4 Application for Emission Tomography (GATE) [66-68]. GATE is an object-oriented Monte Carlo simulation platform based on Geant4 libraries [68]. The simulated PET scanner had a 24 cm diameter detector ring made up of 42 detector blocks. Each detector block is arranged in a 9×5 lutetium oxy-orthosilicate (LSO) crystal array. Each crystal element had a surface area of 2×2 mm^2 and was 18 mm thick. The energy resolution of the simulated scanner in this preliminary investigation was 0.1% FWHM at 511 keV, and a 170-512 keV energy window, in which all single scattered coincidences can be selected, was used. Noise and dead time were not included in the simulation process in order to focus on the role that scattered coincidences played in the image quality.

A simplified Deluxe Jaszczak phantom [69, 70] was simulated as shown in Figure 3.4.This cylindrical water phantom has a diameter of 80 mm and contains 3 hot disks (with diameters of 3 mm, 6 mm, 9 mm) and 1 cold disk (with diameter of 12 mm). The hot-to-background ratio was set to 4:1 in this simulation. Attenuation correction was ignored in this chapter due to the small phantom being used.

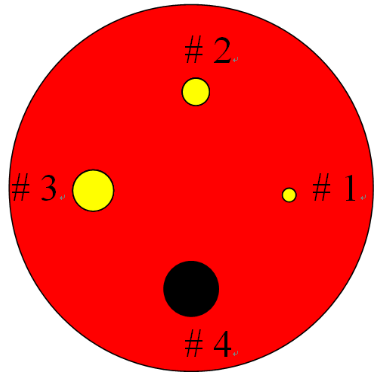

Figure 3.4 A simplified Deluxe Jaszczak phantom. The three yellow circles represent hot disks with diameters of 3 mm, 6 mm and 9 mm respectively. The black circle represents a cold area with diameter of 12 mm. The red area represents the 40 mm radius cylindrical water phantom. The hot-to-background ratio is 4.

Images were reconstructed within a 99× 99 pixel matrix, with a pixel size of 1×1 mm^2. The contrast recovery ratio of the reconstructed images was analyzed using the mean value of the disks relative to the local background while the noise was calculated using the relative standard deviation (RSD) of a 10 mm diameter circular region of interest (ROI) located in the center of the phantom image. Two concentric circular ROI with diameters of 6 mm and 8 mm were defined within the #3 and #4 disks respectively. Annular ROI with a 20 mm outer diameter and an inner diameter of 9 mm and 12 mm respectively were drawn in the background around disks #3 and #4. The local contrast recovery coefficient (CRC_{local}) was defined by

$$CRC_{local} = \frac{\frac{H}{B}-1}{R-1} \quad \text{.................(3.4)}$$

where *H* is the average values within the ROI in the hot disk, *B* is the average value in the annulus around the disk, and *R* is the experimental set-up hot-to-background ratio. For the cold source, CRC_{local} is defined by

$$CRC_{local} = 1 - \frac{C}{B} \quad \text{..............(3.5)}$$

where C was the average value of the ROI in the cold disk.

For the purpose of evaluation, a point on the CRC curve was determined which was the shortest distance from the CRC curve to the point (0,1) defined by an ideal CRC of 1 and a RSD of 0.

As comparisons, the same data were also reconstructed by using the conventional ML-EM (LOR-MLEM) method, which is developed based on the single scatter simulation approach. Firstly, the spatial distribution of single scatter events will be estimated by Monte Carlo method. Then the estimated scatter is scaled globally to ensure a good fit between the estimated scatter and the measured projections. Lastly the true coincidences can be obtained by subtracting the scatter event events from the prompt coincidences and reconstructed in MLEM algorithm interactively.

3.2.3.1 The feasibility test of images reconstructed from only scattered coincidences

To illustrate that scattered coincidences can be used to reconstruct PET images, 10^6 scattered coincidences were simulated to reconstruct PET images by using the GS-MLEM method. As comparisons, these 10^6 scattered coincidences as well as another 10^6 true coincidences were also reconstructed respectively by using the conventional ML-EM (LOR-MLEM) method.

3.2.3.2 Comparison of images reconstructed by using GS-MLEM and LOR-MLEM with different scattering fractions

The scatter fraction is a function of the geometry of scanner, the density and the size of the patient as well as the energy window employed. To compare images reconstructed with different scatter fractions, we simulated 3×10^5 true coincidences and added scattered coincidences to obtain the required data with scatter fractions ranging from 0-60% using the same phantom. The simulation data we used are more artificial than real; however, it serves the goal of this research to investigate the relative value of the proposed algorithm for different fractions of scattered coincidences to the image quality while at the same time removing unwanted complexities resulting from more realistic simulations.

3.2.3.3 Evaluation the different energy thresholds of scattering coincidences on image quality

The scatter fraction affects contrast and noise of images. As more scattered coincidences are included in the image reconstruction, the noise will decrease but so will the contrast. However, the strength of the proposed method lies in its ability to recover contrast while keeping noise low. The trade-off between contrast and noise (for a particular scatter fraction) can be adjusted by varying the scattered photon energy threshold. Photons scattered through large angles may still be of value close to the periphery of the phantom. In this work, the TCA area threshold defined based on the intersection of the area encompassed by the TCA and the image matrix has been proposed. This is similar to using a scattered energy threshold, but enables both energy and spatial information to be involved to full advantage. A total of 6×10^5 coincidences with a scattering fraction of 50% were used to test how the varying thresholds enable the GS method to trade-off between the contrast and noise. By setting different thresholds and calculating the intersection areas between the TCA and the image matrix, the data were generated and used for reconstruction.

3.3 Results

3.3.1. Feasibility test of reconstructing PET images from only scattered coincidences

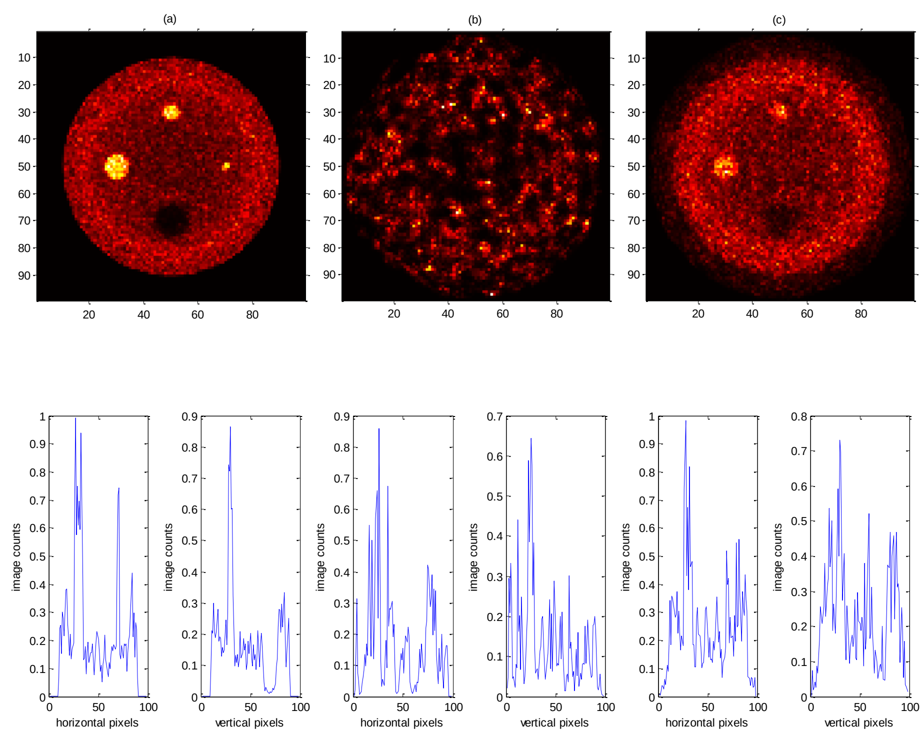

Figure 3.5 (a) The image reconstructed from10^6 true coincidences by using the LOR-MLEM with 36 iterations. (b) The image reconstructed from 10^6 scattered coincidences by using the LOR-MLEM approach which assumes these events are true coincidences. (c) The image reconstructed from the same scattered coincidences dataset as in (b), but by using the GS-MLEM approach with 62 iterations. The second row plots the profiles through above images in the horizontal and vertical direction passing through the center of the images respectively.

Figure 3.5 (a) displays a typical image reconstructed from true coincidences by using the conventional ML-EM (LOR-MLEM) algorithm. Figure 3.5 (b) shows that the same algorithm was incapable of producing recognizable images from only scattered coincidences since the LOR assigned for each scattered coincidence no longer pass through the annihilation position. This figure illustrates why scattered photons are traditionally considered contributing only noise to the resultant image and are, where possible, typically eliminated. The initial experiments as shown in Figure 3.5 (c) demonstrated that the proposed algorithm was capable of producing an image entirely from scattered coincidences. While this figure is not as good as the image in Figure 3.5 (a), it still adequately represents the activity distribution. There is still blurring evident in the scattered photon reconstruction and image converges at least 2-3 times slower. From the profiles under the corresponding images, the image reconstructed from only scattered events has a decreased contrast and noisier background compared with that from true coincidences. Figure 3.5 (c) was used to illustrate the feasibility of reconstructing an image from only scattered coincidences. However, in practice, an image would be reconstructed by incorporating both true and scattered events instead of only from scattered coincidences. We hypothesize that including scattered coincidences in the reconstruction provides greater advantages than simply rejecting them, and the results will be shown in the next section.

3.3.2 Comparison of images reconstructed by GS-MLEM and LOR-MLEM with different scatter fractions

Figure 3.6 shows the CRC curves for the #3 (largest hot disk) versus the relative standard deviation of the background obtained by varying the number of iterations. Figure 3.7 is similar except that it shows the results for #4 (the cold) source. The CRC curves for images reconstructed by using the GS-MLEM algorithm were always above those generated by the LOR-MLEM algorithm. Unlike the CRC curves for the LOR-MLEM algorithm that decrease with increasing scatter fraction, the CRC curve for the GS-

MLEM algorithm generally increased with increasing scatter fraction. For the hot disk, this trend reversed beyond the point where the CRC curve for the GS-MLEM intersected with that of the CRC for reconstructions from only true coincidences. For the cold disk, this reversal was not observed. This reduction in CRC was small and occurred only for iterations beyond the evaluation point. For scatter fractions from 10% to 60%, the evaluation points on the CRC curve for the hot disk were 0.5%-3.0% greater than those obtained using only true coincidence data and were 3.0%-24.5% greater than the corresponding curves reconstructed by using the LOR-MLEM algorithm. The noise was reduced by 0-1.7 % in comparison with the true coincidences data and was 2.0%-12.0% less than that produced by LOR-MLEM method with the same scatter fraction. For scatter fractions between 10% and 60%, the evaluation points for the cold disk had a CRC 0-3.5% greater than the curves calculated using only true coincidences and were 4.0%-24.0% greater than the LOR-MLEM method. The noise at the evaluation point was 0-1.6% less than that obtained using only true coincidences and was 0.5%-8.3% less than that calculated using the LOR-MLEM method with the same scatter fraction. This trend is consistent with the position that the scattered coincidences contribute to noise in the conventional PET image reconstruction and that as the scatter fraction increases, the image quality deteriorates.

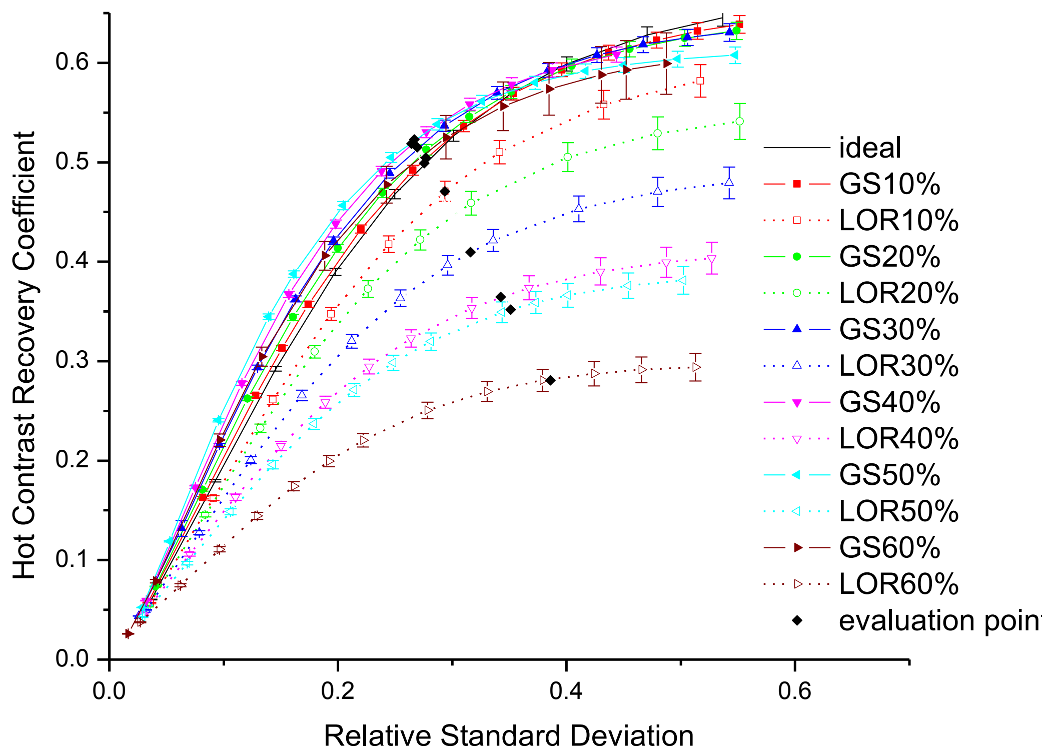

Figure 3.6 The CRC curves for # 3 disk versus the relative standard deviation of the background by varying the number of iterations. The CRC curves shown with filled symbols represent the images reconstructed by GS-MLEM with different scattering fractions. The void symbols in the same style correspond to images with the same scattered fraction, reconstructed by LOR-MLEM. The CRC for true coincidences is shown as a solid line for comparison. The diamonds reflect the optimal points on the CRC-RSD curves.

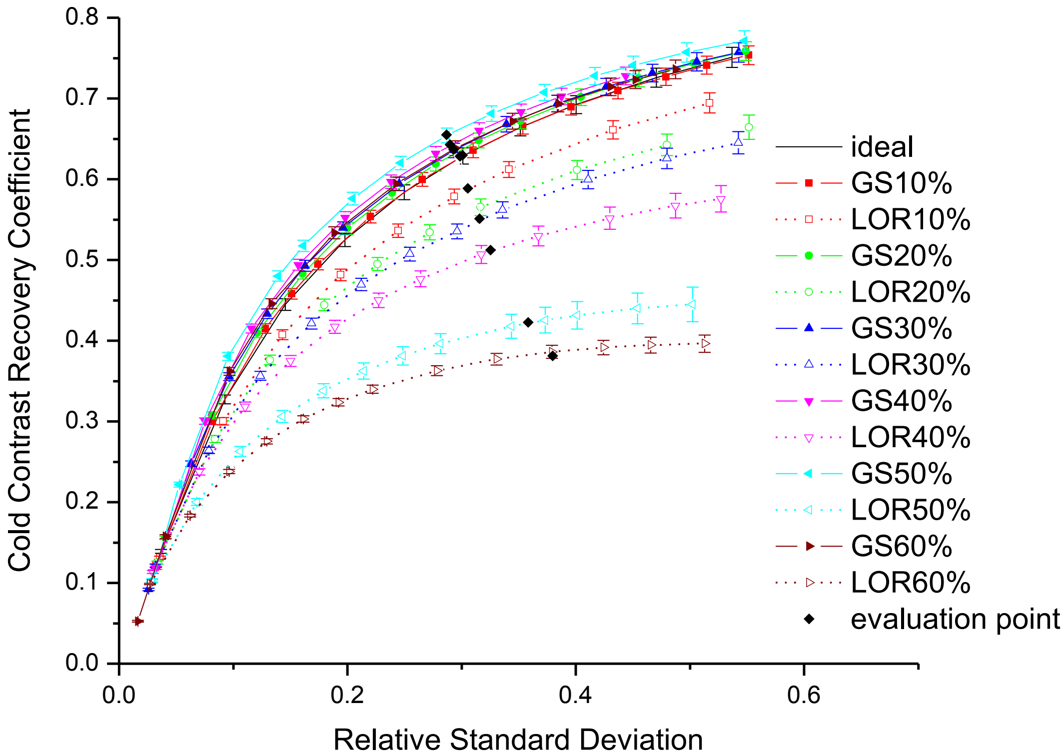

Figure 3.7 The CRC curves for the #4 (cold) disk versus the relative standard deviation of the background by varying the number of iterations. The CRC curves shown with filled symbols represent the images reconstructed using the GS-MLEM with different scattering fractions. The void symbols in the same style correspond to images with the same scattered fraction, reconstructed by LOR-MLEM. The CRC for the true coincidences is shown as a solid line for comparison. The diamonds reflect the optimal points on the CRC-RSD curves.

3.3.3. Evaluation the different energy thresholds of scattered coincidences on image quality

Figure 3.8 plots the CRC of #3 (the largest source) for different TCA area thresholds as a function of the relative background standard deviation obtained by varying the number of iterations. Figure 3.9 is similar, except that it shows the results for the #4 (cold) source. The results show that the value of the CRC for images reconstructed by using the GS-MLEM method were always greater than those obtained with a conventional LOR-

MLEM. For the GS-MLEM method, the evaluation point (Point #1 in Figure 3.8) for the hot disk had a CRC that was 2.5% better than images reconstructed with true coincidence data only (which is an idealistic upper limit on existing algorithms) (Point #2 in Figure 3.8), and was 13.0% greater than images reconstructed by using the conventional LOR-MLEM algorithm (Point #3 in Figure 3.8). The image noise was 2.0 % less (Point # 1 in Figure 3.8) than the ideal reconstruction from trues (Point #2 in Figure 3.8) and was 7.0 % less than the LOR-MLEM approach (Point #3 in Figure 3.8). For the cold source, the evaluation point for the GS-MLEM approach (Point #1 in Figure 3.9) had a CRC that was 5.0 % greater than the CRC obtained with the ideal true coincidence calculation (Point #2 in Figure 3.9) and 18.0 % greater than the LOR-MLEM method (Point #3 in Figure 3.9). For the cold source, the noise at the evaluation point by using the GS-MLEM method (Point #1 in Figure 3.9) was 2.0 % less than the ideal reconstruction from trues (Point #2 in Figure 3.9) and was 8.0 % less than the LOR-MLEM approach (Point #3 in Figure 3.9). Virtually no difference was found between the CRC curves for thresholds of 91.8% and 100%. The evaluation CRC/noise point for the hot source occurred for thresholds close to 100% of the matrix size while the evaluation point for the cold source was optimal when the threshold was set to 10.2% of the matrix size. The evaluation of the contrast recovery point for the hot disk approached the true value as the threshold approaches zero, but the CRC for the cold source still showed an improvement for thresholds approaching 100%.

Figure 3.10 (a) displays the image reconstructed from 3×10^5 true coincidences using the conventional LOR-MLEM method. Figure 3.10 (b) shows the image reconstructed from the same true 3×10^5 coincidences plus 3×10^5 scattered coincidences that fall into the 350-511 keV energy window and reconstructed using the conventional LOR-MLEM algorithm as a comparison. Figure 3.10 (c) shows the image produced by 6×10^5 coincidences with 50% scatter fraction and a threshold of 100% reconstructed using the GS-MLEM method.

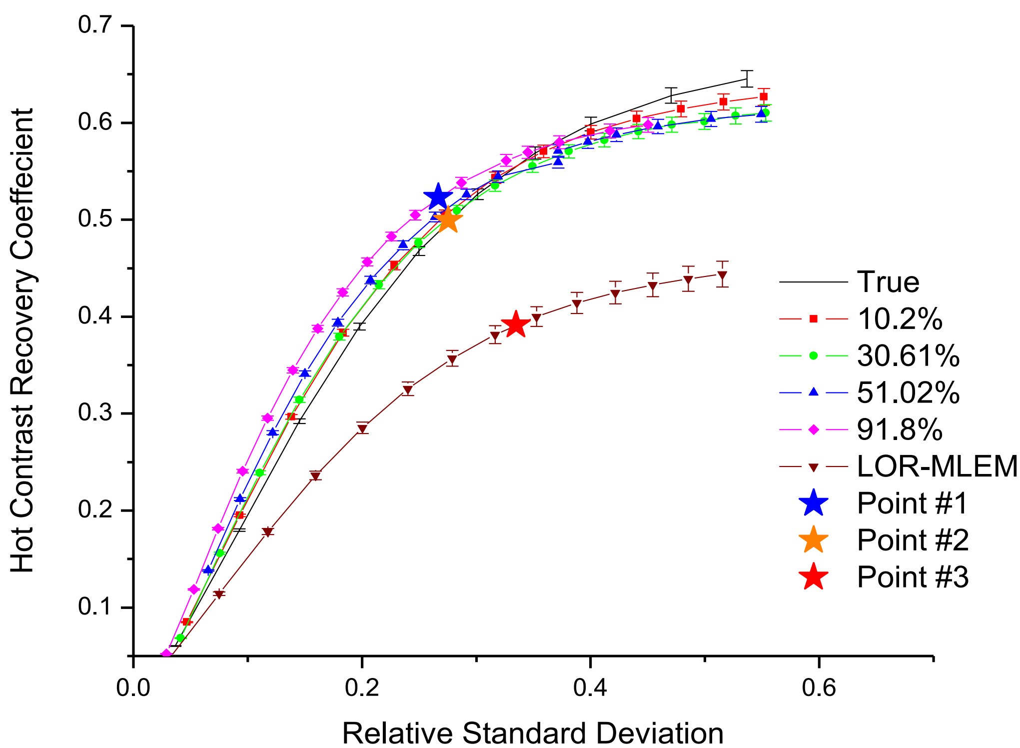

Figure 3.8 The CRC curves for the #3 (largest hot) disk calculated from only trues, with 50% scatter fraction calculated using the conventional LOR-MLEM approach, and with the GS-MLEM approach using different thresholds defined by the ratio of the area of intersection between the TCA and image matrix to the total image matrix area. These curves were obtained by varying the number of iterations. Points #1, #2 and #3 identify the evaluation points for reconstructions using GS-MLEM method, only trues and the LOR-MLEM respectively.

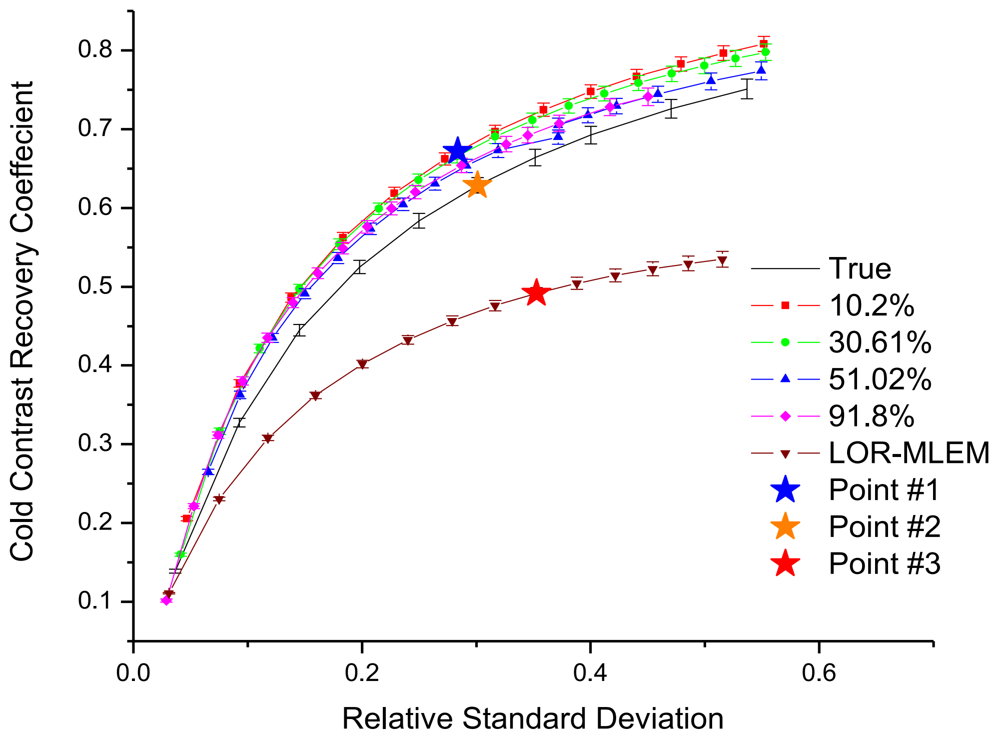

Figure 3.9 The CRC curves for the #4 (cold) disk calculated when only trues are present and with 50% scatter fraction calculated using the conventional LOR-MLEM approach and with the GS-MLEM approach using different thresholds defined by the ratio of the intersection area between the TCA and image matrix to the total image matrix area. These curves were obtained by varying the number of iterations. Points #1, #2 and #3 identify the evaluation points for reconstruction using GS-MLEM method, only trues and the LOR-MLEM respectively.

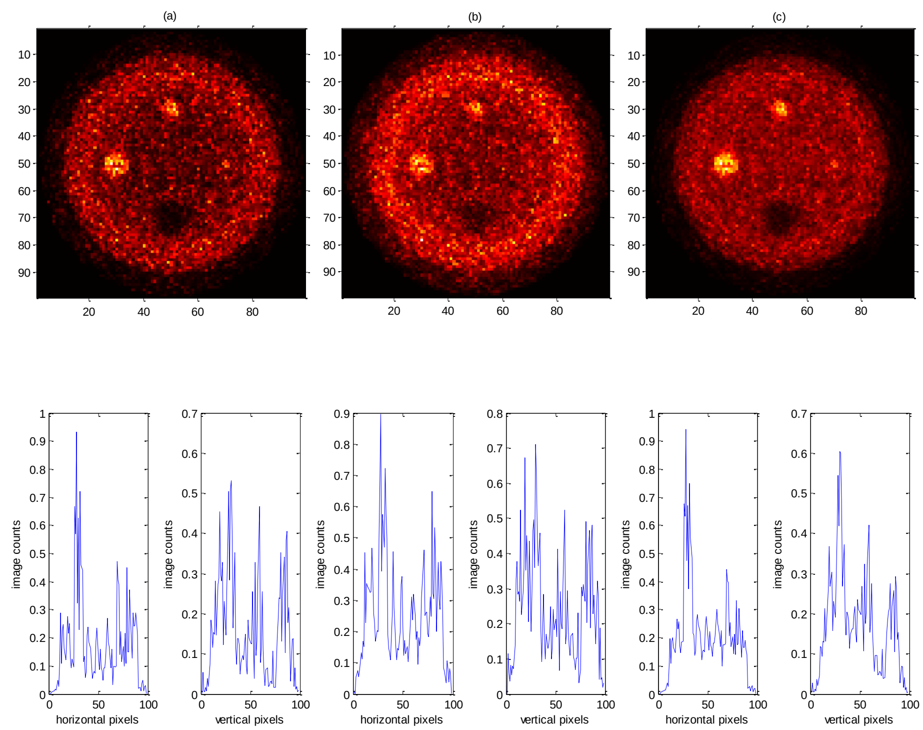

Figure 3.10 (a) The image using 3×10^5 true coincidences reconstructed by using a LOR-MLEM reconstruction algorithm. (b) The image using the same true 3×10^5 coincidences plus 3×10^5 scattered coincidences that fall into the 350-511 keV energy window reconstructed by using the conventional LOR-MLEM algorithm as a comparison. (c) The image using 6×10^5 coincidences with a 50% scatter fraction reconstructed by using the GS-MLEM algorithm. The second row shows the profiles of above images along horizontal and vertical direction passing through the center of the images respectively.

3.4 Discussion

A novel PET reconstruction algorithm has been proposed, which can incorporate both true and scattered coincidences into the reconstruction process. The initial results have shown that including scattered coincidences in the reconstruction is more advantageous than simply rejecting them in the ideal energy resolution scenario.

It has been shown that the activity distribution can be extracted from only scatter events as shown in Figure 3.5 (c). The image in Figure 3.10 (c) is still idealistic and far from optimized, but these results show that the proposed method produces an image with a more homogeneous background, sharper edges, reduced noise and with improved contrast (for both hot and cold disks), relative to both conventional algorithm (which degrades in the presence of scatter) and the idealistic situation (only true events used). Algorithms that incorporate scatter correction will move closer to the idealistic response curve but will never exceed it. Thus, including scattered photons directly into the reconstruction could eliminate the need for (often empirical) scatter corrections required by conventional algorithms and increase image contrast and SNR. This could be used to either improve the diagnostic quality of the images and/or to reduce patient dose and radiopharmaceutical cost.

The results in Section 3.3.3 show that an additional advantage of the GS-MLEM algorithm is that a threshold can be used to adjust contrast and noise in order to optimize the role that scattered coincidences play in the image reconstruction process. At the optimal threshold, adding scattered coincidences into image reconstruction appears to result in minimal (if any) loss in spatial resolution while significantly improving the SNR and contrast recovery. The results show that by appropriately including a greater number of scattered photons in the reconstruction, improvements in both contrast and noise can be achieved. In addition, this threshold also can remove partial coincidences scattered within detectors or in the gantry, which usually have relatively larger scattering angles and unusually short distances between scattering position and detector positions. The TCA for these situations usually covers the whole image space and can be removed from the reconstruction dataset by employing the proposed TCA area threshold.

Similar to conventional energy-based scatter correction methods, the accuracy of the proposed method is limited by the energy resolution of the detector. In conventional scatter correction based methods, the ability to distinguish and reject scattered coincidences is limited by energy resolution. In this proposed method the energy resolution of detectors determines the confidence with which the TCA can be defined for each scattered coincidence, which in turn affects the locus of the possible scattering positions and hence the annihilation position. The locus is sensitive to the energy of the detected photons and a small uncertainty in the energy of the scattered photon can result in a significant difference in the shape of the TCA and the position of the source. For example, if the detector’s energy resolution is 4% at 511 keV, the maximum uncertainty in the calculated area between the TCA is approximately 21% for a scattered photon energy of 450 keV. Thus developing a detector with high energy resolution and weighting the spatial probability distribution of the annihilation position by using both the patient outline [71, 72] and the energy resolution of the detector will be important future work.

Guerin et al. [6] indicated that neglecting the effect of multiple scattered coincidences was not a serious source of error. In practice, multiple scattered events cannot be distinguished from single scattered events on the basis of the energy of the scattered photons. Even though the relation between scattered energy and scattering angle cannot be connected by Compton scattering equation for multiple scattered coincidences, we can propose to use a synthetic scattering angle for multiple scattered events based on the scattered photon energy. In addition, the uncertainty in the energy of the detected photon as a result of the limited energy resolution of the detector is more challenging for multiple scattered events when trying to determine the locus of possible scattering positions. Corrections for randoms can be addressed by adding a factor to the forward projection in the algorithm as do most existing methods. The data model used to derive the reconstruction algorithm can be improved by including the electron density and tissue attenuation. The impact of these on the quality of the reconstructed images is beyond the scope of this chapter and will be the focus of a separate study. Since the TCA is a function of scattering angle and detector positions, which will be calculated for each detected coincidence in the reconstruction algorithm, the computational time is currently 3-4 times longer when compared with a conventional MLEM algorithm. However, this algorithm still needs to be optimized for calculation efficiency.

In summary, considering the challenges mentioned above, the following chapters will be arranged as following: Chapter 4 will investigate further improvements to PET image quality by adding a patient/phantom outline as a constraint in the GS algorithm. The uniform attenuation phantom used in this chapter is simple in comparison to anthropomorphic phantoms and may not reflect the complexity of scatter in humans, which will be addressed in Chapter 5. Chapter 6 will introduce a geometrical model to characterize the different probabilities of annihilation positions within TCA to further improve the imaging quality. Chapter 7 will explore the dependency of the image quality on the energy resolution, and adapts the proposed method for non-ideal energy resolution scenarios. The final chapter summarizes and concludes this work and identifies future areas of research.

3.5 Conclusion

A new method that includes scattered coincidences directly into PET reconstruction has been presented and evaluated in this chapter. The results of the phantom study have shown that PET images can be reconstructed from only scattered coincidences. Including scattered coincidences into the reconstruction eliminates the need for scatter corrections while increasing image contrast and reducing noise. A threshold, which depends on both energy and detector positions, is used to adjust the trade-off between noise and contrast in this chapter. The optimal threshold was different for hot and cold sources, but the variation in CRC for the cold source was only weakly dependent on the threshold. Improvements in the CRC and noise for both hot and cold sources could be obtained by maximizing the use of all scattered events.

Chapter 4: Image Quality Improvements When Adding Patient Outline Constraints into a Generalized Scatter PET Reconstruction Algorithm

The material in this chapter has been reprinted and adapted from ISRN Biomedical Imaging, Volume 2013, Hongyan Sun, Stephen Pistorius, "Evaluation of Image Quality Improvements When adding Patient Outline Constraints into a Generalized Scatter PET Reconstruction Algorithm," Copyright (2013), with permission from Hindawi Publishing Corporation.

4.1 Introduction

In Chapter 3 we have shown that true coincidences can be considered to be a subset of scattered coincidences and a GS-MLEM algorithm has been developed to estimate the source distribution from both true and scattered events [73]. This method takes advantage of the kinematics of Compton scattering by connecting the coincidence detectors with two arcs in 2D, which describe the locus of scattering. It can be shown that the annihilation position is encompassed in 2D by TCA or, in 3D by a surface, described by the rotation of these arcs around an axis connecting the detectors. See Figure 3.1.

The annihilation position within the TCA can be further confined by using the patient outline (or a geometrical shape that encompasses the patient outline) as a further spatial constraint. Adding this constraint into the GS-MLEM algorithm speeds up the image convergence and improves the image quality. This work has been presented, in part, at the 2012 IEEE Nuclear Science Symposium and Medical Imaging Conference [72].

This chapter will describe how the patient/phantom outline constraint is introduced into the GS-MLEM algorithm, and will evaluate the contrast and noise properties of the constrained GS-MLEM algorithm as well as the dependency of the proposed method on the accuracy of the patient/phantom outline constraints employed.

4.2 Methods and Materials

4.2.1 Outline Constraint Reconstruction Theory

In PET, the three main sources of photon scatter are 1) patient, 2) detectors, or 3) the gantry and surrounding environment. Patient scatter generally dominates in human imaging, and this work assumes the patient is the only scattering source and ignore the relatively small contribution due to scattering in the gantry and detectors [14, 74].

In such a scenario as illustrated in Figure 4.1, the possible annihilation positions can be further constrained by connecting the intersection points between the TCA and the patient outline, C (furthest from the unscattered photon Detector A) and D (closer to the unscattered photon Detector A) with the unscattered photon Detector A. The position of annihilation is confined to the area encompassed by the TCA, the patient/phantom outline and the line AC (Area CDE as shown in Figure 4.1). If both circular arcs of a TCA for a coincidence intersect with the patient/phantom outlines, the areas used to confine the annihilation positions can be calculated for each circular arc separately in a similar way.

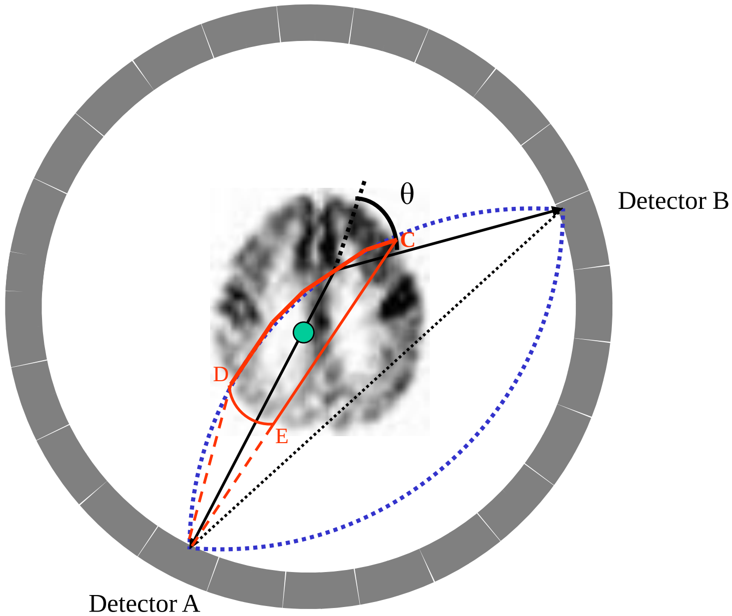

Figure 4.1 In this case, one of the TCA interacts with the patient at Point D (closer to A) and C (further from A). If the extent of the scatter volume is known (the patient outline), the possible annihilation area may be further confined to the area C-D-E encompassed by line CA, TCA, and the outline of the patient.

The patient outline can be estimated in a variety of ways. One approach is to use an external x-ray source or optical system (either laser-based or photogrammetric). In PET/CT or PET/MRI systems the anatomical image provided by the CT or MRI could be used. Alternatively, it may be possible to estimate the constraints using an approximation of the patient outline based on initial iterations or by using a basic geometric shape (say a circle or ellipse) as shown in Figure 4.2. The size of the circle could be chosen from a simple measurement (or estimate) of the patient size or based on earlier iteration images. This resembles the concept of Chang's attenuation correction [75] in PET and SPECT brain imaging.

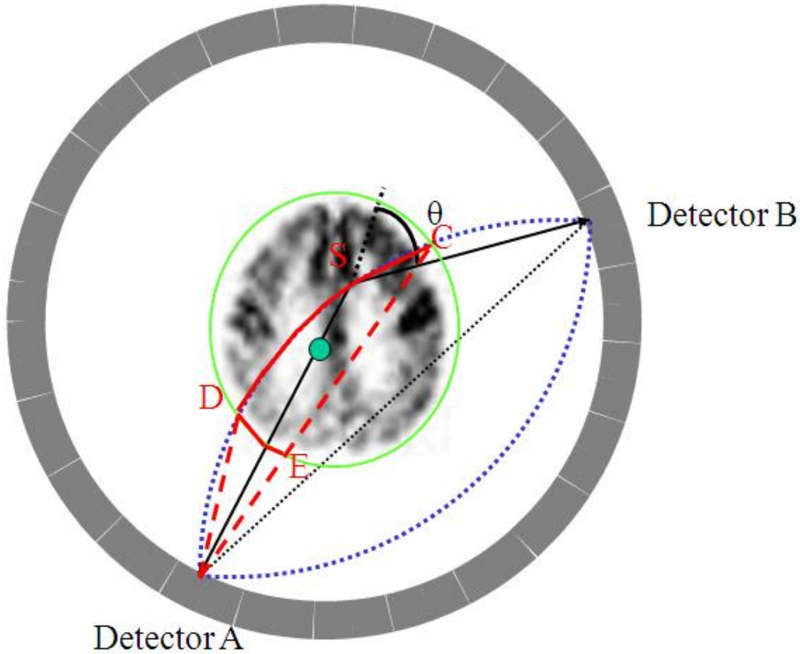

Figure 4.2 The patient outline is replaced by an ellipse which is slightly larger than the patient outline and intersects with TCA at point C (furthest to the unscattered photon detector) and point D (closer to the unscattered photon detector). The possible annihilation positions are confined to the area C-D-E encompassed by line CA, TCA and the ellipse calculated in the same way as the case of patient/phantom outline.

4.2.2 Constrained GS-MLEM algorithm

The expected number of coincidences in which an unscattered photon is observed at A while the other photon is observed at B following a Compton scattering through an angle θ, is determined from:

$$\langle P_{ab}(\theta)\rangle = \tau \oint_A^B [\int_A^S f_x \, dx] \cdot \rho_e(S) \cdot \frac{d\sigma_C^{KN}}{d\theta} \frac{1}{4\pi} e^{-(\int_A^S \mu dl + \int_S^B \mu' dl)} ds \ldots\ldots\ldots(4.1)$$

In the above expression the total number of photons which could reach the scattering point S is obtained by integrating the source f_x from line segment A to C. The possibility that the photons at S undergo a Compton scattering event, is proportional to the electron density at this point weighted by the differential Klein-Nishina electronic cross section. The outer integral sums over all possible scattered points which have been constrained by the patient outline. τ is the acquisition time, μ and μ' are the linear attenuation coefficients for the unscattered and scattered photons.

To reduce the large computational workload, the expected number of detected coincidences is assumed to be linearly proportional to the product of the differential Klein-Nishina electronic cross section and the total activity within area CDE as given by:

$$\langle P_{ab}(\theta)\rangle = C \cdot \overline{\rho_e} \cdot \frac{d\sigma_C^{KN}}{d\theta} \iint_{CDE} f_x \, dy \ldots\ldots\ldots\ldots\ldots(4.2)$$

where C is a constant and $\overline{\rho}_e$ is the mean electron density. Putting this data model into the system model and following the same maximization process as in [1], we can derive the constrained GS-MLEM algorithm in list-mode [43, 44, 65]:

$$\vec{f}_i^{\,n+1} = f_i^n \frac{1}{\sum_{j'=1}^{N} a_{j',i}} \sum_{j=1}^{N} a_{j,i} \frac{1}{\sum_{i'=1}^{p} a_{j,i'} f_{i'}^n} \quad i = 1, \ldots, p \ldots\ldots\ldots\ldots\ldots(4.3)$$

where p is the total number of pixels in the image, N is the total number of coincidences, n is the iteration number, and $a_{j,i}$ is the system matrix accounting for the probability that the j^{th} coincidence detected in the list mode entry comes from Pixel i. To incorporate the patient outline as a constraint in the algorithm, the sum over i is only calculated within the confined areas, instead of the whole area within the TCA.

4.2.3 Phantom Measurement

To make the comparison consistent with Chapter 3 [73], the same PET scanner and phantom (see Figure 3.4) are simulated by GATE [66, 68] in this chapter. The simulated system had a perfect energy resolution with the energy window set to 170 to 512 keV. Noise and dead time were not modeled in the simulation process.

In this initial evaluation of the proposed method, only the coincidences scattered within the phantom were used in the reconstruction. The image quality was evaluated using CRC and RSD, which are defined in Section 3.2.3.

An evaluation point on the CRC curves was determined by the shortest distance from the CRC curve to the point (0,1) defined by the ideal $CRC=1$ and $RSD=0$.

As comparisons, the same data were also reconstructed by using the conventional ML-EM (LOR-MLEM) method, which is developed based on the single scatter simulation approach. Firstly, the spatial distribution of single scatter events will be estimated by Monte Carlo method. Then the estimated scatter is scaled globally to ensure a good fit between the estimated scatter and the measured projections. Lastly the true coincidences can be obtained by subtracting the scatter event events from the prompt coincidences and reconstructed in MLEM algorithm interactively.

4.2.3.1 Evaluation of images reconstructed by using the proposed method with different scatter fraction data

The image quality reconstructed with the phantom outline constraint was compared to the results obtained by using the GS-MLEM algorithm without the phantom outline constraint and to the conventional LOR-MLEM method given in Chapter 3 [73]. Coincidences with scatter fractions ranging from 0 to 60% were randomly simulated by GATE. To be consistent with the previous results, 3×10^5 true coincidences and scattered coincidences with the required scatter fraction were generated. Here, the actual phantom outline (a circle with a radius 40 mm) was employed in the reconstruction process as the outline constraint.

4.2.3.2 Evaluation of image quality using different outline constraint approximations

The improvement in the contrast and noise properties of the reconstructed images was related to the accuracy of the patient/phantom outline used. When the phantom outline constraints chosen are smaller than the actual phantom outline, the confined area may not encompass the annihilation position, which will reduce the image contrast and introduce artifacts. Thus, the minimum, but still most accurate outline constraint should be the actual patient/phantom outline. A larger area can be used to constrain the annihilation position, but will not be optimal. When the constraint outline approaches that of the detector positions, the outline constraint-based GS-MLEM algorithm will approach the non-outline constraint-based algorithms. To evaluate the effect of different constraint sizes on the reconstructed image quality, the patient/phantom outline size is characterized as a function of the ratio of differences between the tested outline constraint and the actual phantom outline size relative to the actual phantom outline size. Therefore the effect of various phantom outline constraints was tested by using a circle with diameters of 84 mm, 90 mm, 100 mm, 120 mm, being 5%, 12.5%, 25%, 50% larger than the actual phantom outline respectively. A total of 6×10^5 coincidences, with a 50% scatter fraction, were generated by GATE and were used by the proposed method with the different outline constraints to reconstruct the activity maps. The images were also reconstructed using the same dataset, but with the GS-MLEM algorithm without the phantom outline constraint and with the conventional LOR-MLEM algorithm, as well as with 3×10^5 true coincidences by using the conventional LOR-MLEM algorithm as a comparison.

4.3 Results

4.3.1 Evaluation of images reconstructed by using the proposed method with different scatter fraction data

To illustrate the performance of the constrained GS-MLEM algorithm, the CRC vs. RSD for different methods/or data for the #3 (largest hot) disk was plotted in Figure 4.3 and the #4 (cold) disk was plotted in Figure 4.4, respectively. The results show that the CRC curves for images reconstructed by using GS-MLEM with phantom outline constraint approach are always above those of the unconstrained GS-MLEM approach and the conventional LOR-MLEM algorithm. The optimal CRC curve for the conventional LOR-MLEM method is at zero scatter fraction, and the curves decrease with increasing scatter fraction. In contrast to that, the CRC curve for the GS-MLEM, both with and without phantom outline constraint, generally increases with increasing scatter fraction. This trend, for the hot disk, changes beyond the point where the CRC curves for the constrained and unconstrained GS-MLEM intersect. However, this reduction in contrast is not obvious and occurs beyond the evaluation point. The same trend for the cold disk is not observed. For the hot disk as shown in Figure 4.3, the GS-MLEM algorithm with phantom outline constraints improved the CRC properties of the reconstructed images by 0.6% to 3.8% compared with the GS-MLEM algorithm without the phantom outline constraint for scatter fraction ranging from 10%-60%. For the same scatter fractions, the results were 4% to 28.6% greater than the corresponding curves reconstructed by using the LOR-MLEM algorithm. The noise of images reconstructed using the GS-MLEM algorithm with phantom outline constraint was 0.7% to 2.6% lower than the corresponding curves using an unconstrained GS-MLEM algorithm and was 2.4% to

14.7% less than that produced by the LOR-MLEM method. For the cold disk, with a scatter fraction of 10% to 60%, the evaluation point for the cold disk using the GS-MLEM algorithm with phantom outline constraint had a CRC 1.1% to 11.6% greater than the curves calculated only using the GS-MLEM algorithm and was 5.1% to 40% greater than the LOR-MLEM method for the corresponding scatter fraction. The noise at the evaluation point for images reconstructed using GS-MLEM with phantom outline constraint was 0.5% to 3.6% less than that obtained using an unconstrained GS-MLEM, and was 1.5% to 11.8% less than that calculated using the LOR-MLEM method with the same scatter fraction.

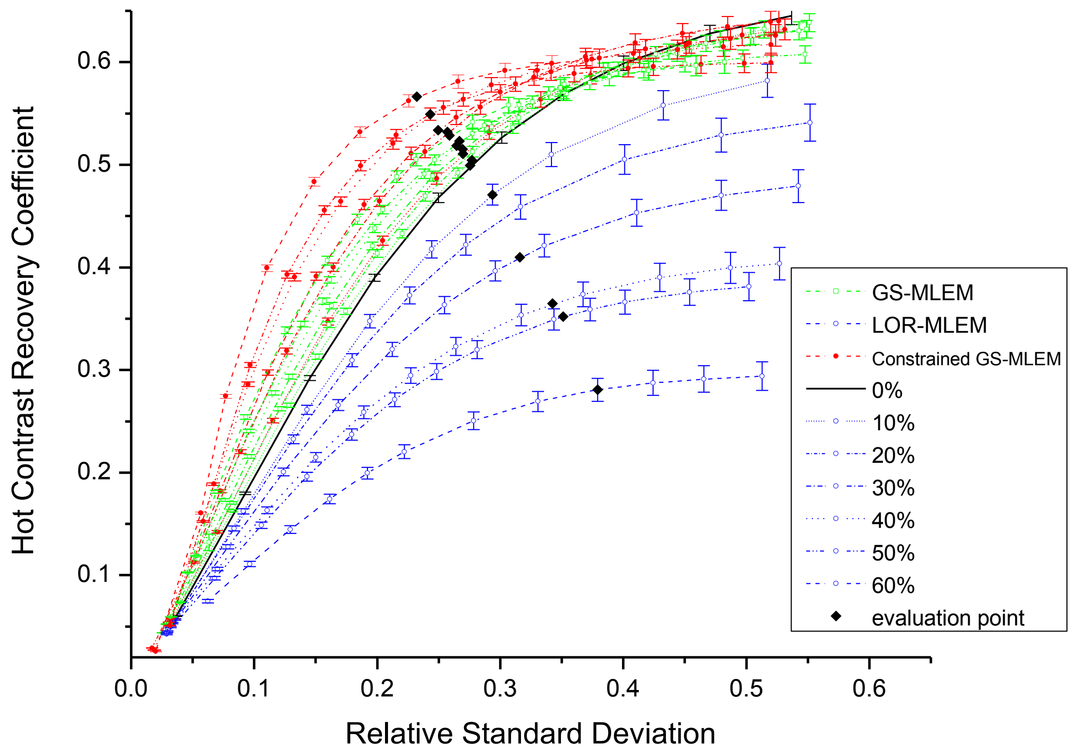

Figure 4.3 The CRC curves of #3 (largest hot) source calculated by using the GS-MLEM with (red lines) /without (green lines) phantom outline constraints, and the conventional LOR-MLEM approach (blue lines) for the scatter fraction ranging from 0-60%.

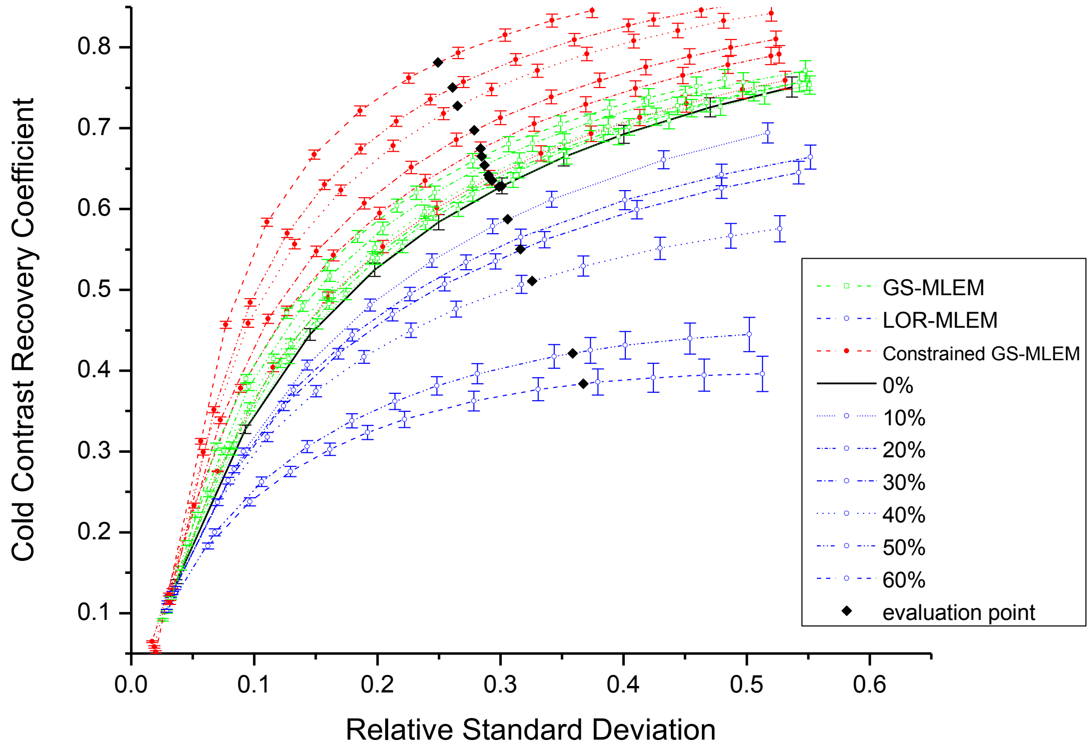

Figure 4.4 The CRC curves of #4 (cold) source calculated by using the GS-MLEM with (red lines) /without (green lines) phantom outline constraints, and the conventional LOR-MLEM approach (blue lines) for the scatter fraction ranging from 0-60%.

Figure 4.5(a) displays the image reconstructed from $6{\times}10^5$ coincidences with a scatter fraction of 50% using the GS-MLEM method with the phantom outline constraint. Figure 4.5(b) shows the image produced using the same number of coincidences and algorithm as in (a) but without the outline constraint. As a comparison, the same $3{\times}10^5$ true coincidences were combined with scattered coincidences from a $3{\times}10^5$ dataset and reconstructed using a conventional LOR-MLEM algorithm with a 350 to 512 keV energy window. The results as shown in Figure 4.5 demonstrate that constrained GS-MLEM (Figure 4.5(a)) can achieve a more uniform background and sharper edges than that of the unconstrained GS-MLEM method (Figure 4.5(b)), which in turn is superior to that the conventional LOR-MLEM method (Figure 4.5(c)).

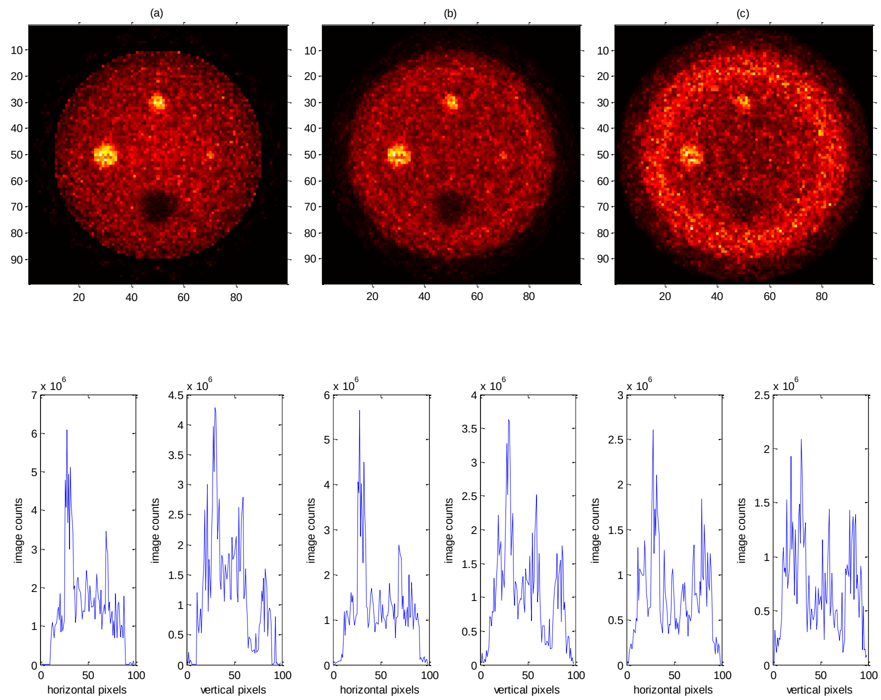

Figure 4.5 (a) The image using 6×10^5 coincidences with a scatter fraction of 50% by using the GS-MLEM with patient/phantom constraint method. Figure 4.5(b) The image using the same data as (a) and by the unconstrained GS-MLEM method; Figure 4.5(c) The image from the same true 3×10^5 coincidences plus 3×10^5 scattered coincidences that fall into the 350 to 511 keV energy window and was reconstructed using the conventional LOR-MLEM algorithm as a comparison. The second row shows profiles of above images passing through the center of the images in the horizontal and vertical directions respectively.

4.3.2 Evaluation of the dependency of the proposed algorithm on the accuracy of the outline constraints

Images with different phantom outline constraints were also reconstructed to evaluate the dependency of the proposed algorithm on the accuracy of the phantom outline constraints. The CRC curves of the #3 (largest hot) disk for different phantom outline constraints as a function of the relative background standard deviation were obtained by varying the number of iterations as shown in Figure 4.6. The same result for the #4 (cold) disk can be seen in Figure 4.7. For the hot disk, the CRC curves for the GS-MLEM method with phantom outline constraints decrease as the phantom outline constraints increase up to the point where the CRC curves for the GS-MLEM method intersect with that of true coincidences. This intersection was not observed for the cold disk, but the same trend was observed. All the CRC curves with phantom outline constraints were above those that did not use phantom outline constraints. The CRC and RSD for the evaluation points on each CRC curve are plotted as a function of the relative increase of radii of the phantom outline constraints to the phantom's actual radius, for the hot and cold disks in Figure 4.8 and Figure 4.9 respectively. As the relative radius increase from 5% to 50%, the CRC for the hot disk reduced by 2% while noise increased 0.5%. For the cold disk, the CRC reduced by 4.5% and noise increased by 1.3%. For both the hot and cold disks, the CRC varied slowly when the relative radius was increased by less than 12.5% (corresponding to an outline constraint with radius 45 mm), when compared to the change for the relative radius increase from 12.5% to 50%.

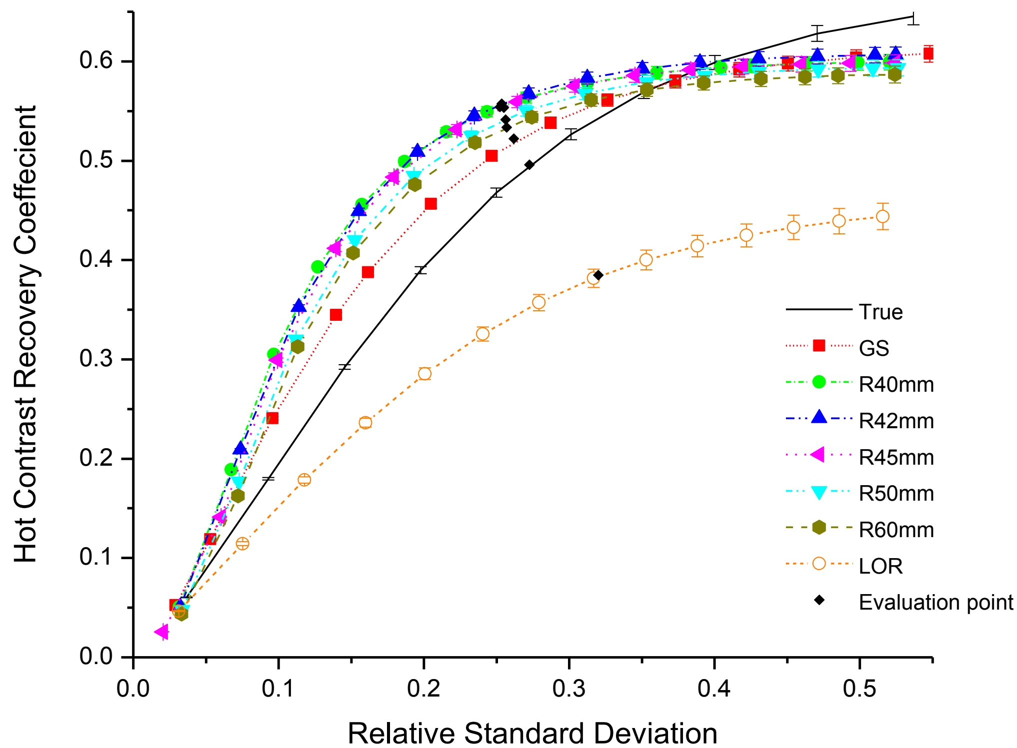

Figure 4.6 The CRC curves of #3 (largest hot) disk calculated using the GS-MLEM with different phantom outline constraints. The CRC for 3×10^5 true coincidences and 6×10^5 coincidences with 50% scatter fraction by using the conventional LOR-MLEM were also reconstructed as a comparison.

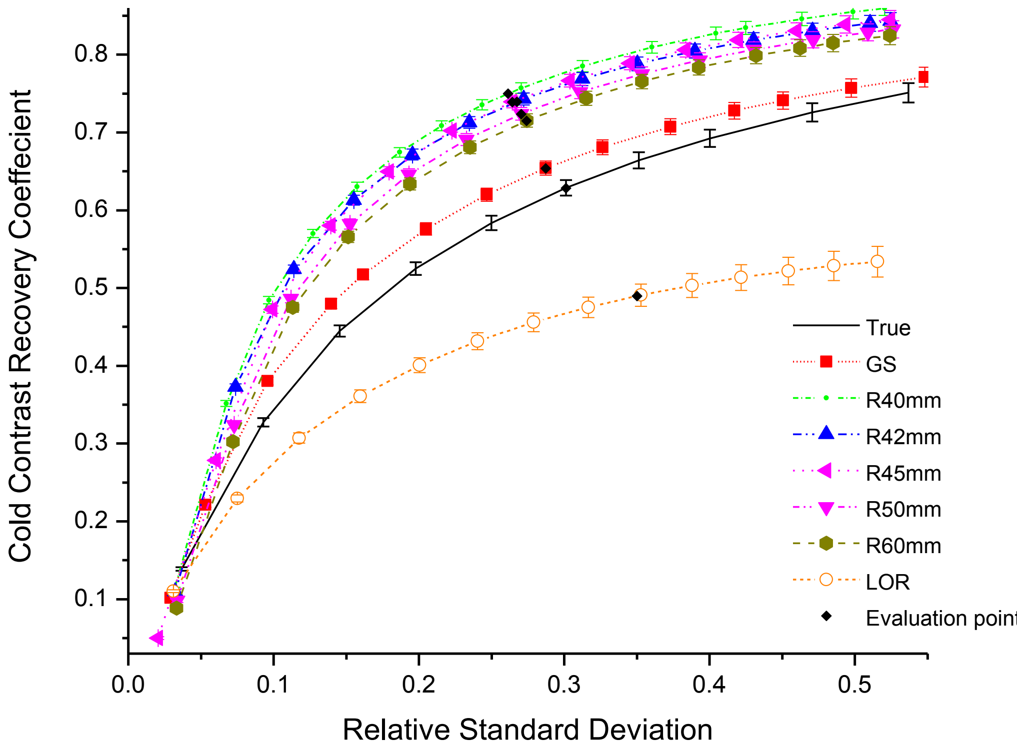

Figure 4.7 The CRC curves of #4 (cold) disk calculated using the GS-MLEM with different phantom outline constraints. The CRC for 3×10^{5} true coincidences and 6×10^{5} coincidences with 50% scatter fraction by using conventional LOR-MLEM were also reconstructed as a comparison.

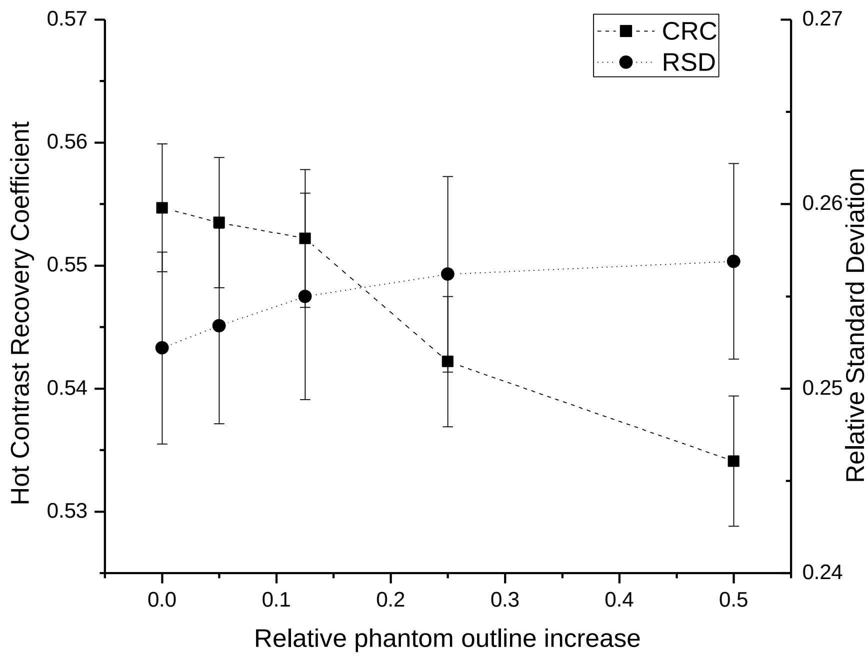

Figure 4.8 The CRC and noise properties of #3 (largest hot) disk as a function of relative increase of radii of the phantom outline constraints for the evaluation points in Figure 4.6.

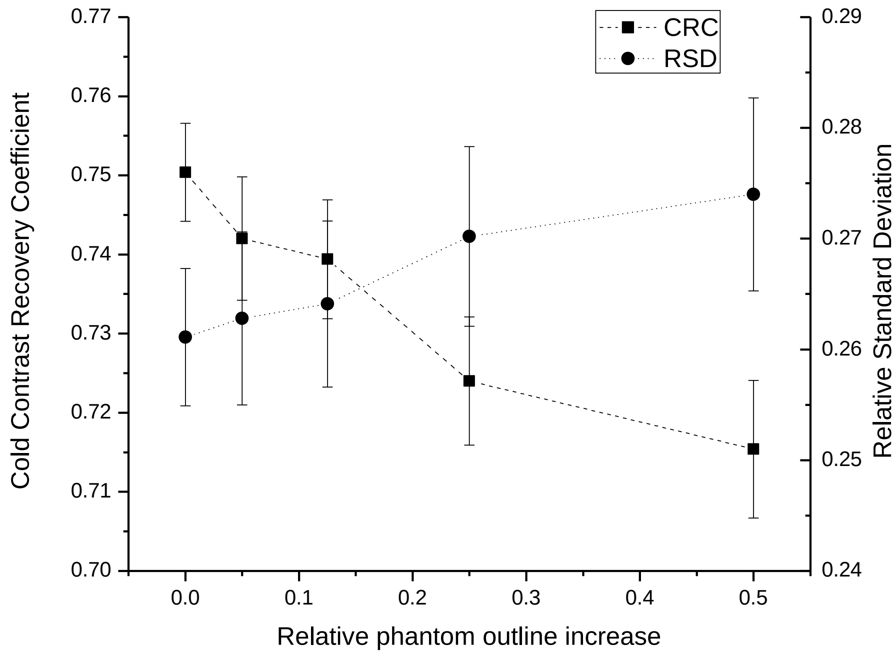

Figure 4.9 The CRC and noise properties of #4 (cold) disk as a function of relative increase of radii of the phantom outline constraints for the evaluation points in Figure 4.7.

4.4 Discussion

Chapter 3 [62, 72, 73, 76] and this chapter have demonstrated that scattered coincidences can be used in the PET imaging reconstruction by taking advantage the individual photon energy. Conti et al. [60] have taken of advantage of the time difference of scattered photons in a time of flight PET and applied this knowledge to refine the physics model to describe the annihilation position. This work included the patient/phantom outline as a constraint to the physics model to further confine the possible annihilation position. The results have shown that the contrast of the reconstructed image was improved while noise was reduced. Since this method no longer considers scatter coincidences as noise, more data is available, and a lower energy window can be applied, thus improving both the system sensitivity and image quality.

The improvement in the reconstructed image quality is due to the annihilation position being confined into a more accurate area (or volume in 3D) by adding the patient outline as a constraint. As expected, the contrast and noise properties will degrade as the accuracy of the patient outline constraint continues compromising, which is illustrated in Figure 4.8 and Figure 4.9. However, the results for the evaluation of different outline constraints on image quality have shown that uncertainties in defining the patient/phantom outline are not a significant obstacle when implementing the proposed method. As the uncertainty of the patient outline further increases, the benefit to the reconstructed image quality will be lost.

This method is based on the assumption that the patient scattering dominates detector, gantry and surrounding environment scattering, which is true in human imaging [4]. In this initial test of the proposed method, we carried out this work in 2D and only the coincidences scattered within phantom were selected to show the principle of the proposed method and at the same time reduce the complexity of the mathematics. This approach could be implemented in 3D where it could be of even greater value.

As discussed in Chapter 3, the TCA are calculated using the detector positions and the scattering angle which is closely related to the scattered photon energy. The accuracy with which the locus of the TCA assigns the possible scattering positions and encompasses the annihilation position will, therefore, depend on the energy resolution of the detectors. The area defined using scattered photon energy with a large uncertainty may not encompass its annihilation position or may overestimate the confined area, resulting in artifacts or blurring of the reconstructed images. The effects of energy resolution on the proposed method will be investigated in Chapter 7.

4.5 Conclusion

Previous work demonstrated that scattered coincidences can be directly included into the reconstruction process. The results of this chapter show that further improvements in the contrast and noise properties of the reconstructed images can be made by including the patient outline into the reconstruction algorithm as a constraint.

Chapter 5: Attenuation Correction for a PET Generalized Scatter Reconstruction Algorithm

5.1 Introduction

In Chapter 3 and Chapter 4, we proposed a generalized scatter (GS) reconstruction algorithm which considered true coincidences as a subset of scattered coincidences and uses both true and scattered events in a self-consistent way to extract the activity distribution [73].

In order to obtain quantitatively accurate PET images, adequate correction of detected events for the attenuation caused by different tissues is essential [1, 77]. Traditionally, the attenuation coefficients are measured by employing a transmission rod source or by using data provided by an x-ray CT or MR system [63]. CT data can provide accurate attenuation coefficients at diagnostic energies. The energy difference between PET and CT requires the diagnostic CT image to be converted, in a non-linear fashion, to electron density in order to obtain an accurate PET attenuation correction [37]. Some attempts have been made to produce attenuation maps from MR sequences [38]. However, there is no direct relationship between the MR image and the PET attenuation map, as MR images are a function of proton spin while PET attenuation is dependent on electron density. In this chapter, the process of generating the PET attenuation map is not considered, and it is assumed that an effective method exists. Once the distribution of attenuation coefficients in the tissue is known, the attenuation correction of PET images created using true coincidences is straightforward [78].

Similarly, artifacts will appear in the images reconstructed from scattered coincidences if the attenuation of the scattered photons is not taken into account. As the size of the object increases, this effect becomes more pronounced. The conventional strategies for the attenuation correction of true coincidences are not directly applicable to scattered coincidences. For a scattered event, the two annihilation photons travel along a 'broken' LOR, and the scattering position cannot be singularly determined. Only the scattering locus (TCA) can be assigned as shown in Figure 3.1. To our knowledge, no effective attenuation correction method for PET scatter has been published. This chapter will report on the methods developed to correct for the attenuation of scattered coincidences and evaluates the reconstructed image quality obtained with the proposed attenuation correction.

5.2 Methods and Materials

5.2.1 Attenuation correction and reconstruction theory

The expression for the mean number of the detected scattered events $<P_{AB}(\theta)>$ in Equation (3.1) works for a small PET scanner when evaluating the feasibility of the GS reconstruction algorithm. To adapt this expression to the human-size PET system, more factors need to be taken into account. As illustrated in Figure 3.1, the new expression of $<P_{AB}(\theta)>$ following the single scatter simulation (SSS) algorithm [24, 79] has been updated as:

$$\langle P_{AB}(\theta)\rangle = \tau \int_{TCA} \epsilon_{AS}\epsilon'_{BS}\left(\frac{\sigma_{AS}\sigma_{SB}}{4\pi R_{AS}^2 R_{SB}^2}\right)\cdot \rho_e(S)\cdot \frac{d\sigma_C^{KN}}{d\Omega}\cdot I_s \cdot e^{-\left(\int_A^S \mu dl + \int_S^B \mu' dl\right)} dV_s$$

……………………………………………………………………………..……………..(5.1) where Tau (τ) is the acquisition time. ϵ_{AS} and ϵ'_{BS} represents the detecting efficiencies for Detectors A and B, which depend on the angle of the photon incidence and the photon energy. The geometrical cross sections are denoted by σ_{AS} and σ_{SB} for the photon incident to Detector A along AS and for the photon incident to Detector B along SB, while their distance from the scatter point are R_{AS} and R_{SB} respectively. $\rho_e(S)$ is the electron density at one of the possible scattering points S and $d\boldsymbol{\sigma}^{KN}{}_C/d\boldsymbol{\theta}$ is the Klein-Nishina electronic cross-section. μ and μ' are the linear attenuation coefficients for the unscattered and scattered photons respectively. I_s represents the coincident photon fluence that reaches one of the possible scattered positions S, calculated by integrating the source activity $f(x)$ from A to S:

$$I_S = \int_A^S f(x)\, dx \text{.................}(5.2)$$

Different from the single scatter simulation (SSS) algorithm [24, 79] , Equation (5.1) only integrates along TCA which depicts the locus of all the possible scattering positions in 2D.

Successful detection of a scattered coincidence requires the simultaneous observation of both the unscattered and scattered photons, which depends on the combined paths AS and SB. AS is the path of the unscattered photon. The probability that the two photons are detected in a coincidence is independent of the source position on this path. SB is the path for the scattered photon, and the attenuation coefficient for materials on this path was obtained by linear interpolation of the published NIST data [80]. The attenuation coefficient at S can be integrated along the two broken LORs, AS and SB. The mean attenuation coefficient for a scattered coincidence were obtained by averaging the attenuation for all possible scattering positions scribed by the TCA, weighted by the photon fluence and electron density at each scattering position:

$$\overline{Att} = \frac{\int_{TCA} \epsilon_{AS}\epsilon_{BS}^{'}\left(\frac{\sigma_{AS}\sigma_{SB}}{R_{AS}^2 R_{SB}^2}\right)\cdot\rho_e(S)\cdot I_S\cdot e^{-\left(\int_A^S \mu dl+\int_S^B \mu^{'} dl\right)} dV_S}{\int_{TCA} \epsilon_{AS}\epsilon_{BS}^{'}\left(\frac{\sigma_{AS}\sigma_{SB}}{R_{AS}^2 R_{SB}^2}\right)\cdot\rho_e(S)\cdot I_S dV_S} \ldots\ldots(5.3)$$

In the above equation, the parameters that are not specific to the scattering point S have been cancelled out. To reduce the computational load further, we assumed that the variations of the detector efficiencies, photon incident cross-sections, the photon fluence f_s and electron density ρ_e at each scattering position were not significant. With this assumption, a simplified attenuation coefficient can be approximately calculated by averaging the attenuation coefficients over all the possible scattering positions along the TCA:

$$\overline{Att} = \frac{\sum_i^M e^{-(\int_A^i \mu dl+\int_i^B \mu' dl)}}{M} \ldots\ldots\ldots\ldots\ldots\ldots..(5.4)$$

where M is the total number of pixels along the TCA for a scattered coincidence in the image matrix. This simplification will be evaluated and compared with that in Equation (5.3).

When the scattered photon energy approaches 511 keV, the attenuation correction calculated by this method approaches that for true coincidences calculated using the conventional approach.

Thus, the data model in Equation (5.1) was defined using the calculated attenuation coefficient:

$$\langle P_{ab}(\theta)\rangle = \overline{Att} \cdot \frac{d\sigma_C^{KN}}{d\Omega} \cdot \tau \int_{TCA} \epsilon_{AS} \epsilon_{BS}^{'} \left(\frac{\sigma_{AS}\sigma_{SB}}{4\pi R_{AS}^2 R_{SB}^2}\right) \cdot \rho_e(S) \cdot I_s dV_s \ldots\ldots\ldots\ldots\ldots\ldots (5.5)$$

Incorporating this attenuation coefficient into the GS-MLEM reconstruction algorithm in list-mode [43, 44], we get:

$$\vec{f}_i^{n+1} = f_i^n \frac{1}{\sum_{j'=1}^{N} a_{j',i}} \sum_{j=1}^{N} a_{j,i} \frac{1}{\sum_{i'=1}^{p} a_{j,i'} f_{i'}^n * \overline{Att}} \qquad i = 1, \ldots, p \ldots\ldots\ldots\ldots (5.6)$$

where p is the total number of pixels in the image, N is the total number of detected coincidences and $a_{j,i}$ is the element of the system matrix representing the probability detected in the j^{th} coincidence (whether scattered or not), were emitted from Pixel i.

The main difference between this Generalized Scatter (GS) based ML-EM algorithm (GS-MLEM) and the conventional ML-EM algorithm (LOR-MLEM) is that the projection/back-projection process is applied over the area confined by the TCA based on photon energy and detector positions instead of along the LOR. When including the patient/phantom outline as a constraint into the reconstruction algorithm, the summation is further confined to the area CDE as shown in Figure 4.1.

5.2.2 Evaluations based on GATE simulations

To evaluate the proposed method, a clinical PET scanner was simulated by GATE [67]. The PET scanner is a 24 ring system with 35 detector block per ring; each block is a 12×24 LSO crystal array with dimensions of 6.3×6.3×30 mm^3. The detector covers a total 70 cm transaxial FOV and 15.7 cm axial FOV. The detector efficiency was set to be homogeneous for all crystals, photon energy, and different incident photon directions.

The detectors have been shielded by lead slab, and only a slit with width of 20 mm was left for 2D acquisition. The system operates with an ideal energy resolution (0.1% FWHM at 511 keV). The energy window was set to 170-512 keV in order to detect all the true and single scatter coincidences. The spatial position and energy information were recorded for each measured coincident events. The total activity was kept below 3.7 MBq to reduce the number of randoms [81].

Two phantoms have been simulated in this work. The spatial resolution of the attenuation corrected images was obtained by simulating a 2 mm in diameter line source located at the center of a uniform 20 cm diameter cylindrical water phantom. The reconstructed images of a line source known as the PSF represent the different imaging system responses to the true and scattered events. The FWHM of the PSF of the line source was measured as a method of evaluating the spatial resolution.

The second simulated phantom was the National Electrical Manufacturers Association (NEMA) NU 2-2012 phantom [82], which was used to evaluate the accuracy of the attenuation correction and quantitatively analyze the image quality. This phantom contains four hot spheres (inner diameters 1.0, 1.3, 1.7 and 2.2 cm respectively) and two cold spheres (inner diameters 2.8 and 3.7 cm respectively) in a warm background. The ratio of the activities in the hot sphere to the background was set to 4:1. The attenuation correction was measured by placing a 5 cm diameter insert with an attenuation coefficient approximately equal to the average value in the lung (density 0.30 g/mL) at the center of the phantom.

The reconstructed image qualities were evaluated using the NEMA NU 2-2012 Standard [82]. ROIs with diameters equal to the physical inner diameters of the spheres were drawn on the spheres and throughout the background to evaluate the image quality. In addition, the accuracy of the attenuation correction was assessed by drawing an ROI in the region of the lung insert. The RSD as a measure of the background variability was calculated from the standard deviation of the mean relative to the mean in the background ROI values for each sphere size. The hot contrast recovery coefficient (CRC_{hot}) is calculated as:

$$CRC_{hot} = \frac{\frac{C_{hot}}{C_{bkgd}}-1}{\frac{a_{hot}}{a_{bkgd}}-1} \ldots\ldots\ldots\ldots\ldots\ldots(5.7)$$

where C_{hot} and C_{bkgd} are the average counts in the hot sphere ROI and the average of the counts in all background ROIs, respectively. a_{hot}/a_{bkgd} is the ratio of the activities in the hot sphere and background. The cold sphere CRC (CRC_{cold}) is calculated as:

$$CRC_{cold} = 1 - \frac{C_{cold}}{C_{bkgd}} \ldots\ldots\ldots\ldots\ldots..(5.8)$$

where C_{cold} is the average of the counts measured in the cold sphere ROI. The residual error (ΔC_{lung}) in the lung insert is calculated as:

$$\Delta C_{lung} = \frac{C_{lung}}{C_{bkgd}} \times 100\% ....(5.9)$$

where C_{lung} is the average of the counts in the lung insert ROI.

As comparisons, the same data were also reconstructed by using the conventional ML-EM (LOR-MLEM) method, which is developed based on the single scatter simulation approach. Firstly, the spatial distribution of single scatter events will be estimated by

Monte Carlo method. Then the estimated scatter is scaled globally to ensure a good fit between the estimated scatter and the measured projections. Lastly the true coincidences can be obtained by subtracting the scatter event events from the prompt coincidences and reconstructed in MLEM algorithm interactively.

5.3 Results

5.3.1 Spatial resolution comparison between true and scattering reconstruction

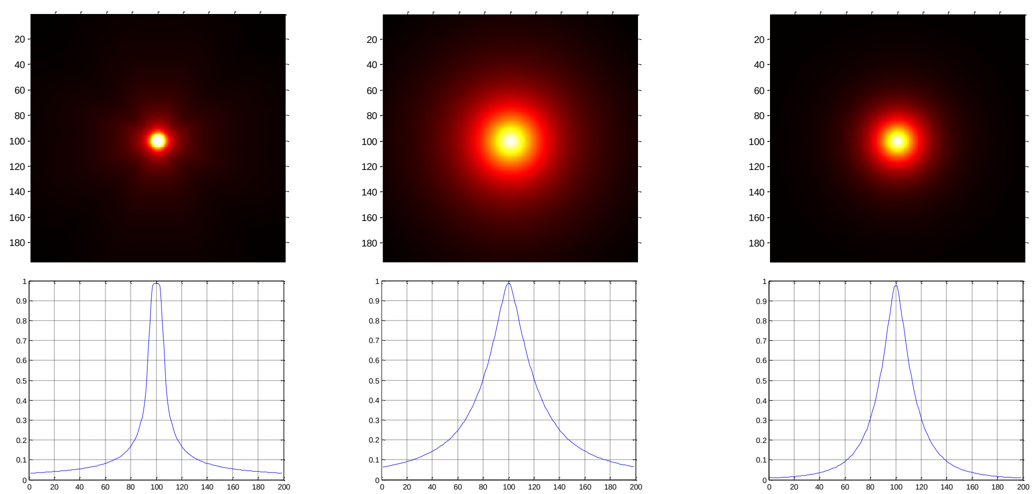

(a) (b) (c)

Figure 5.1 The PSFs generated by back-projecting a line source in a 20 cm diameter uniform water phantom using (a) true coincidences, (b) scattered coincidences without patient outline constraint, and (c) scattered coincidences with patient outline constraint. The corresponding profiles passing through the center of the above images are also shown under each image. The pixel size of the reconstructed images is 0.2 mm.

Figure 5.1 shows the PSFs of a line source and the corresponding profiles generated by back-projecting true and scattered events under the ideal energy resolution scenario respectively, which represents the different responses of the imaging system to true and scattered coincidences. The FWHM of the PSF for the scattered photons without the patient outline constraint in Figure 5.1(b) is 8 mm at 0.1% energy resolution while the FWHM for the trues in Figure 5.1(a) is 4 mm at the same energy resolution. When using the patient outline as a constraint, the FWHM of the PSF for the scattered photons in Figure 5.1(c) has reduced to 6 mm but still 50% larger than that from true events.

5.3.2 Image quality of NEMA phantom

5.3.2.1 Image quality evaluation using scattered only

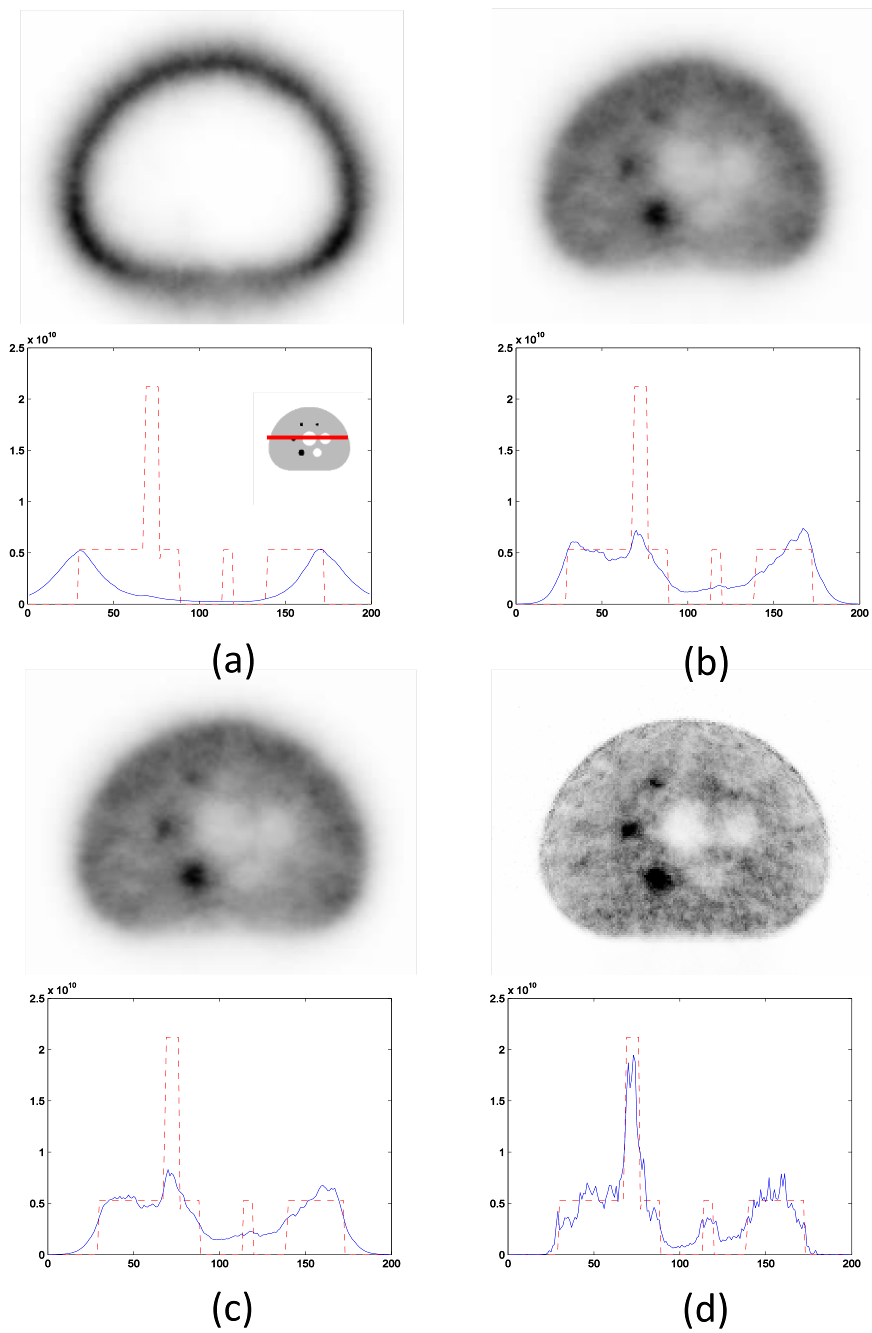

Figure 5.2 (a) image reconstructed from only scattered coincidences without applying any attenuation correction; (b) image reconstructed from only scattered coincidences with the attenuation correction

calculated using the full physics model (Equation (5.3)); (c) image reconstructed from only scattered coincidences with the attenuation correction calculated using the simplified model (Equation (5.4)); (d) image reconstructed from scattered coincidences with the attenuation correction calculated using the full physics model plus phantom outline constraint employed. The profiles (blue line) passing along the center of the above images and the actual activity distribution (red line) in the horizontal direction are also shown under the corresponding images.

Figure 5.2 shows the transaxial images of the NEMA phantom reconstructed using only scattered coincidences with and without attenuation correction applied. Figure 5.2(a) illustrates the reconstruction without any attenuation correction and shows regions in the center of the phantom that are void of tracer while high activities are observed around the edges of the phantom. The image shown in Figure 5.2(b) is reconstructed from scattered coincidences only and with attenuation coefficients calculated using the full physics model (Equation (5.3)) while Figure 5.2(c) shows a similar image except that the attenuation coefficients are calculated using the simplified model (Equation (5.4)). Even though the contrast and noise properties of the images shown in Figure 5.2(b) and Figure 5.2(c) are not optimal, they still adequately represent the actual activity distribution. Three of four hot spheres (except the 1-cm hot sphere) and all three cold spheres were both observable in Figure 5.2(b) and Figure 5.2(c). The high intensity near the outline seen in Figure 5.2(a) has disappeared with attenuation correction in Figure 5.3(b) and Figure 5.2(c). The images, as well as the profiles, show little difference between Figure 5.2(b) and Figure 5.2(c). However, the attenuation coefficients calculated using the full physics model involved more parameters in the calculation process and result in a 2-3 times larger computational load compared with the simplified model. Figure 5.2 (d) illustrates that when the attenuation and the outline constraint are taken into account all four hot spheres, including the 1-cm hot sphere, were observable. Similar results are obtained irrespective of which attenuation correction approach was used. The corresponding profile matches better the actual activity distribution compared with these in Figure 5.2(b) and Figure 5.2(c).

To compare the similarity between the reconstructed images with the actual activity distribution, 2D correlation coefficients between the reconstructed images and the ground-truth activity distribution were calculated and are shown in Figure 5.3. A similar trend to that illustrated in Figure 5.2 can be seen. The image without attenuation poorly correlated with the standard activity distribution with a correlation coefficient of less than 0.3. The correlation improves to better than 0.81 with the inclusion of attenuation correction while adding the outline constraint improved the correlation by another 6%. The correlation coefficient of the image shown in Figure 5.2(d) is 0.87, which is comparable to the value of 0.92 obtained with the image reconstructed only using true coincidences.

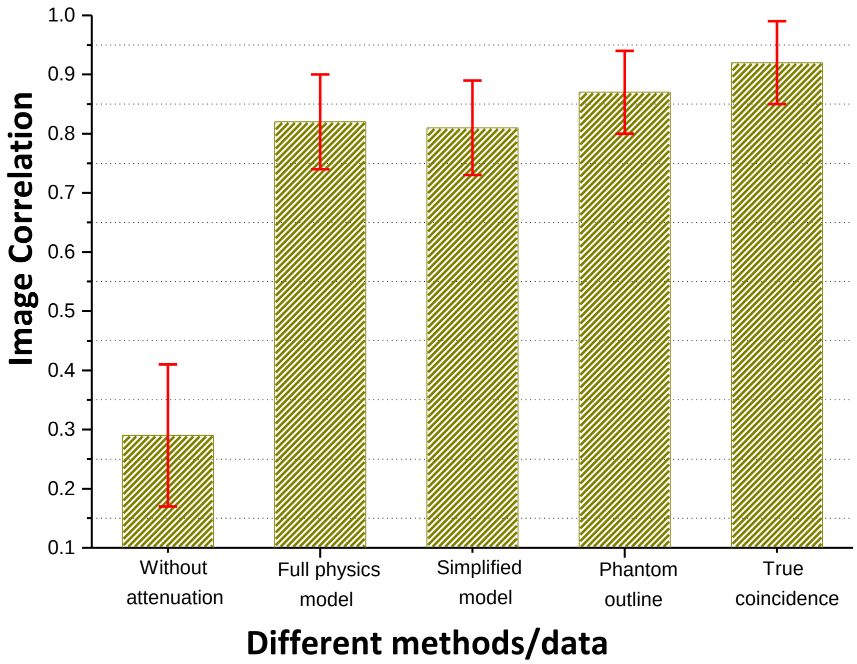

Figure 5.3 The correlation between the standard activity distribution and images reconstructed using only scattered coincidences without/with attenuation correction applied as well as the phantom outline constraint. The correction for the images reconstructed from true coincidences is also calculated as a comparison.

One drawback of the images reconstructed only from scattered coincidences is that a background has been added to the activity, which may degrade image contrast. However, in practice, both true and scattered coincidences are used simultaneously, and the performance of the algorithm will be evaluated in the following section.

5.3.2.2 Evaluation of image quality reconstructed by the GS method with attenuation correction

Figure 5.4(a) shows the image reconstructed from the simulated data with a scatter fraction of 50% by using the GS-MLEM algorithm. The attenuation coefficients were calculated using the full physics model and the patient outline constraint was also applied in this figure. When incorporating both true and scattered events into the reconstruction, the base added to the activity has removed compared with that only using scattered events in Figure 5.2. Figure 5.4(b) shows the image reconstructed only from the same number of the true coincidences used in Figure 5.4(a), representing the optimal image that would be obtained by scatter correction based methods. Figure 5.4(c) shows the image reconstructed using the same measured data as in Figure 5.4 (a) and using the conventional LOR based (LOR-MLEM) algorithm. The corresponding profiles passing through the center of the reconstructed image (blue line) and the ground-truth activity distribution (red line) for each image are also shown in the second row. Compared with Figure 5.4(b) and (c), all the four hot and the two cold spheres were observable in Figure 5.4(a). While the PSF of the scattered events is broader than that from true events as shown in Figure 5.1, incorporating scattered events into the reconstruction did not compromise the image spatial resolution. In contrast, the noise has been reduced when including the scattered events into the reconstruction.

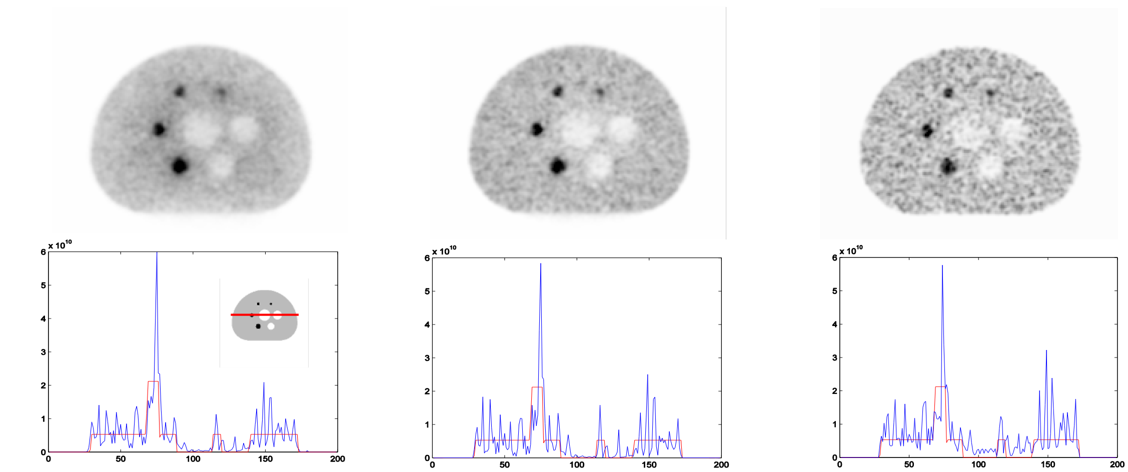

(a) (b) (c)

Figure 5.4 (a) An image reconstructed from the simulated data with a 50% scatter fraction using the GS-MLEM algorithm. The attenuation coefficient was calculated using the full physics model and the patient outline constraint was also applied; (b) image reconstructed from only true coincidences, which represents the optimal image with the scatter correction based method; (c) image reconstructed from the same data as in (a) using a conventional scatter correction based method. The profiles (blue line) along the center of the above images and the ground-truth activity distribution (red line) in the horizontal direction are also shown under the corresponding images.

To evaluate the reconstructed image quality, the CRC and RSD (represented by the error bar for each data point), were calculated for the six different spheres in Figure 5.5. When including both true and scattered coincidences into the reconstruction (Figure 5.4(a)), the CRC for hot spheres with diameters of 1-2.2 cm increased by 3-11% compared with that using only true events (Figure 5.4(b)) and by 9-24% against conventional scatter correction based methods (Figure 5.4(c)). For the two cold spheres, the CRC for Figure 5.4(a) increased by 5% and 11% with respect to Figure 5.4(b) and by 18% and 23% compared with Figure 5.4(c) respectively. At the same time, the RSD has decreased by 4% and 3.5% for the hot and cold spheres respectively compared with Figure 5.4(b). Compared with Figure 5.4(c), the RSD has decreased by 6% and 5% for the hot and cold spheres respectively. The residual errors in the lung insert (largest cold sphere in the center of the phantom) in the Figure 5.4(a) have decreased by 17% and 21% compared with Figure 5.4(b) and Figure 5.4(c), respectively.

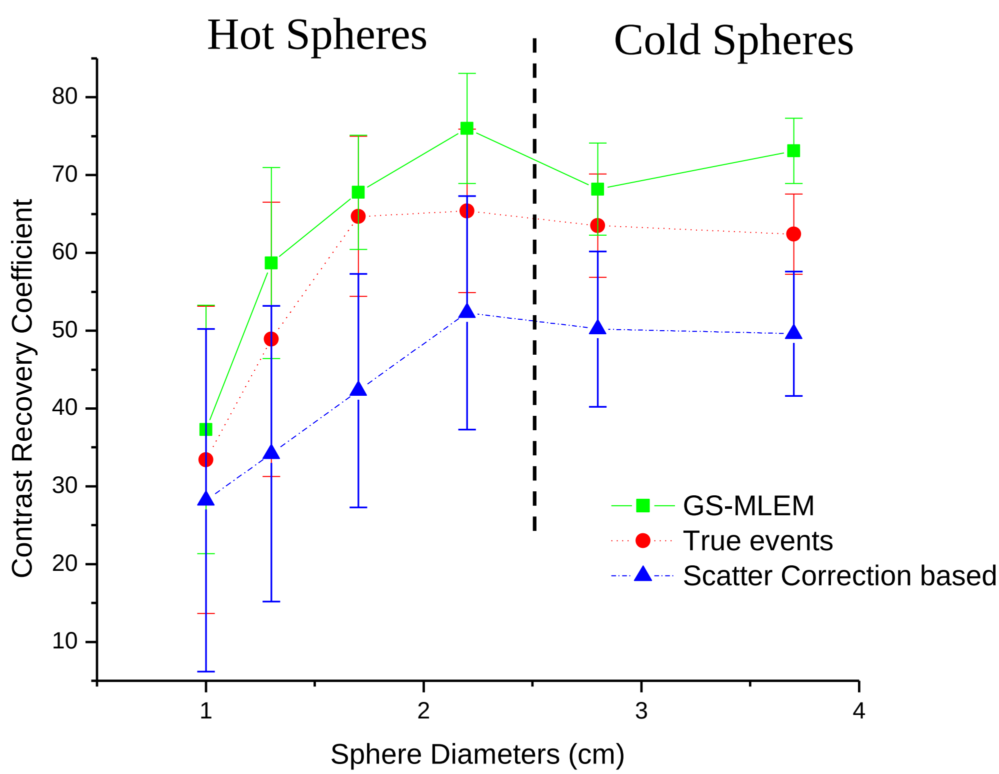

Figure 5.5 The contrast recovery coefficients of the spheres with different diameters for images reconstructed from both true and scattered coincidences using the GS algorithm (solid line+square symbol), the same true and scattered events reconstructed using the conventional scatter correction based method (dash-dot line+triangle symbol), and only from true coincidences using the conventional scatter correction based method (dot line+circle symbol). The relative standard deviation represented by the error bar at each data point is also shown in this figure.

5.4 Discussion

The benefits of including scattered coincidences into PET imaging reconstruction are twofold. Firstly, it eliminates the need for the scatter correction procedure carried out in the conventional PET reconstruction methods; Secondly, it improves the contrast and noise properties of the reconstructed images, as well as the system sensitivity. However to successfully implement the proposed method on clinical PET scanners, some issues still need to be addressed. Firstly, the TCA used to describe the scattered locus is closely related to the scattered photon energy. As such, the performance of this method is limited by the energy resolution of the PET detectors. This can be addressed by developing novel PET detectors with better energy resolution. Alternatively, by assigning the true and scattered probabilities to the measured event, the generalized scattered reconstruction algorithm can be made less sensitive to the energy resolution of the detector. This work will be described in more detail in Chapter 7. Secondly, the inter-crystal, inter-block, and multiple scattered events cannot be distinguished from those scattered within the object based only on the scattered photon energy. In this study, the septa added to simulate a 2D scanner will increase the inter-crystal and inter-block scattered events. A method to address the inter-crystal and inter-block scattered events by summing the photon energies in adjacent detectors within a defined time stamp has been proposed [83]. The lower energy threshold of 170 keV can also increase the detection of multiple scattered events. The area within the TCA increases as the scattered photon energy decreases and thus the contribution from these events are small. The trade-off between the available scattered counts and the lower energy threshold has been investigated in Chapter 3, and an energy threshold of ~350 keV can give a good compromise [73]. Thus in practice a higher energy threshold will typically be used. As the goal of this chapter was to develop an effective photon attenuation correction method for all single scattered events, the lower energy window of 170 keV was selected.

As illustrated in Figure 5.1, the point spread function extracted from only scattered events is broader than that calculated from trues. This result is expected as the area of the TCA used to confine the source position for scattered events is larger than that LOR for true events. The detail in the images reconstructed from only scattered photons as shown in Figure 5.2(b) and 5.2(c) demonstrates greater blurring than when reconstructed from only trues. The blurring can be reduced by introducing additional constraints to further refine the possible annihilation area. As shown in Figure 5.2(d), the image quality has been improved when the phantom outline is used to confine the annihilation positions. This is consistent with the narrower PSF in Figure 5.1(c). In practice, both trues and scattered photons are used in the reconstruction and the broader PSF due to the scattered photons has little impact on the resolution as shown in Figure 5.4(a). This is due to the ratio used to update the image in the next iteration being inversely proportional to the area confined by the TCA. For the TCA with large scattering angle, the contribution to the imaging reconstruction has been reduced. On the other hand, the inclusion of the scattered photons, as shown in Figure 5.5, improves the contrast by 3-11% compared with a reconstruction using only true events and by 9-24% against conventional methods. In addition, the noise has been decreased by 4% and 6% respectively.

As demonstrated in Figure 5.2(a), severe distortions of activity distribution are observed without effective attenuation correction of the scattered photons. These artifacts can be removed by using the attenuation coefficients calculated with either the full physics model or the simplified model. The correlation coefficients calculated between the reference image and Figure 5.2(b) and Figure 5.2(c) differ by less than 3%. However, the attenuation coefficient calculated using the full physics model in Figure 5.2(b) needs more apriori information and takes 2-3 times longer to compute than the simplified model. Thus calculating the attenuation coefficients for scattered coincidences by averaging the attenuation coefficient over the scattering locus is efficient and sufficiently accurate for reconstruction using scattered photons.

5.5 Conclusion

Two methods to calculate the attenuation coefficients for scattered coincidences have been proposed. While both methods are suitably accurate, the simplified model is more efficient. The artifacts due to scattered photon attenuation have been removed, and the image contrast and noise properties have been improved by incorporating scattered coincidences into the PET imaging reconstruction.

Chapter 6: A Geometrical Model to describe Annihilation Positions associated with Scattered Coincidences in PET: A Simulation-based study

6.1 Introduction

In the previous chapters, we have developed the GS reconstruction algorithm in PET to extract the activity distribution from both true and scattered coincidences in a consistent manner [71, 73]. The previous work has shown that the activity distribution can be extracted from only scattered coincidences, and incorporating scattered coincidences into PET reconstruction can improve both the image quality attributes of contrast and noise [71, 73].

The probability of the annihilation position within TCA in our previous work however was not modeled in the GS reconstruction algorithm, and only a uniform distribution within the TCA is assumed. In reality, this probability is constrained by the source distribution and the scanned object size. If this probability could be accurately modeled and built into the reconstruction algorithm, we assume that the image can converge faster to the activity distribution and the corresponding reconstructed imaging quality could be further improved. Kazantsev et al. [84] have derived a mathematical model of single scatter in PET for a detector system possessing excellent energy resolution in both 2D and 3D cases. However, this model depends on the distance between the two photon detected positions, which is generally different for each scattered coincidence. Besides, only a single source was exploited in this work. Different from the work of Kazantsev et al. , the goal of this chapter is to propose a geometrical model in a normalized coordinate to characterize the distribution of the annihilation positions associated with scattered coincidences, and investigate the dependency of this distribution on the source distribution and scanned object size based on the Monte-Carlo simulations.

6.2 Methods and Materials

6.2.1 The Geometrical model to describe the annihilation positions associated with scattered coincidences

In this work, the term of scattered coincidences refers to the event in which only one of the two annihilation photons undergoes a single Compton interaction in the object. This assumption has been validated by a number of Monte Carlo simulations, in which the single scattered events account for more than 80% of the measured scattered events [1, 33]. With the knowledge of the scattered photon energy E', the scattering angle θ for a photon with the primary energy of 511 keV undergoing a Compton interaction can be calculated by using the Compton equation:

$$cos\theta = 2 - \frac{511}{E'} \quad \ldots\ldots\ldots\ldots\ldots(6.1)$$

With this scattering angle, the TCA can be identified as illustrated in Figure 6.1(a) by connecting the two coincident photons measured positions with two arcs. The scattering angle, and the distance between the two photon-measured positions are generally different for different scattered coincidences. In order to describe the annihilation positions for all the scattered coincidences within the same geometrical model, we have normalized the distance *AB* between the detector pair (A, B) and the perpendicular distance *CO* from the TCA to the center of AB as unity. Thus, the annihilation point *S* for a scattered event can be expressed by using the ratio of *AD* relative to *AB* as the abscissa, and the ratio of *SD* relative to *CO* as the ordinate in this normalized coordinate, as illustrated in the Figure 6.1(b).

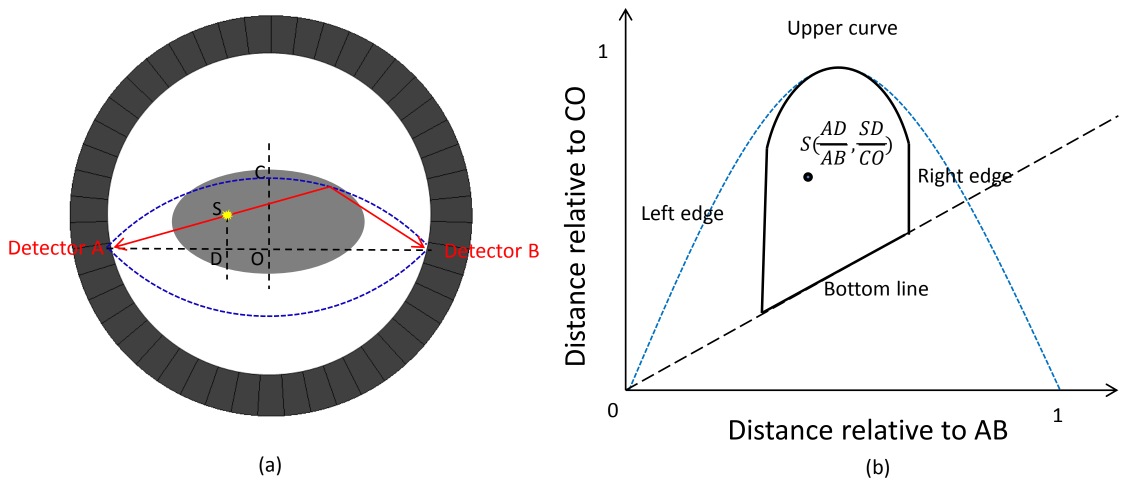

Figure 6.1 Diagram of a scattered coincidence in the object. Two anti-parallel 511 keV photons are generated at S, with the unscattered photon observed at A and the scattered photon observed at B. Two circular arcs (TCA), shown as blue dotted curves, which describe all the possible scattered positions and encompass the annihilation position, can be identified. O is the center of AB and CO is perpendicular to AB and intersects one-half TCA at C. (b) The annihilation position S in the normalized coordinates can be obtained by normalizing AD relative to the distance AB as the abscissa and the ratio of SD relative to CO as the ordinate. The geometrical model to describe the distribution of the annihilation positions (black solid line) and normalized TCA (blue dotted line) are also illustrated in this figure.

Limited by the size of the scanned object and the radiopharmaceutical distribution, the probability of the annihilation position is not uniform within the TCA. We have proposed a geometrical model (black solid line) as shown in the Figure 6.1(b) to describe the distribution of the annihilation positions. The upper curve of this geometrical model is confined by the normalized TCA (blue dotted line), which describes all the possible scattered positions and are the outer edge of the annihilation positions in this new coordinate. The locus (x', y') of this normalized TCA is given by:

$$y' = \frac{1}{1-\cos\theta}\left(\sqrt{1-4[(x'-0.5)\cdot\sin\theta]^2}-\cos\theta\right) \quad \text{.............(6.2)}$$

The derivation of this equation is given in Appendix B. Initially the upper curve of this geometrical model coincides with the normalized TCA. As the upper curve continues extending downward, it gradually deviates from the normalized TCA and the distance between the left and right edges continues to increase until a maximum value is achieved. The deviation is due to the annihilation positions within the TCA being limited by the size of the scanned object and the distribution of the radioactive source. The maximum distance between the left and right edges can be characterized by a linear function of the largest distance from the source to the center of the FOV. The bottom edge of this geometrical model can be described by a straight line passing through the origin of the normalized coordinate, with a slope which depends on the size of the scanned object. For a point source located in the center of the FOV, the straight line will pass through point (0.5, 1) with a maximum slope of two. As the phantom size increases, the slope of the lower line decreases to zero as the radius of the scanned object (if a cylindrical shape is assumed) approaches the radius of the PET scanner. Thus, mathematically the slopes S of the bottom line can be characterized by a linear relationship with the ratio of the radius r of the scanned object (if cylindrical phantoms assumed) relative to the radius R of the PET scanner:

$$\boldsymbol{s = -2 \cdot \frac{r}{R} + 2} \ \ldots\ldots\ldots\ldots\ldots \ (6.3)$$

The probability density of annihilation positions within the geometrical model depends on both the radioactive source distribution and the size of the scanned object. This dependency on the radioactive source and scanned objects was explored using MC simulations.

6.2.2 GATE simulation

To investigate the distribution of annihilation positions within the normalized TCA as a function of the radioactive source and the scanned object size, a PET scanner with ideal energy resolution (0.1% FWHM at 511 keV) was simulated using GATE [66, 68]. The system consists of 24 detector rings of 35 detector modules placed on a ring with radius 44.3 cm, each module is composed of a 12×24 LSO crystal array of 6.3×6.3×30 mm^3. To acquire the measured data in 2D, the detectors have been shielded by lead slab, and only a slit with width of 20 mm was left. A 6 ns coincidence window and a 3.2 ns time resolution were also modeled. All simulations were made for an energy window of 170-512 keV to detect all the true and single scatter coincidences. The detected positions, annihilation position, and photon energy will be recorded for each coincidence in list-mode in the GATE simulations.

Four sets of simulations have been set up to evaluate the dependency of the proposed geometrical model on the phantom sizes and the source distributions. The phantoms are always placed at the center of the FOV in these simulations.

i) A line source with radius of 2 mm located at the center of the cylindrical water phantoms with radii 10 cm, 20 cm, 30 cm, 40 cm respectively;

ii) A 25 cm radius cylindrical water phantom with a line source with radius of 2 mm located at 5 cm, 10 cm, 15 cm, 20 cm to the center of the phantom individually;

iii) Two 25 cm radius cylindrical water phantoms, one with a centered ring source (with inner and outer radii of 9.8 cm and 10 cm), and one with a 10 cm radius cylindrical source respectively, were simulated. These two simulations will be compared with that of the 25 cm radius cylindrical water phantom with a line source with radius of 2 mm located at 10 cm to the center of FOV as simulated in (ii). This set of simulations is used to validate that the maximum distance between the left and right edges of the proposed geometrical model is only dependent on the largest distance from the radioactive source to the center of the FOV.

iv) Cylindrical water phantoms with radii 10 cm, 20 cm, 30 cm and 40 cm, and with uniform source distribution.

Only the events undergoing a single Compton scattering within the phantom were selected from the coincident files. Then the TCA for each scattered coincidence was identified, and the annihilation position relative to the TCA in the normalized coordinate was calculated and plotted in a 2D histogram. Since the number of the scattered coincidences generated in each simulation is different, the analysis of the intensity of the distributions is limited within each figure and is not comparable between different simulations.

To quantitatively evaluate the geometrical model, we measured a series of points along the upper edge of the distribution in (iv) set simulations, and the positions were compared with the calculated TCA in the normalized coordinate system. We also evaluated 1) the slopes of the straight lines along the lower edges of the distribution as a function of phantom size; 2) and the relationship between the width of the distribution in the normalized coordinate and the largest distance from the source to the center of the FOV.

To validate that the proposed geometrical model can be used to predict the distribution of the annihilation position and can also improve the reconstructed image quality, the NEMA NU 2-2012 phantom [82] was simulated. The maximum width of the cross section of NEMA phantom is 30 cm, and the height is 23 cm. Since the distribution relies on the largest distance from the source to the center of the FOV in this geometrical model, we selected the half-maximum width (15 cm) to calculate the outline of distribution to test the accuracy of the proposed model. To evaluate the reconstructed image quality, a total of one million scattered coincidences were generated by GATE using a NEMA phantom and reconstructed with and without introducing the distribution of the annihilation positions as a constraint into the GS-MLEM algorithm.

6.3 Results

Figure 6.2 shows the 2D histogram of the annihilation positions associated with scattered coincidences in the normalized coordinate for the first set of different radii cylindrical water phantoms with a line source located in the center. The distributions of annihilation positions are narrow for the line source located in the center of phantoms. The widths between the left and the right edge of the distributions are almost the same for these four simulations, which are independent of the size of the cylindrical phantom. The radius of the phantom only determines the vertical length of the distribution, which becomes longer as the radius of the phantom increases. This vertical length can be characterized by the slope of a straight line passing through the origin and the bottom of the distribution, which will be obvious for a distributed source. The high-intensity area tends to concentrate at the lower end of these distributions and becomes increasingly needle-like as the radius of the phantoms increases.

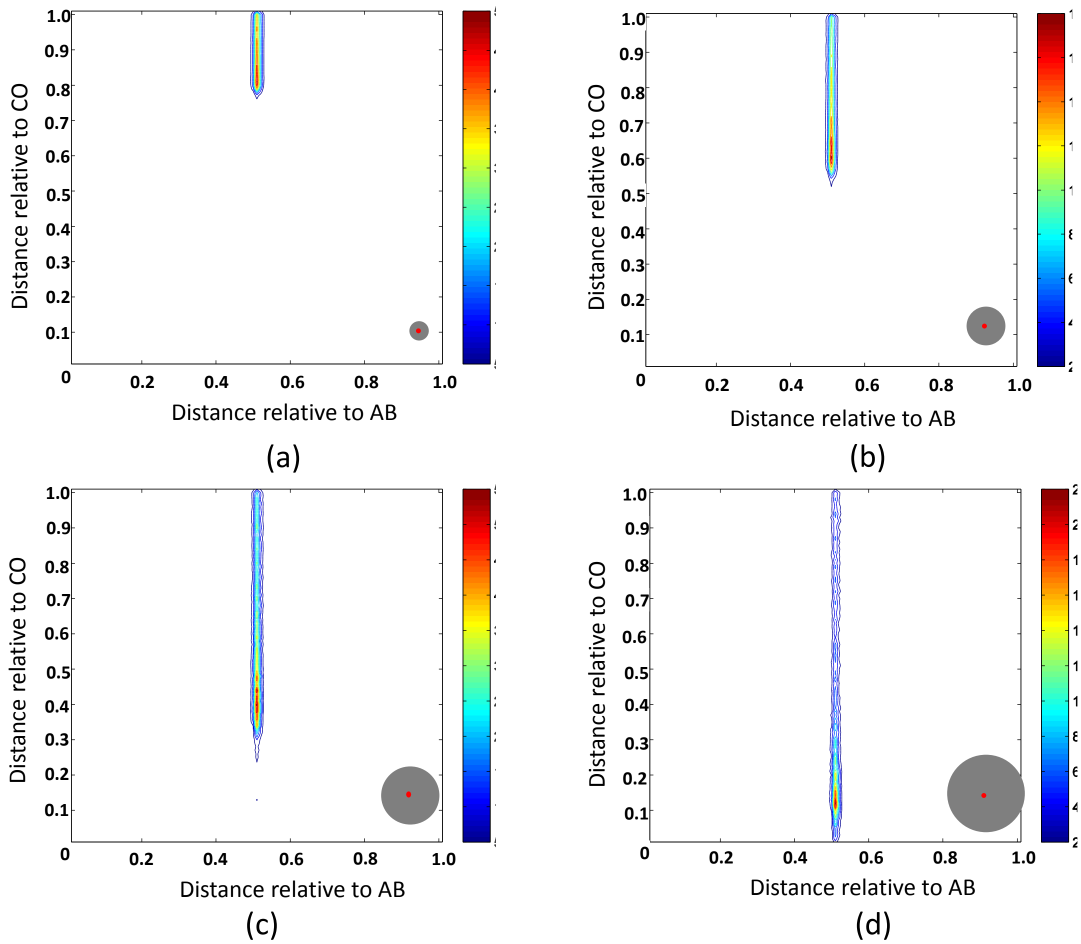

Figure 6.2 The 2D histogram of the annihilation positions associated with scattered coincidences in the normalized coordinate for a line source in the center of the cylindrical water phantoms with radius (a) 10 cm, (b) 20 cm, (c) 30 cm and (d) 40 cm respectively.

Figure 6.3 shows the 2D histogram of annihilation positions associated with scattered coincidences in the normalized coordinate for the same cylindrical phantom with a radius of 25 cm but with a line source located at 5 cm (Figure 6.3(a)), 10 cm (Figure 6.3(b)), 15 cm (Figure 6.3 (c)), and 20 cm (Figure 6.3 (d)) from the center of the phantom. As indicated in this figure, the distance between the left and right edges of the distributions are dependent on the largest distance from the source to the center of FOV. When the sources are located further away to the center of FOV, the upper edges of the distribution extend further downward, and the distribution of annihilation positions becomes wider. The slopes of these bottom lines are the same within a reasonable uncertainty (3%) for this set of simulations, which indicates that the slopes of these lines are only dependent on the phantom size for a specific PET scanner geometry and are independent of the source distributions. The intensities of the distribution of annihilation positions in the normalized coordinate are not uniformly distributed; high intensities are concentrated at the left and right bottom edges except in Figure 6.3 (d) in which high intensity is also seen to concentrate at the upper center of the distribution.

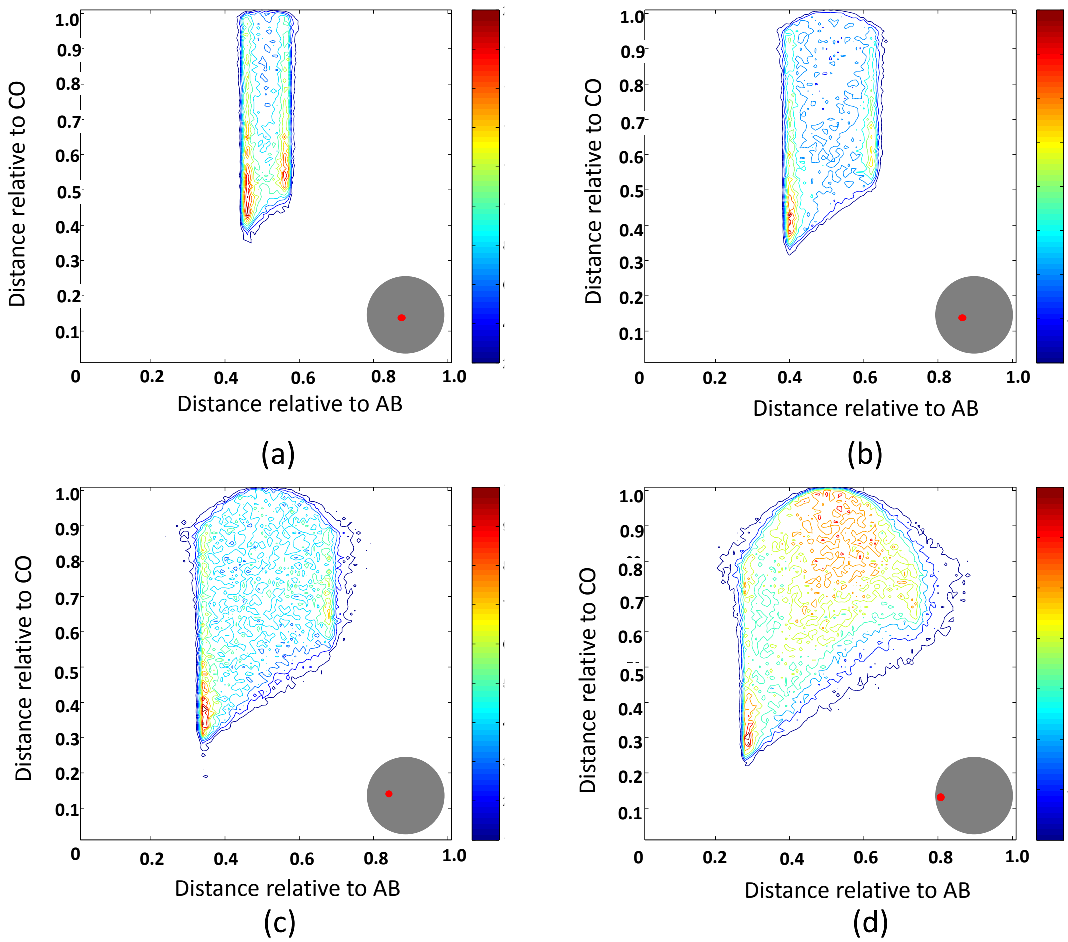

Figure 6.3 The 2D histogram of the annihilation positions associated with scattered coincidences in the normalized coordinate for a 25 cm radius cylindrical phantom with a line sources located at (a) 5 cm, (b) 10 cm, (c) 15 cm, and (d) 20 cm from the center of the FOV.

These results have shown that the width of the distribution of the annihilation positions in the normalized coordinate is only dependent on the largest distance from the source to the center of the FOV. To further validate this conclusion, the 2D histograms for a 25 cm radius cylindrical water phantom with a ring source with an inner radius 9.8 cm and an outer radius of 10 cm are shown in the Figure 6.4 (b), and a cylindrical source with a radius of 10 cm shown in the Figure 6.4 (c), are generated. These two distributions were compared with the same cylindrical water phantom but with a line source located at 10 cm from the center of the FOV as shown in Figure 6.4(a) (same as Figure 6.3 (b)). As shown in Figure 6.4, the width of the distribution of the annihilation positions are the same for these three different source configurations, and only the intensities of these distributions are impacted by the source configurations. The slopes of the straight lines along the bottom edges in Figure 6.4 are not dependent on the different source configurations, which is only a function of the phantom size.

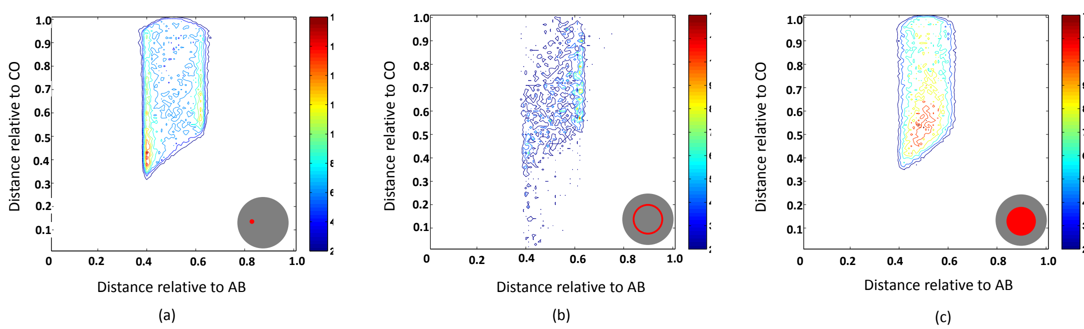

Figure 6.4 The 2D histogram of the annihilation positions associated with scattered coincidences in the normalized coordinate for a 25 cm radius cylindrical phantom with (a) a line sources located at 10 cm from the center of the FOV, (b) a ring source with inner radius 9.8 cm and outer radius 10 cm, and (c) a cylindrical source with radius 10 cm.

Figure 6.5 shows the 2D histogram of the annihilation positions in the normalized coordinate for the 10 cm (Figure 6.5(a)), 20 cm (Figure 6.5(b)), 30 cm (Figure 6.5(c)) and 40 cm (Figure 6.5(d)) radius cylindrical water phantoms with uniform source distribution. As the radius of the phantoms increases, the distribution of annihilation positions stretches to a larger area within the normalized TCA. The upper curve of this distribution also extends lower as the radius of phantoms increases. As indicated in the previous results, the slopes of the lines along the bottom edges are a function of the phantom size for a specific PET scanner geometry. When the radius of the phantom becomes larger, the slope of the straight line along the bottom edge becomes smaller. For a uniform source distribution within most of the phantoms, the high-intensity areas are concentrated in the upper center of the distribution in the normalized coordinate system and decrease toward the left, right and lower edges. However, in the case of the 40 cm radius phantom (Figure 6.5(d)) the high-intensity area is concentrated in the lower left of the distribution with coordinates equal to (0.2, 0.1).

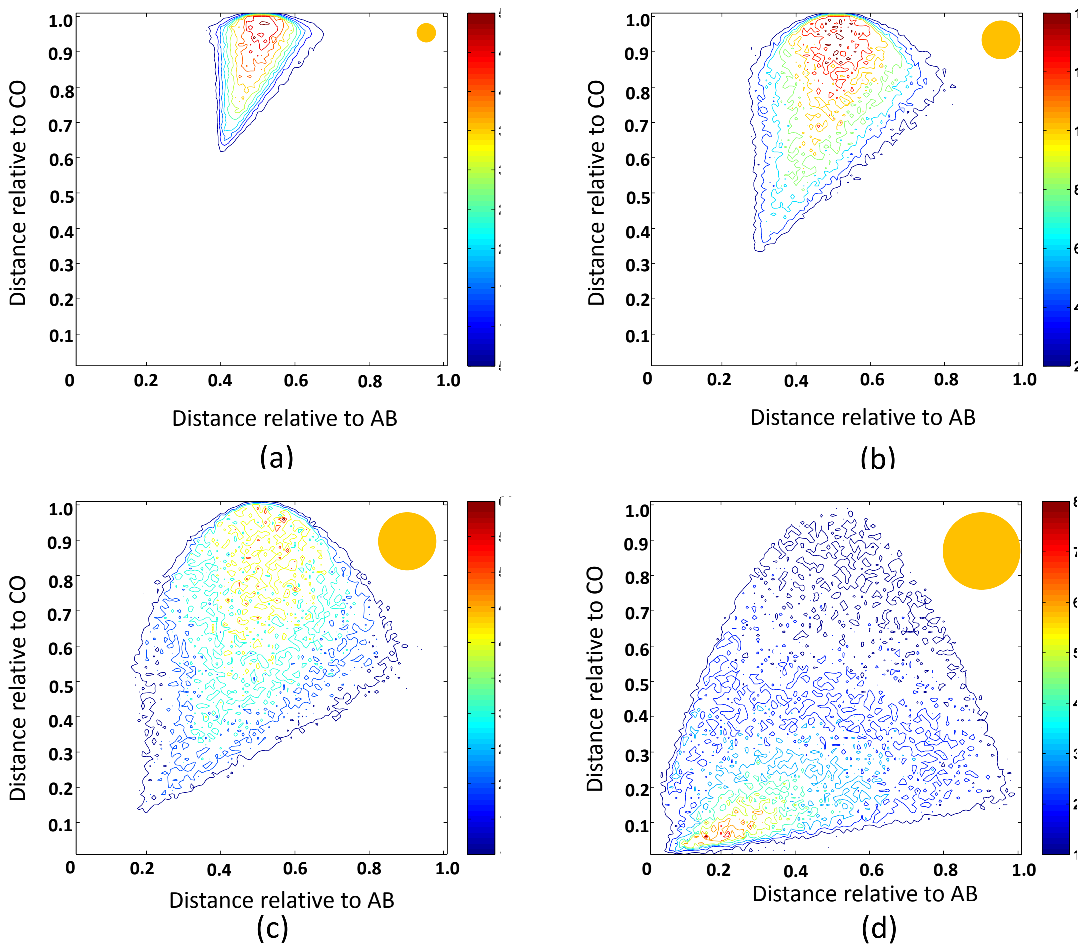

Figure 6.5 The 2D histogram of the annihilation positions in the normalized coordinate for (a) 10 cm, (b) 20 cm, (c) 30 cm and (d) 40 cm radius cylindrical water phantoms with uniform source distribution.

To validate the accuracy of the proposed geometrical model, we calculated the normalized TCA with scattering angles of 0.01$\boldsymbol{\pi}$ and 0.5$\boldsymbol{\pi}$ using Equation (6.1). These are plotted in Figure 6.6. The curves of the normalized TCA are a function of the scattering angle, which broadens as the scattering angle increases. The points along the upper curves of the distribution of the annihilation distributions in Figure 6.5 were measured and plotted in this figure. For the cylindrical phantom with a 10 cm radius, the edge of the upper curve of the distribution is more consistent with the normalized TCA with scattering angle of 0.5$\boldsymbol{\pi}$. As the radius of the cylindrical phantom increases, the top curve approaches the normalized TCA calculated with scattering angle of 0.01$\boldsymbol{\pi}$.

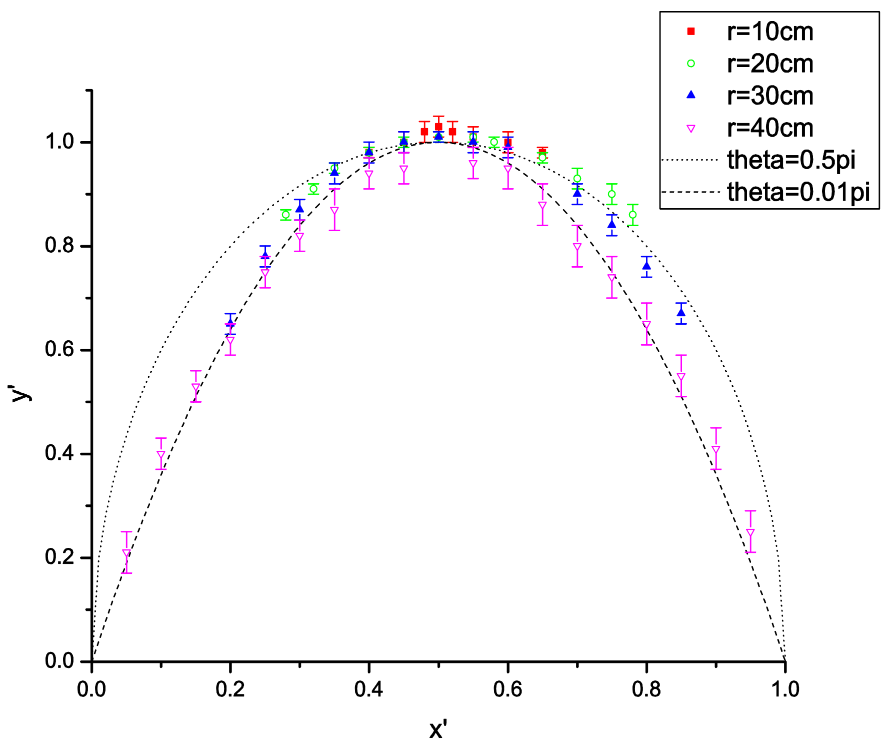

Figure 6.6 The curves of TCA with scattering angles of 0.01$\boldsymbol{\pi}$ (dash line) and 0.5$\boldsymbol{\pi}$ (dotted line) are calculated and plotted in the normalized coordinate. The points on the top curves of the distribution of the annihilation position in Figure 6.5 were sampled and plotted in this figure.

The slope of the bottom line of the annihilation distribution as a function of the phantom size was calculated and plotted in Figure 6.7. The phantom sizes have been normalized relative to the radius of the PET scanner. The relationship can be fitted with a straight line with a negative slope of -1.91 with an uncertainty 3.7%. The slope and intercept of the fitted line deviate from the predicted values by 4.5% and 3.4% respectively. The result shows that the slope of the straight line along the bottom of the distribution of annihilation positions in the normalized coordinate decreases linearly as the radius of the phantom increases.

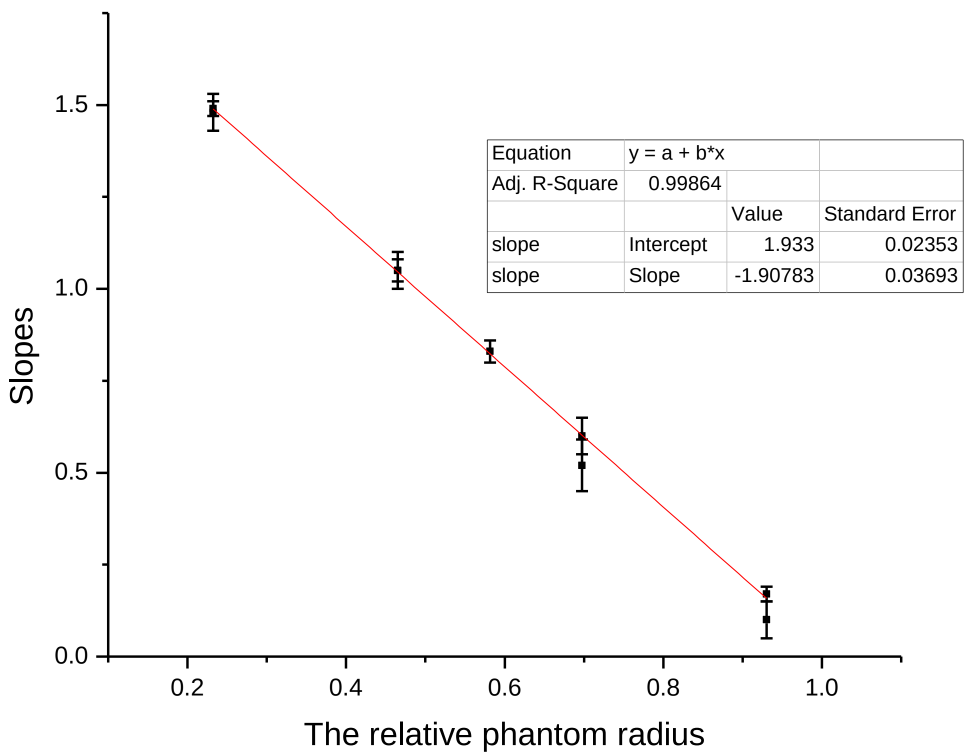

Figure 6.7 The slopes of the bottom lines of the annihilation distribution as a function of the phantom size. The phantom sizes have been normalized to the radius of the PET scanner in this plot.

The distance between the left and right edges of the annihilation positions distribution in the normalized coordinate were calculated and plotted as a function of the largest distance from the sources to the center of the FOV in Figure 6.8. The data is fit by a straight line. The result indicates that the relationship between the relative width of the distribution of the annihilation positions and the largest distance from the source to the center of FOV is strongly linear with R^2=0.99.

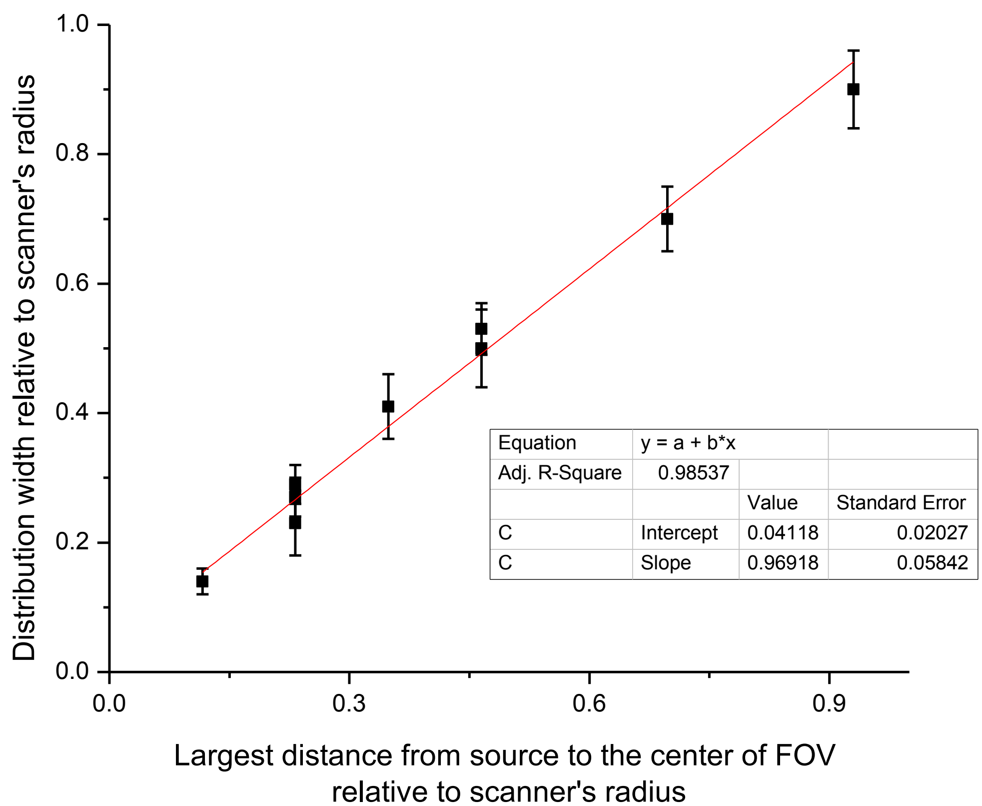

Figure 6.8 The relationship between the width of the distribution and the furthest distance from the radioactive source to the center of the FOV.

Figure 6.9 shows the 2D distribution of the annihilation positions associated with scattered coincidences for the NEMA NU2-2012 phantom in the normalized coordinate system. This distribution is similar to the cylindrical phantoms with a uniform source distribution. This is because the NEMA phantom has a distorted ellipse-like shape and the source is distributed within the phantom. The geometrical outline calculated using the proposed model is also plotted with a red dash-dot line in this figure. The predicted outline fits with the actual distribution of the annihilation positions except the aberration at the left bottom.

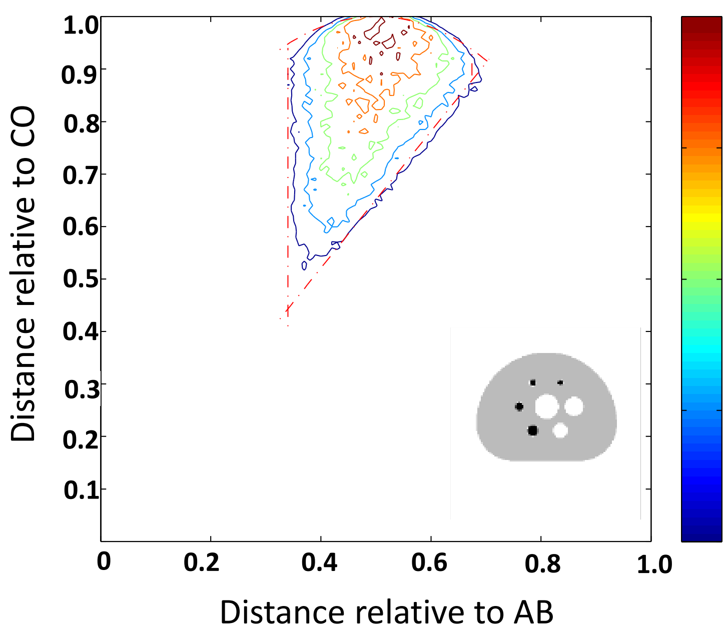

Figure 6.9 The 2D histogram of the annihilation positions associated with scattered coincidences for the NEMA phantom in the normalized coordinate. The outline calculated based on the proposed geometrical model is also plotted with red dash-dot line in this figure.

Figure 6.10 shows the images reconstructed from only scattered coincidences without and with the introduction of the annihilation position distribution model as a constraint in the GS-MLEM algorithm. Compared to the image without the annihilation distribution constraint, as shown in Figure 6.10(a), the contrast and noise properties of the image shown in Figure 6.10(b) have improved by 6% and 4% respectively.

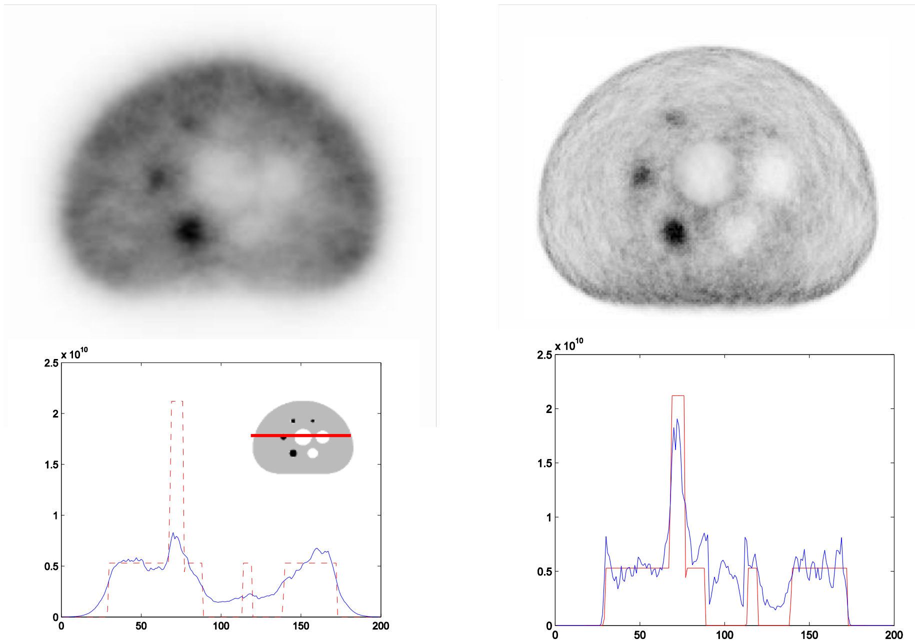

(a) (b)

Figure 6.10 (a) Image reconstructed from only scattered coincidences by using the GS-MLEM algorithm; (b) image reconstructed from the same scattered coincidences with introduction of the geometrical distribution into the GS-MLEM algorithm. The profiles (blue line) along the center of the above images and the phantom (red line) in the horizontal direction are also shown under the corresponding images.

6.4 Discussion

In this chapter, a geometrical model associated with scattered coincidences in PET has been proposed to describe the distribution of the annihilation positions in a normalized coordinate system. This model can reveal the dependence of the distribution of the annihilation positions for scattered coincidences on the phantom size and source distribution. Introducing this annihilation position map into the GS-MLEM reconstruction algorithm, the actual activity distribution has converged about 2 times faster compared with that without using this map. As shown in Figure 6.10, the contrast and noise properties have improved compared to those obtained without using this geometrical constraint.

The intensity of the distribution of the annihilation positions within the TCA is a function of the source distribution and shape and size of the scanned object. In this study, we investigated this dependence using Monte Carlo simulations. The 2D histogram of the annihilation positions in the normalized coordinate were generated using the raw data simulated by GATE without accounting for the photon attenuation. The impact of the photon attenuation on the distribution of the annihilation positions becomes more significant as the phantom size increases, which is one possible reason for the inconsistency in the intensity distribution between Figure 6.3(d) and 6.5(d) for the same set of simulations. Another possible reason for the inconsistency of the distribution in Figure 6.3(d) and 6.5(d) is that when the simulated phantoms occupy almost the whole space within the scanner, part of the phantoms are outside of the FOV of the scanner, resulting in some coincidences being excluded from the measured data.

As indicated in Figure 6.5(a) and 6.5(b), if the distance from the point source to the center of the FOV equals the radius of the ring source, the distribution in the normalized coordinate for a point source is the same as that for a ring source except for a normalization factor. This conclusion can be derived by taking the ring source as a series of point sources, and the ring source distribution can be obtained by using the geometrical symmetry. The distribution for the cylindrical source can be obtained by combining the distribution of a set of ring sources with radii ranging from zero to the radius of the cylindrical source.

In this chapter, the distribution of annihilation positions was generated at an ideal energy resolution (0.1% FWHM @ 511keV). In the non-ideal energy resolution scenario, the photon energy of a scattered photon may be measured whether smaller or larger than its actual energy, which results in a larger or smaller TCA identified. However, this energy uncertainty only affects the perpendicular distance CO as illustrated in Figure 6.1(a). That is the non-ideal energy resolution blurs the distribution of annihilation positions in the vertical direction. Thus the distribution of annihilation positions for the limited energy resolutions can be obtained by blurring the ideal energy resolution distribution with a Gaussian distribution with the corresponding energy resolution in the vertical direction. This implementation will be discussed in Chapter 7.

6.5 Conclusion

A geometrical model to describe the distribution of the annihilation positions associated with scattered coincidences has been proposed in this chapter. This model can describe the distribution of the annihilation positions in a normalized coordinate system, which can be used to speed the image convergence and further improve the reconstructed image quality.

Chapter 7: A Generalized Scatter Reconstruction Algorithm for Non-ideal Energy Resolution PET Detectors

7.1 Introduction

In the previous chapters, the Generalized Scatter reconstruction algorithm has been developed which can include both true and scattered coincidences in the PET imaging reconstruction [71, 73, 76]. However, the implementation of the GS reconstruction algorithm on clinical PET scanners currently in use today is obstructed by the energy resolution they achieved. Firstly, the non-ideal energy resolution limits the ability to distinguish scattered coincidences from true coincidences simply based on the measured photon energy. Secondly, the TCA defined to confine the annihilation position for a scattered event cannot be accurately calculated based on the inaccurate photon energy.
In this chapter, the GS reconstruction algorithm has been adapted to the non-ideal energy resolution scenarios and its performance on a clinical PET scanner simulated by GATE [66-68] is reported.

7.2 Reconstruction Theory

Single scatter coincidences account for more than 80% of the measured scattered coincidences [1, 33]. Our scatter reconstruction algorithm is therefore based on the assumption that the measured data contains only true and single scattered events, and multiple scattered events are ignored in this study.

The non-ideal energy resolution of PET scanners makes it difficult to distinguish scattered coincidences from the trues based on the measured photon energy. To address this issue, a measured coincidence will be assigned as both a true and a scattered component with the probabilities P_{tr} and P_{sc}, which can be estimated using the energies (E_1, E_2) of the coincidence photons:

$$P_{tr} = \frac{P(E_1|tr)P(E_2|tr)}{P(E_1|tr)P(E_2|tr)+P(E_1|tr)P(E_2|sc)+P(E_1|sc)P(E_2|tr)} \ldots\ldots\ldots\ldots\ldots\ldots..(7.1a)$$

$$P_{sc} = \frac{P(E_1|tr)P(E_2|sc)+P(E_1|sc)P(E_2|tr)}{P(E_1|tr)P(E_2|tr)+P(E_1|tr)P(E_2|sc)+P(E_1|sc)P(E_2|tr)} = 1 - P_{tr} \ldots\ldots\ldots(7.1b)$$

where $P(E|sc)$ and $P(E|tr)$ are the probabilities that a photon with energy E has undergone a Compton interaction or not, which can be calculated based on the position of E in the energy spectrum as illustrated in Figure 7.1.

$$P(E|tr) = \frac{H_{tr}(E)}{H_{tr}(E)+H_{sc}(E)} \ldots\ldots\ldots\ldots\ldots(7.2a)$$

$$P(E|sc) = \frac{H_{sc}(E)}{H_{tr}(E)+H_{sc}(E)} \ldots\ldots\ldots\ldots\ldots(7.2b)$$

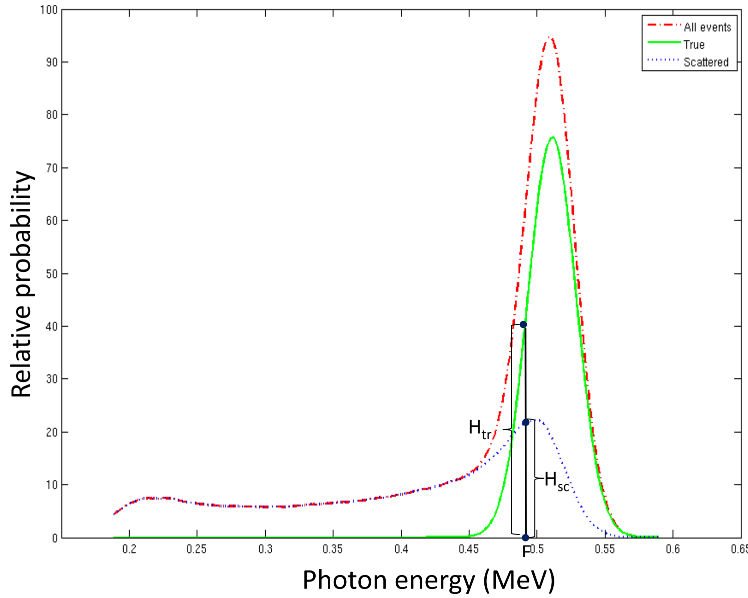

Figure 7.1 The energy spectrums for true and single scattered photons The shape of the spectrum depends on the energy resolution of a PET scanner, the properties of scintillator and the scatter fraction.

This energy spectrum is a function of the scatter fraction which in turn depends on the object being imaged, and the energy resolution of a PET scanner, which can be estimated using MC simulation.

After assigning the probabilities for the true and scattered components, the component that is assigned as a true coincidence will be reconstructed as such, but with a weight P_{tr} in the reconstruction algorithm.

For the scattered component, two methods have been proposed.

7.2.1 The Outer-Inner Arcs Method:

In the non-ideal energy resolution scenarios, the area within TCA should be as small as possible but still large enough to contain the annihilation position. The outer-inner arcs method is therefore proposed as a means to find, by trading off accuracy and blurring, the most appropriate area to confine the annihilation position. Firstly, the photon with the lower energy in a coincidence will be taken as the scattered photon (the photon measured at B in Figure 7.2 as an example). If both the coincident photons have an energy higher than 511 keV, this coincidence will be taken as a true event, since annihilation photons undergoing Compton interaction must have an energy no larger than 511 keV. Otherwise the possible energy range for the scattered photon is modeled with a Gaussian distribution centered at the energy of the scattered photon and with the FWHM equal to the energy resolution of the PET scanner, and lower and upper energy limits will be estimated by minus or plus some standard deviations from the scattered photon energy. The trade-off between the accuracy and blurring can be adjusted by setting different standard deviations when estimating the lower and upper energy limits for the scattered photon. The possible energy range for a photon with primary energy of 511 keV undergoing a Compton interaction is ~170-511 keV. Thus, if the estimated upper energy is greater than 511 keV, it will be taken as 511 keV. And if the measured lower energy is less than 170 keV, it will be taken as 170 keV. Based on the upper and lower energies for the scattered photon, two TCAs, representing the inner and outer boundaries of the possible TCAs as shown in Figure 7.2, can be identified.

Using the patient outline as a constraint [71], allows the annihilation position to be further confined, but the intersection points between the patient outline and TCA are sensitive to the scattered photon energy. As illustrated in Figure 7.2, we select the intersection Point C between the TCA defined using the lower energy and the patient outline, which is further to the higher energy photon detected position A. However, in the non-ideal energy scenarios, it is also possible that the scattered photon is measured at A. To address this, a line defined by connecting the intersection point C and A interacts with the perpendicular bisector of AB at D. Then we can define another inner arc that passes through this intersection point D, which will be used as the inner boundary of the annihilation position. Thus, the area between the outer and this inner arc will be used to confine the annihilation position for the scattered component in the reconstruction algorithm, which plays the same role as the LOR for the true component.

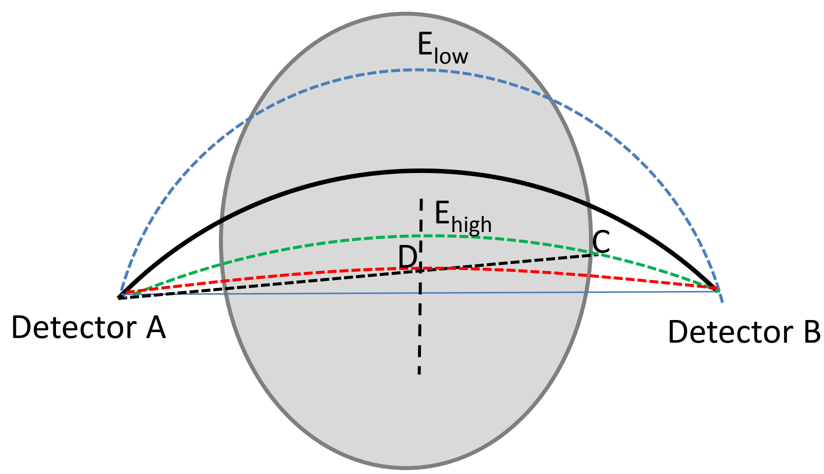

Figure 7.2 The outer arc (blue dash line) and inner arc (green dash line) are identified based on the lower and higher energy limits. The inner arc interacts with the patient outline at C, and the line defined by connecting Detector A to C interacts with the perpendicular bisector of AB at D. Another inner arc is defined by connecting A and B and passing through D. The area between the blue and red arcs will be used to confine the source position for scattered component in the non-ideal energy resolution situation.

7.2.2 Blurred Annihilation Distribution Method:

The blurred annihilation distribution method, as an alternative to the outer-inner arcs method, has been proposed to address the energy uncertainty of the measured photons when reconstructing the scattered component in the non-ideal energy resolution scenarios. As reported in Chapter 6, a geometrical model has been proposed to describe the distribution of the annihilation positions associated with scattered coincidences in the ideal energy resolution scenario. Following the previous work, this section will describe how to generate the distribution of annihilation positions in the non-ideal energy resolution situations. The distribution in the non-ideal energy resolution scenarios can be directly generated using GATE [66-68] simulations or in a more efficient way by blurring the distribution of ideal energy resolution with a Gaussian distribution. The GATE simulation-based method is straightforward but time-consuming, due to the need to resimulate for each specific PET scanner and patient/phantom. The following section will focus on a method to blur the ideal energy resolution distribution. As illustrated in Figure 7.3, the TCA defined based on the ideal energy resolution intersects with the perpendicular bisector of AB at Point C. The annihilation point S for a scattered coincidence in the normalized coordinate can be expressed by using the ratio of *AD* relative to *AB* as the abscissa and the ratio of *SD* relative to *CO* as the ordinate. Limited by the non-ideal energy resolution, the energy of the scattered photon may be measured to be higher or lower than the actual energy. This results in the calculated TCA intersecting the perpendicular bisector of AB either inside (at C') or outside (at C") of the actual TCA. The ordinate for the annihilation position in the non-ideal energy resolution equals the ratio of *SD* relative to the new length of OC′ (or OC″). Therefore, the limited energy resolution of the PET scanner blurs the distribution of annihilation positions in the vertical direction. By modeling the scattered photon energy with a Gaussian distribution with FWHM equal to the corresponding energy resolution and randomly sampling the possible scattered photon energies, the positions of the annihilation position in the normalized coordinate can be calculated and plotted into a histogram. This histogram describes the varying distribution of annihilation positions in the non-ideal energy resolutions for the scattered coincidences. Then this distribution map can be introduced into the reconstruction algorithm for reconstructing the scattered component with weight P_{sc}.

Since the ideal energy-resolution distribution generated is directly from the simulated data that already contains the information of the averaged photon attenuation, it removes the necessity of attenuation correction for the scattered component and only the difference relative to the averaged attenuation needs to apply for. The relative difference of attenuation Δatt can be defined for a material X as:

$$\Delta att = e^{-(\mu_{water}-\mu_X)\cdot d} \qquad \text{……………….(7.3)}$$

where μ_{water} is the linear attenuation coefficients of water and d is the thickness of material.

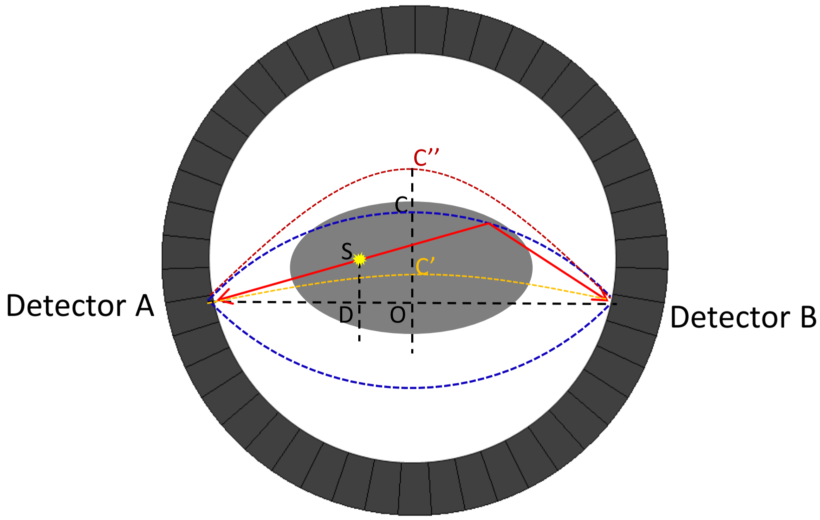

Figure 7.3 A diagram of Compton scattering in the object. Two anti-parallel 511 keV photons are generated at S, with the unscattered photon observed at A and the scattered photon observed at B. TCA shown as blue dotted curves, can be identified to describe all the possible scattered positions and encompass the annihilation position. O is the center of AB and CO is perpendicular to AB and intersects one-half TCA at C. For the non-ideal energy situations, the measured photon energy can be lower or higher than the actual energy, resulting in the calculated TCA intersecting with the perpendicular bisector of AB whether at C′ or C″ .

Thus, a measured coincidence has been split into a true, and a scattered component weighted with the probabilities P_{tr} and P_{sc}. These two components for each measured event with weights P_{tr} and P_{sc} can be reconstructed in the GS-MLEM [43, 44] algorithm in list-mode as follows:

$$\vec{f}_i^{n+1} = f_i^n \frac{1}{\sum_{j'=1}^{N} a_{j',i}} \sum_{j=1}^{N} a_{j,i} \frac{1}{P_{tr} \cdot \sum_{i'=1}^{p} a_{j,i'} f_{i'}^n + P_{sc} \cdot \sum_{i'=1}^{p} a_{j,i'} f_{i'}^n} \qquad i = 1, \dots, p$$

………………………………………..……………………………………..(7.4)

where p is the total number of pixels in the image, N is the total number of detected coincidences and $a_{j,i}$ is the element of the system matrix characterizing the probability that the annihilation photon detected as the j^{th} coincidence (whether scattered or not) were emitted from Pixel i.

The difference between this algorithm and the one in the ideal energy resolution case is that the summation for each coincidence has been split into two components with different weights P_{tr} and P_{sc}.

7.3 Phantom Measurements

To evaluate the performance of the proposed methods, a generic 2D PET scanner has been simulated with GATE [66-68] with an ideal energy resolution (0.1% FWHM at 511 keV). The PET scanner is a 24 ring system with 35 detector blocks per ring, which is arranged on a 44.3 cm radius ring. Each block contains a 12×24 LSO crystal array with dimensions of 6.3×6.3×30 mm^3. The detector covers a total 70 cm transaxial FOV and 15.7 cm axial FOV. The detectors have been shielded by lead slab, and only a slit with width of 20 mm was left for 2D acquisition. The energy window was set to 170-512 keV in order to detect all the true and single scatter coincidences. The measured photon energy was blurred in a post-processing step, which allowed us to generate several energy resolutions without having to resimulate the entire list-mode datasets. The ideal energy resolution data were blurred by an energy-dependent Gaussian distribution with energy resolution ranging from 1% to 12% FWHM individually.

To investigate the dependence of the spatial resolution of the reconstructed images from only scattered coincidences on the energy resolution of PET scanners, a 1 mm radius line source located at the center of a 25 cm radius cylindrical water phantom has been simulated. Images have been reconstructed from 3×10^5 scattered coincidences only by using the two proposed scattered component reconstruction methods.

The reconstructed image quality was evaluated on the simulated NEMA NU 2-2012 phantom [82], which contains four hot and two cold spheres in a warm background with a hot-to-background ratio of 4:1. Detail about this phantom can be found in Section 6.3.2. The image quality was tested using this standard. The evaluation of the proposed algorithm contains two parts.

In the first part, 1.38×10^6 scattered coincidences have been reconstructed using the outer-inner arcs method and the blurred annihilation distribution method respectively. This will be used to assess the performance of these two scattered component reconstruction methods before including true coincidences in the reconstruction. Images reconstructed from only scattered coincidences can lead to an understanding of the dependency of these scattered component reconstruction methods on the energy resolution of the PET scanners. For the outer-inner arcs method, the trade-off between the accuracy and the blurring is investigated by modeling the upper and lower energy limits with zero, one, and two sigma standard deviations from the measured photon energy in the Gaussian distribution. For the blurred distribution method, the distribution of annihilation position in the ideal energy resolution was blurred for the non-ideal energy resolutions ranging from 1%-12% and used for the imaging reconstruction.

In the second part, a total of 6×10^6 measured events with a scatter fraction of 50% were reconstructed using the proposed method for energy resolutions ranging from 1%-12% respectively. The CRC versus background variability, as an image-quality metric, is calculated for the reconstructed images, and the detailed criteria can be found in Section 6.2.2.

7.4 Results

7.4.1 The spatial resolution evaluation

Figure 7.4 shows the images of a 1 mm radius line source located at the center of a 20 cm radius cylindrical water phantom reconstructed from only scattered coincidences using the outer-inner arcs method for energy resolutions ranging from 1%-12%. The corresponding profiles along the center of the line sources are plotted in Figure 7.5. At the energy resolution of 1%, the FWHM of the line source has increased to 24 mm from the 8 mm for the ideal energy resolution. As expected, the FWHM of the line source increases as the energy resolution becomes worse. The FWHM of the line source increased to 56 mm at an energy resolution of 12%, which is about 7 times broader than that at the ideal energy resolution. Meanwhile, the profiles also become much noisier as the energy resolution decreases.

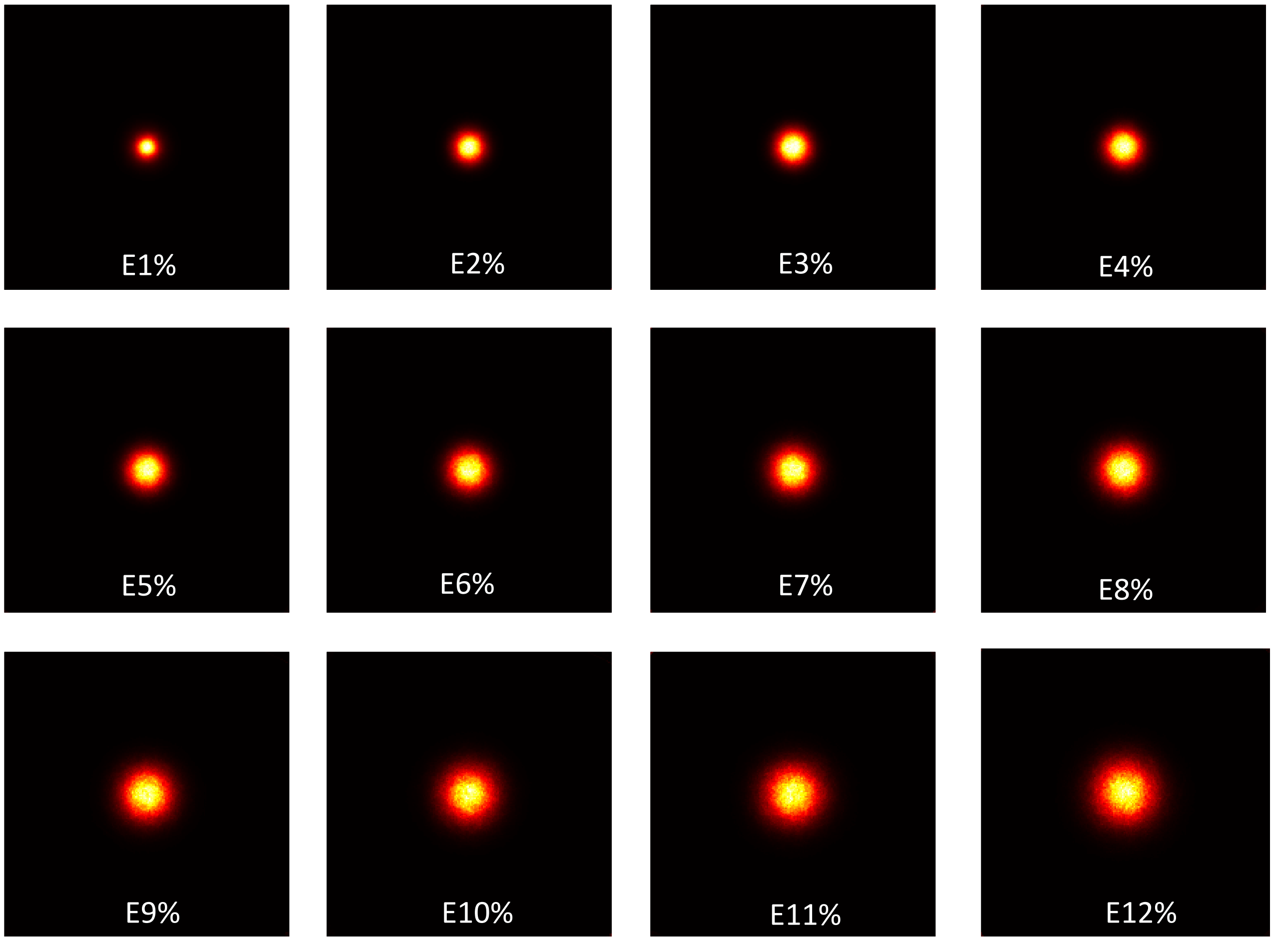

Figure 7.4 The images of a 1 mm radius line source reconstructed from only scattered coincidences by using the outer-inner arcs method with the energy resolutions ranging from 1%-12%.

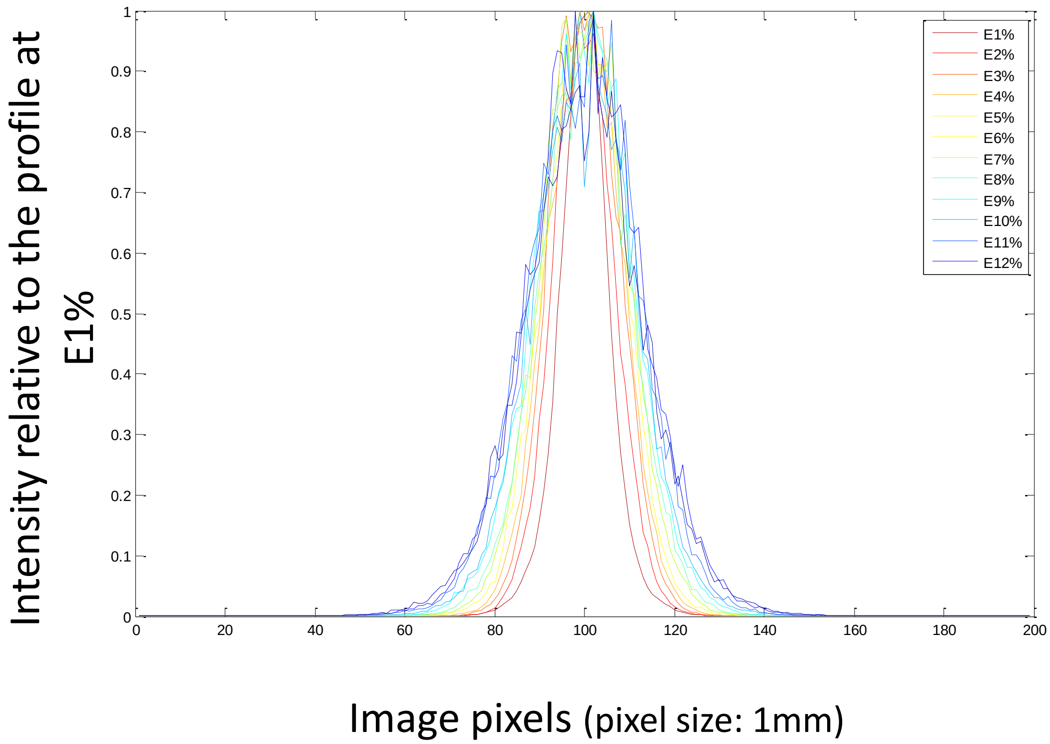

Figure 7.5 The profiles along the center of the images of a 1 mm radius line source reconstructed from only scattered coincidences using the outer-inner arcs method. As the energy resolution decreases, the profiles become broader and noisier. The pixel size of the reconstructed images is 1 mm.

The same line source was also reconstructed from only scattered coincidences by using the blurred annihilation distribution method. The blurred distributions of the annihilation positions for the line source with the energy resolutions ranging from 1%-12% are shown in Figure 7.6. As illustrated in this figure, the non-ideal energy resolution impacts the distributions only in the vertical direction, and the horizontal direction is independent of the energy resolution. As the energy resolution becomes worse, the distributions of annihilation positions stretch longer in the vertical direction. Building these blurred distributions into reconstruction, the images of a line source reconstructed from only scattered coincidences with energy resolutions ranging from 1%-12% are shown in Figure 7.7. The line sources in this figure almost have the same size with sharp edge. The profiles along the center of the line source are also plotted in Figure 7.8. The profiles are overlapped together for these images with the energy resolution ranging from 1%-12%. The FWHM of the line source in these images is 8 mm, which equals that at the ideal energy resolution. Compared with the PSFs obtained using the outer-inner arcs method (Figure 7.5), the profiles in Figure 7.8 are less noisy. These results also indicate that for the blurred annihilation distribution method the PSF is independent of the energy resolution for a line source at the center of a cylindrical phantom.

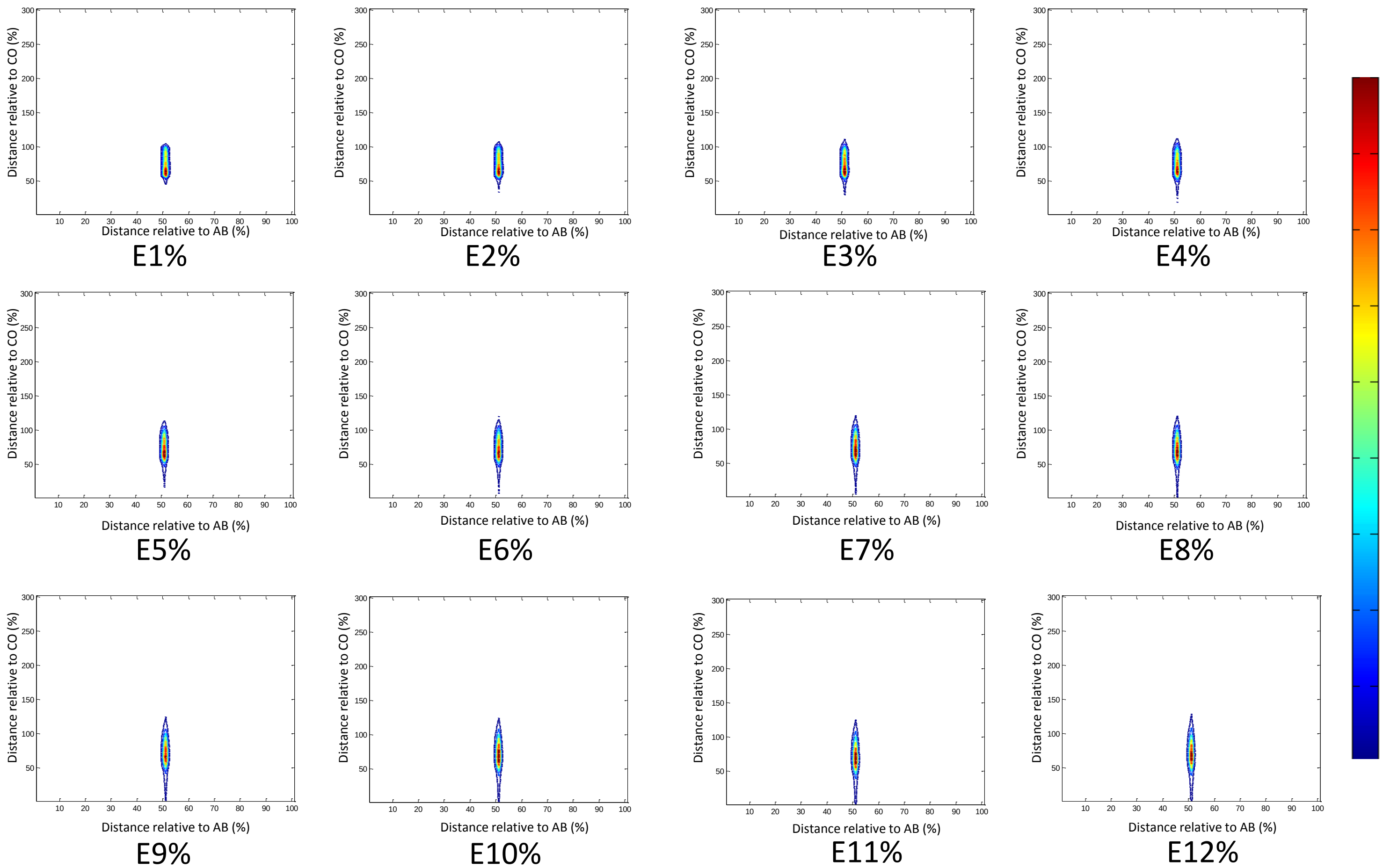

Figure 7.6 The blurred distribution of the annihilation positions for a line source located in the center of a 20 cm radius cylindrical water phantom for the energy resolution ranging from 1%-12%.

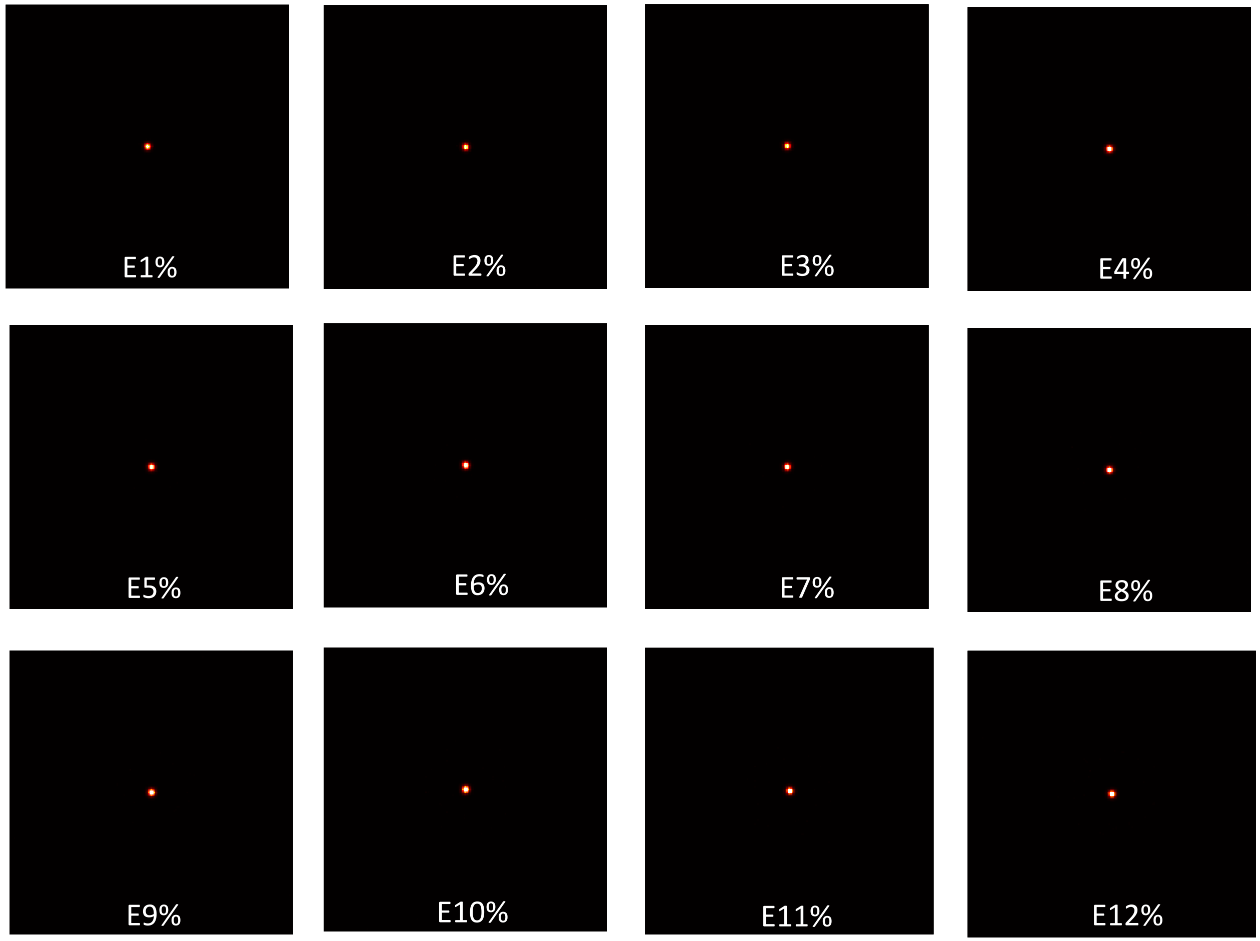

Figure 7.7 The images of a line source reconstructed from only scattered coincidences when introducing the blurred distribution of the annihilation positions into reconstruction for the energy resolution ranging from 1%-12%.

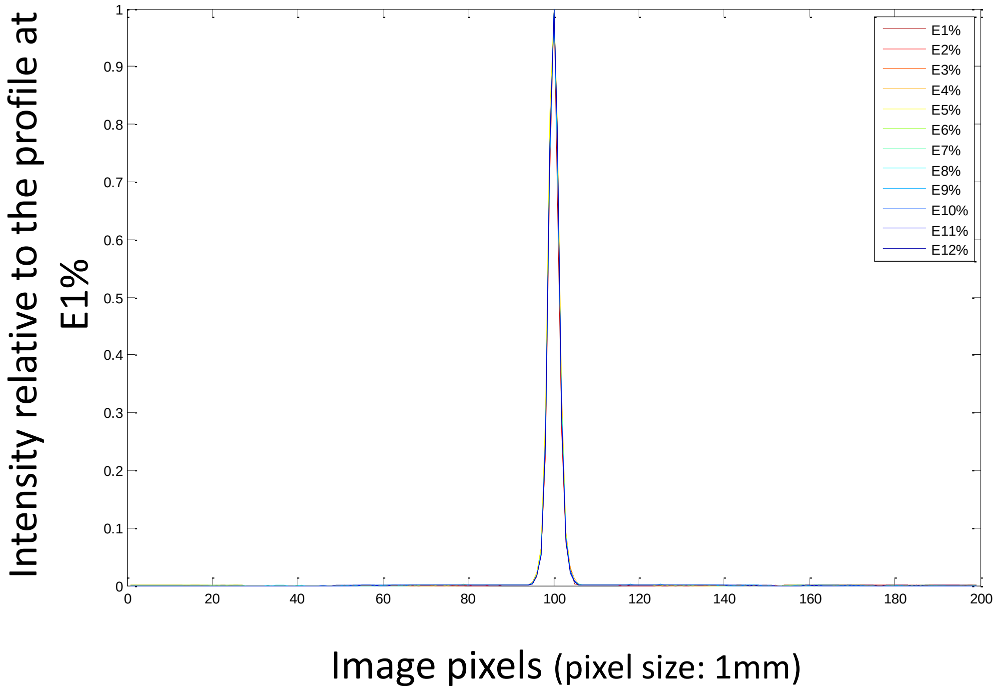

Figure 7.8 The profiles along the center of the images of a line source reconstructed from scattered coincidences by using the blurred annihilation distribution method. The pixel size of the reconstructed images is 1 mm.

7.4.2 Evaluation of images reconstructed from only scattered coincidences

Figure 7.9 shows the images of the NEMA NU2-2012 phantom reconstructed from 1.38×10^6 scattered coincidences using the TCA defined directly from the measured photon energy without accounting for the energy uncertainty. As illustrated in this figure, only the largest hot sphere in the NEMA phantom, with a diameter 3.7 cm, can be distinguished with an energy resolution better than 4%. The two cold spheres and the lung insert (in the center of the phantom) merge together for energy resolutions ranging from 1%-12%. The result indicates that the non-ideal energy resolution can seriously blur the image contrast reconstructed from scattered coincidences, if without properly addressing the energy uncertainties. This figure will also serve as a benchmark when comparing the image quality reconstructed by using the outer-inner arcs method and the blurred annihilation distribution method.

Figure 7.10, Figure 7.11, and Figure 7.12 show the images reconstructed from the same scattered data as in Figure 7.9 but by using the outer-inner arcs method with the upper and lower energy limits estimated by plus/minus zero, one, and two sigma from the measured photon energy respectively. Adding the patient outline constraint to the reconstructions shown in Figure 7.9 improves the image quality as shown in Figure 7.10. As shown in Figure 7.10, Figure 7.11, and Figure 7.12, the hot spheres with diameters of 3.7 cm and 2.8 cm can be recognized with an energy resolution better than 4%. Meanwhile, the two cold spheres and the lung insert can be clearly separated with energy resolutions of up to 3%. As expected, the contrast of the reconstructed images will decrease as the energy resolution becomes worse. The local details disappear with the energy resolution worse than 8% in these three figures, which leads to less valuable information from scattered events but still instead of noise contributing to the reconstructed images.

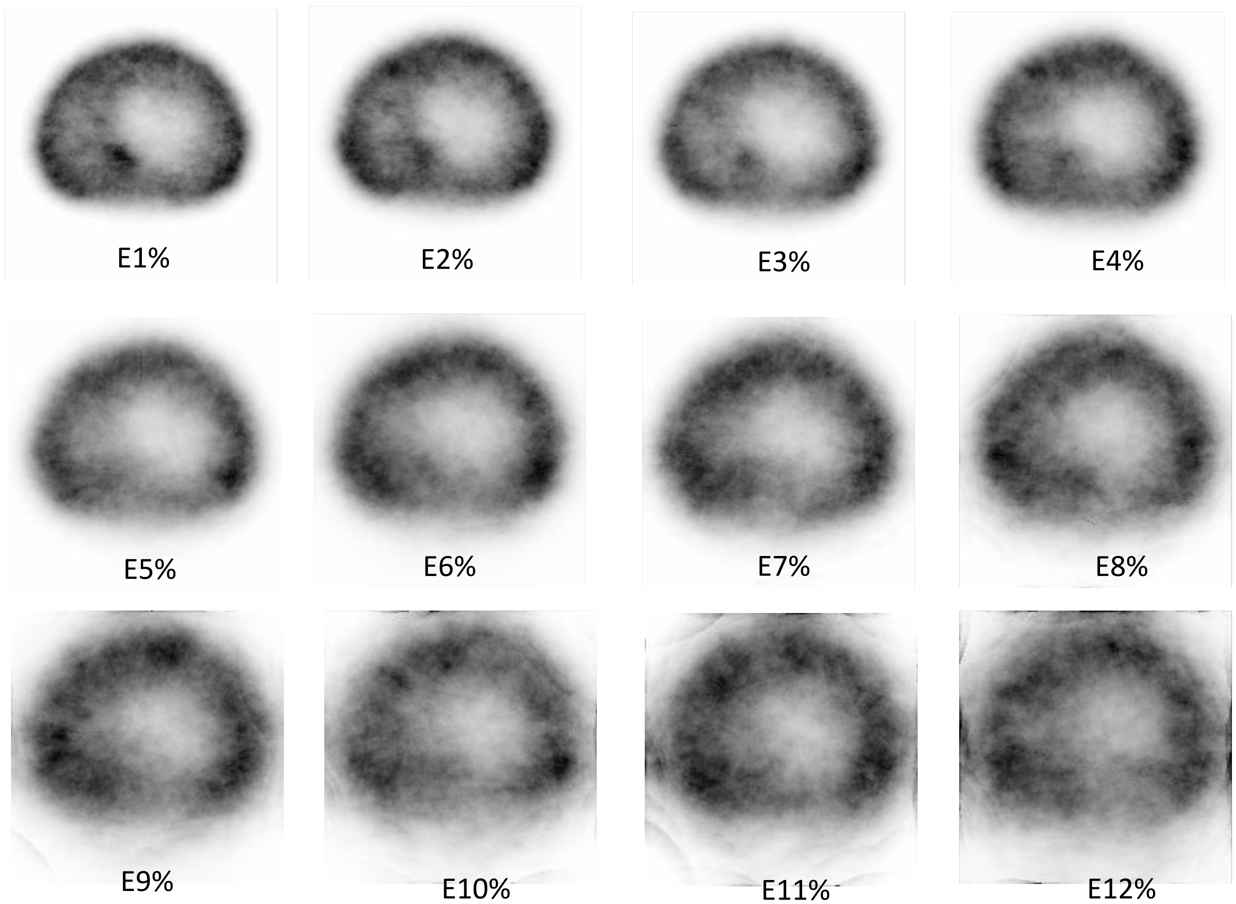

Figure 7.9 The images reconstructed from 1.38×10^{6} scattered coincidences based on the TCA defined directly using the inaccurate photon energy for the energy resolution ranging from 1%-12%.

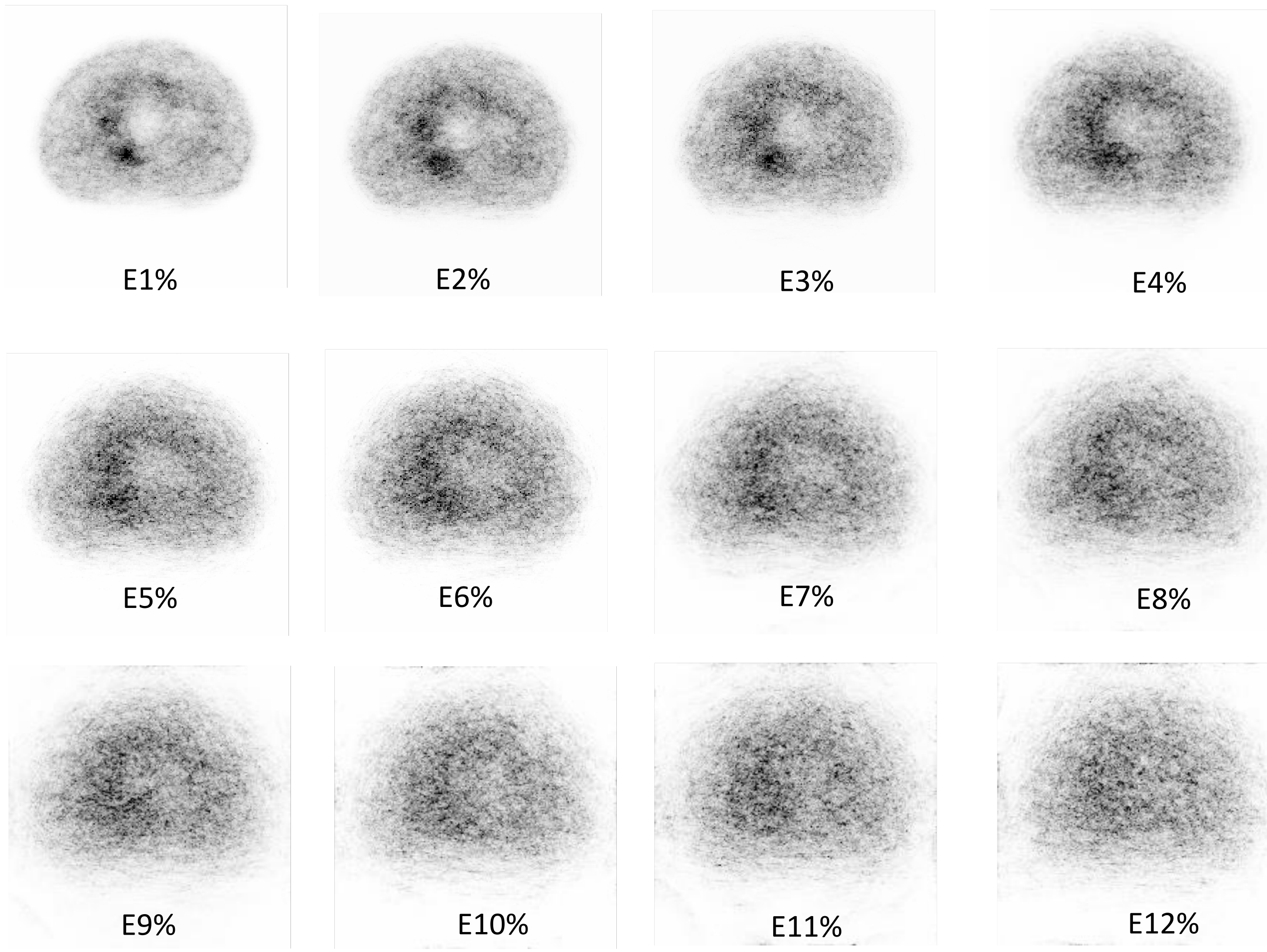

Figure 7.10 The images reconstructed from $1.38{\times}10^6$ scattered coincidences by using the outer-inner arcs method with the upper and lower energy limits estimated by plus/minus zero sigma from the measured photon energy and with patient outline constraints for the energy resolution ranging from 1%-12%.

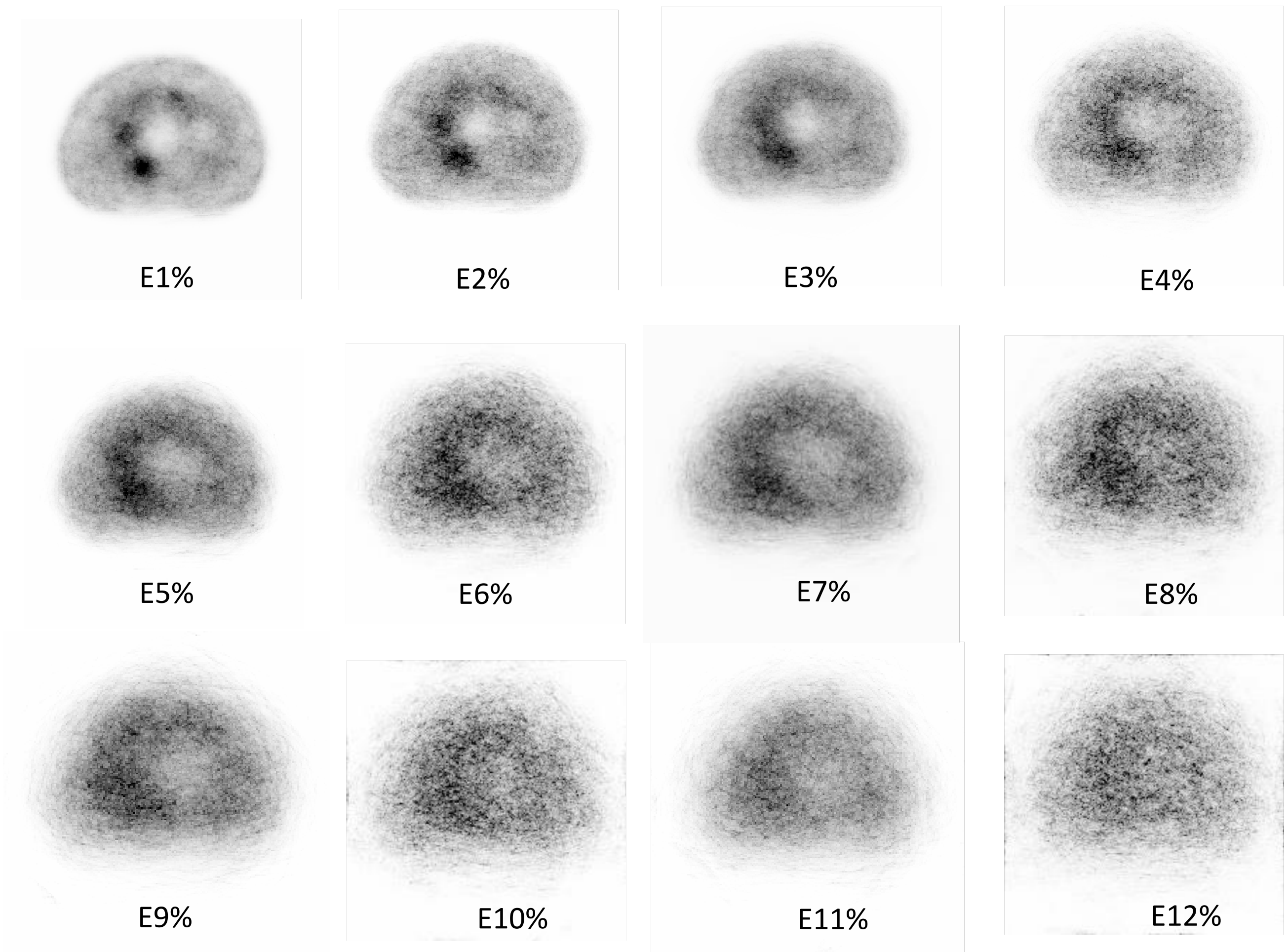

Figure 7.11 The images reconstructed from 1.38×10^{6} scattered coincidences by using the outer-inner arcs method with the upper and lower energy limits estimated by plus/minus one sigma from the measured photon energy and with patient outline constraints for the energy resolution ranging from 1%-12%.

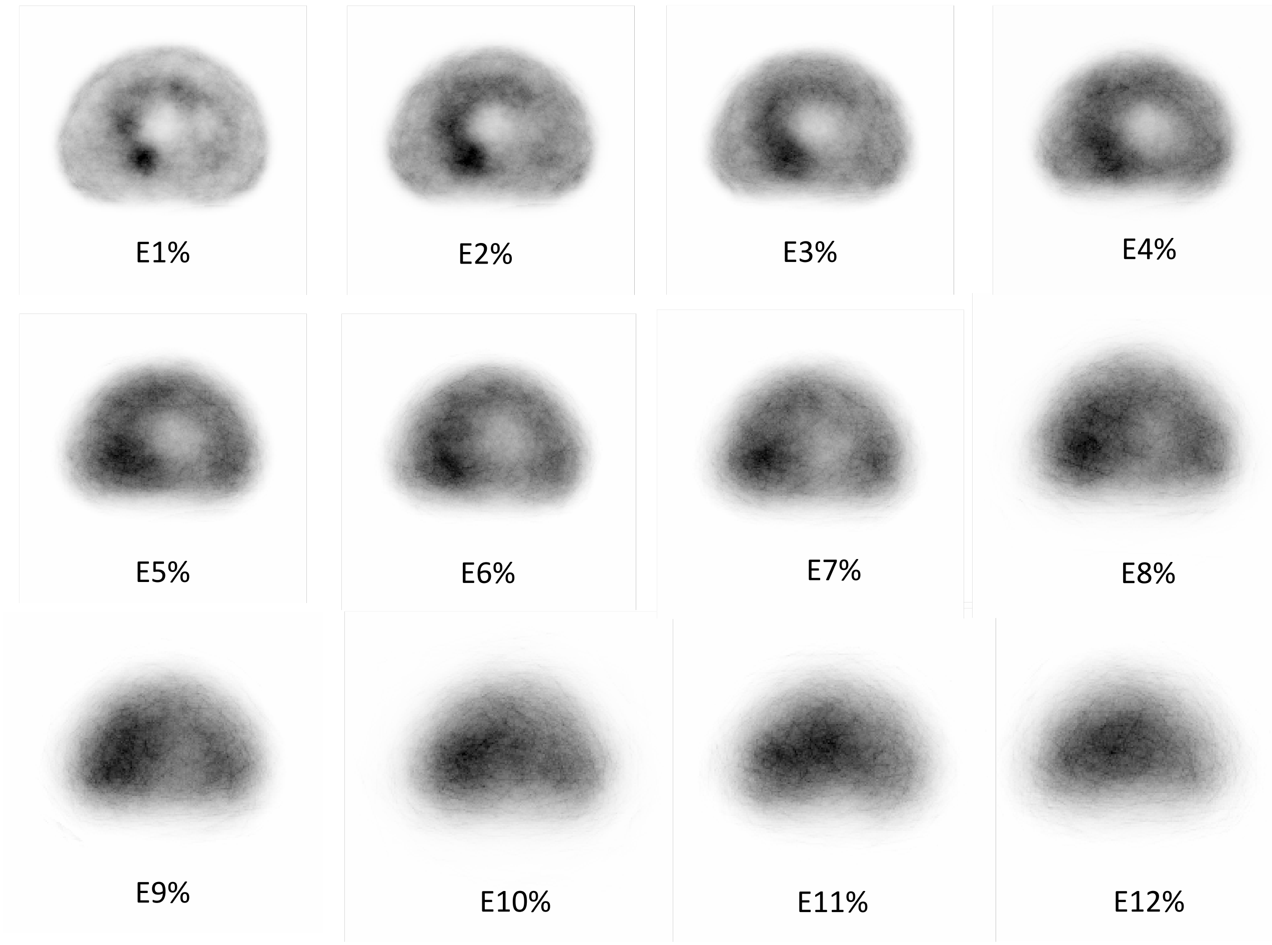

Figure 7.12 The images reconstructed from 1.38×10^{6} scattered coincidences by using the outer-inner arcs method with the upper and lower energy limits estimated by plus/minus two sigma from the measured photon energy and with patient outline constraints for the energy resolution ranging from 1%-12%.

As an alternative to the outer-inner arcs method, the blurred annihilation distribution method tries to characterize the distribution of annihilation positions within the TCA to reconstruct the scattered component for non-ideal energy resolutions. Figure 7.13 shows the blurred distribution maps of the NEMA phantom for the energy resolution ranging from 1%-12%. Building these distributions into the reconstruction, the same scattered coincidences data as used in Figure 7.9 was reconstructed using the blurred annihilation distribution method as shown in Figure 7.14.

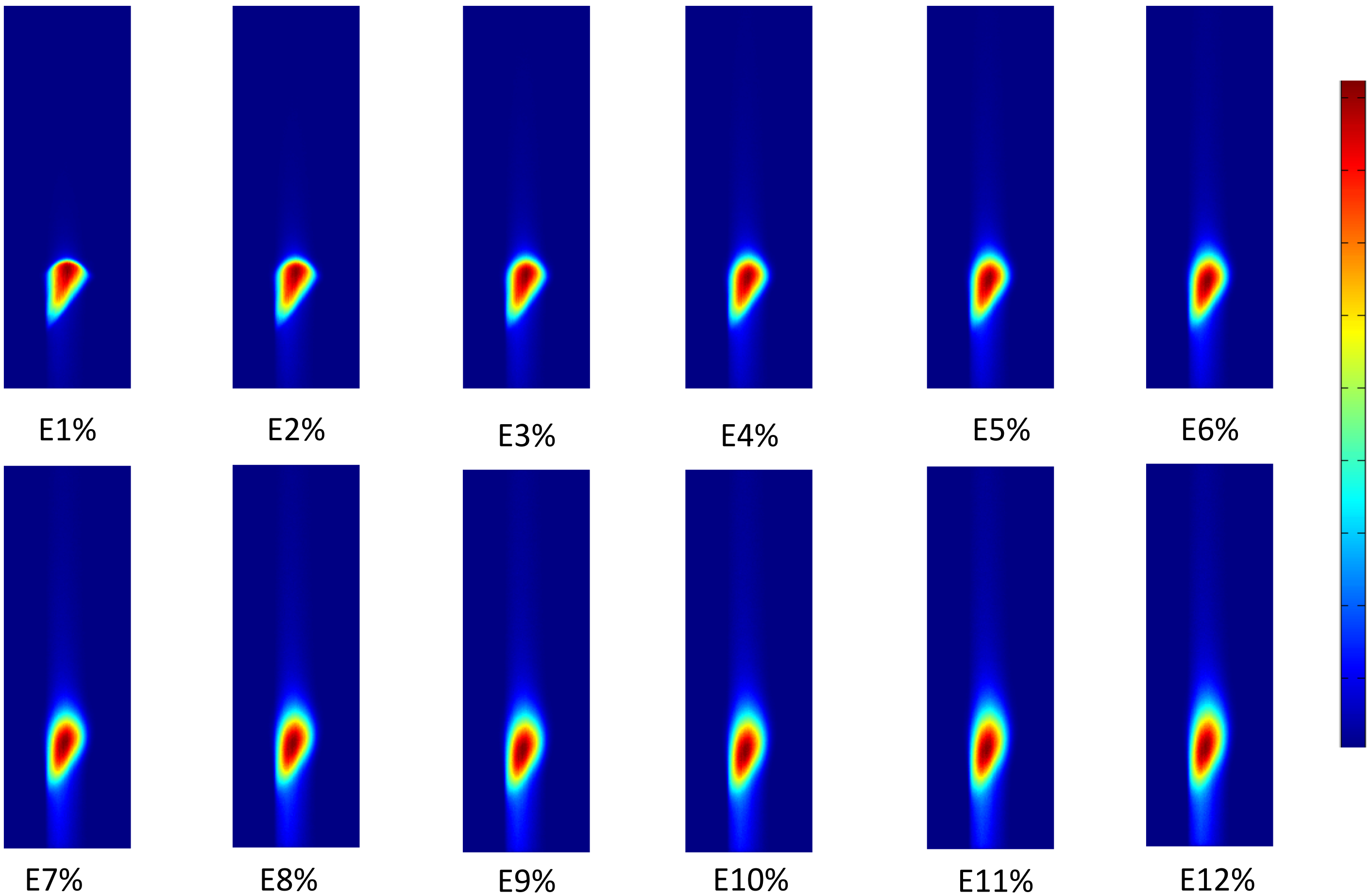

Figure 7.13 The blurred distribution of annihilation positions for the NEMA phantom with the energy resolution ranging from 1%-12%.

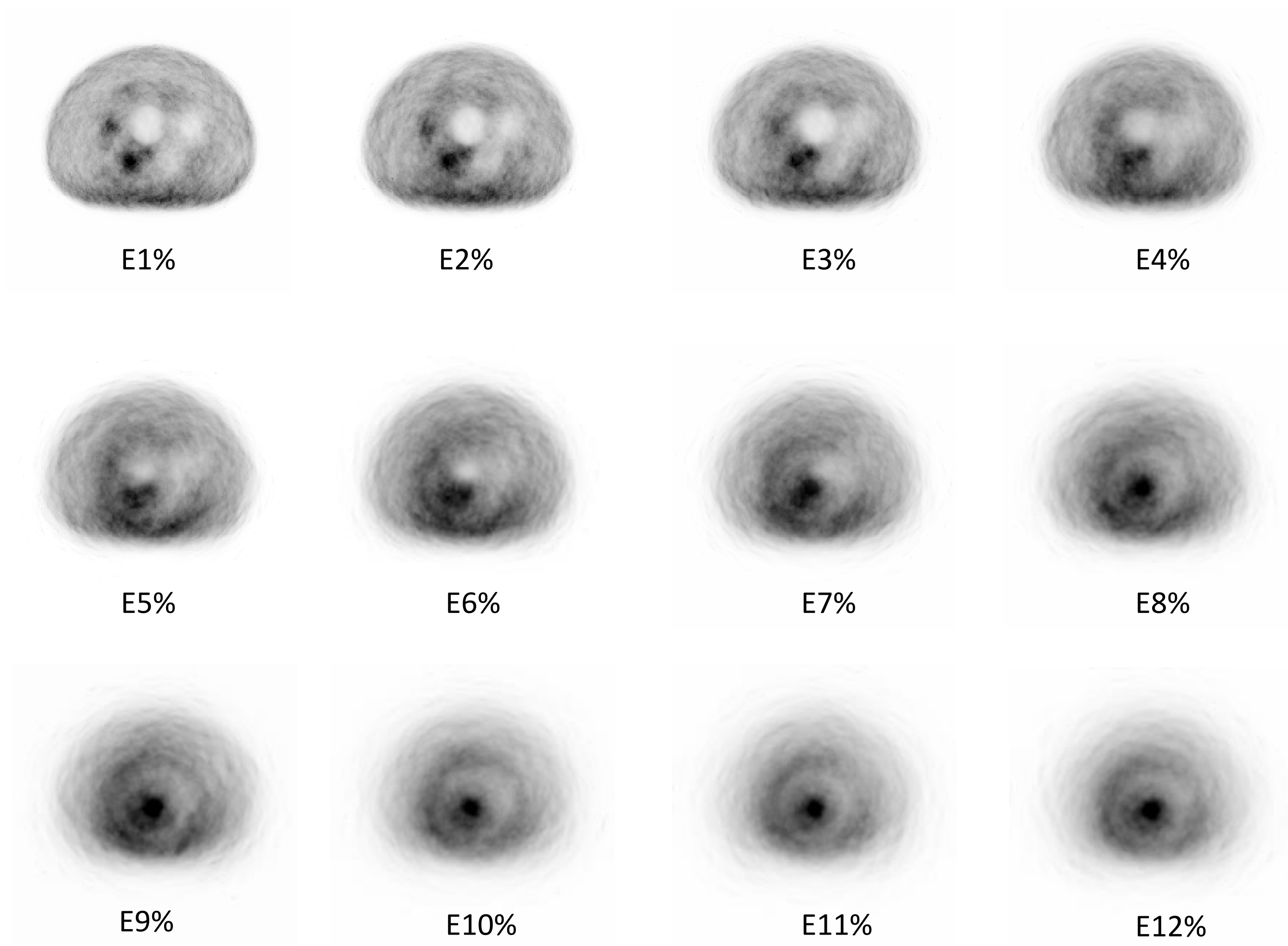

Figure 7.14 The images of NEMA phantom reconstructed from only scattered coincidences using the blurred annihilation distribution method with the energy resolution ranging from 1%-12%.

To quantitatively evaluate the reconstructed image quality, the correlations between the reconstructed images and ground-truth image as a function of the energy resolution were plotted in Figure 7.15. As shown in this figure, all the correlation curves decrease as the energy resolution becomes worse. The results with the outer-inner arcs method are in better agreement with the ground truth for all the energy resolutions, than are the results using the measured photon energy. For the outer-inner arcs method, the curve corresponding to the energy uncertainty modeled with one sigma has improved the correlation by 1.5%-4% and 0.5%-15% compared with that modeled with zero sigma and two sigma. Compared with that directly using the measured photon energy method, the corrections have been improved by 5%-23% for the outer-inner arcs method (modeled by one sigma) and by 7%-21% for the blurred annihilation distribution method.

Compared with these two scattered component reconstruction methods, the blurred annihilation distribution method can achieve 1%-2% better correlation when the energy resolution is better than 6% relative to the outer-inner arcs method modeled with one sigma. Beyond this energy resolution, the trend has reversed, and the outer-inner arcs method can bring more benefits into the scattered component reconstruction. Besides, the artifacts in the images reconstructed by using the blurred annihilation distribution method become more obvious due to the relative attenuation correction applied to the lung insert.

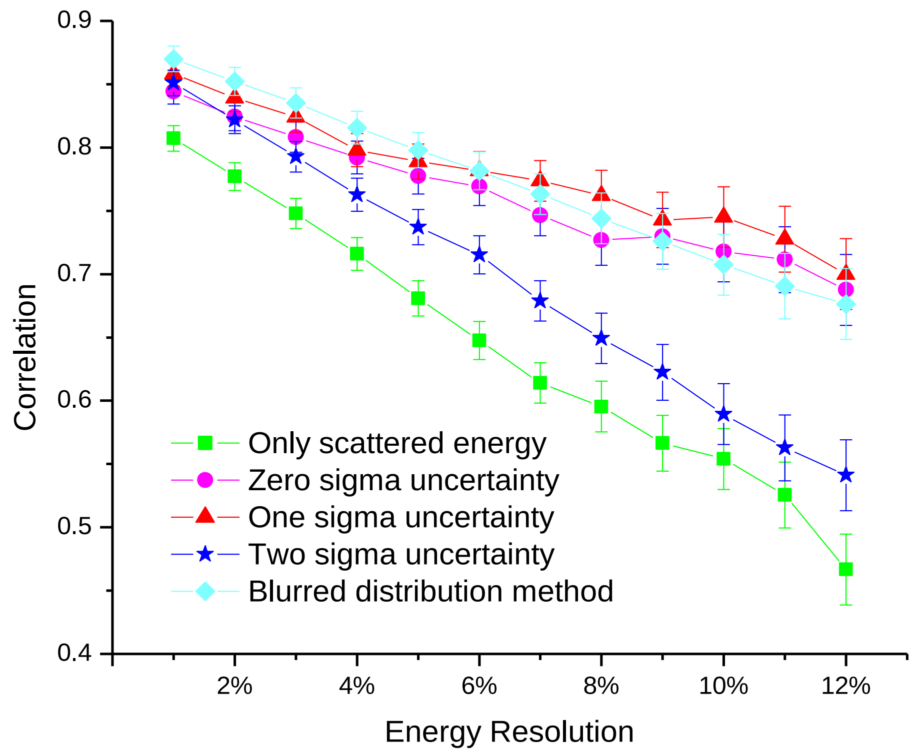

Figure 7.15 The correlation between the ground-truth image and the images reconstructed by directly using the measured photon energy, the outer-inner arcs methods with the energy uncertainty modeled with zero, one, and two sigma, as well as the blurred distribution method, as a function of the energy resolution.

7.4.3 Reconstruction from both true and scattered coincidences

Figure 7.16 shows the images reconstructed from 6×10^6 measured events with a scatter fraction of 50% as a function of the energy resolution ranging from 1% to 12%. The scattered component in this figure was reconstructed by employing the outer-inner arcs method. In contrast to the images reconstructed only from scattered coincidences, the dependency of the image quality on the energy resolution has been alleviated. The quantitative analysis of the contrast and noise properties for the four hot spheres and two cold spheres as a function of energy resolution was evaluated by using the CRC and RSD (represented by the error bar at each data point) as shown in Figure 7.17. The contrast has decreased by 5%-27% for the four hot spheres and by 33%-39% for the two cold spheres with the energy resolution ranging from 0-12%. Compared with the hot spheres, the CRCs for the cold spheres are more sensitive to the energy resolution.

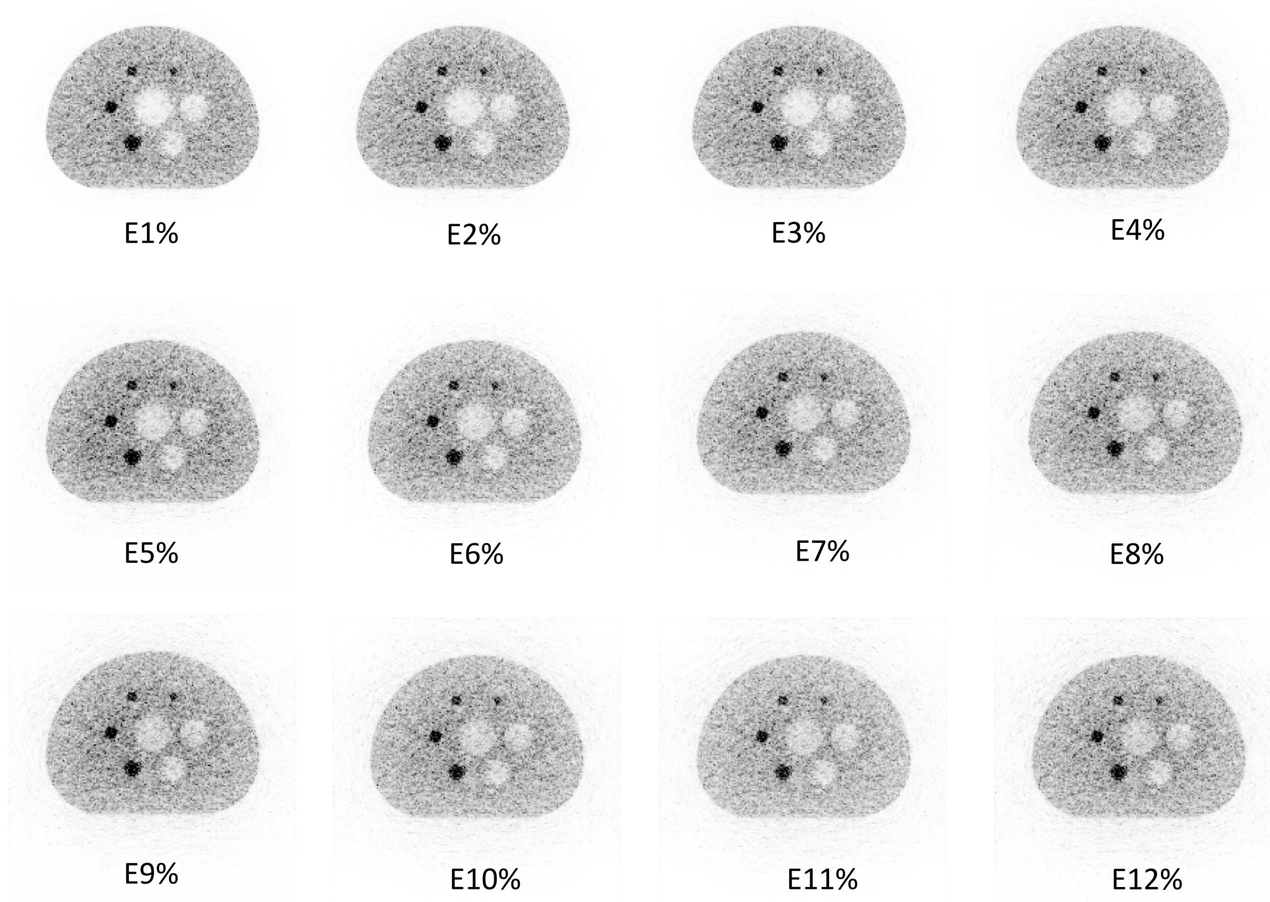

Figure 7.16 Images reconstructed from 6×10^6 measured events with a scatter fraction of 50% for the energy resolution ranging from 1-12% using the proposed method. The scattered component was reconstructed using the inner outer arc method with one sigma deviation and patient outline constraints employed.

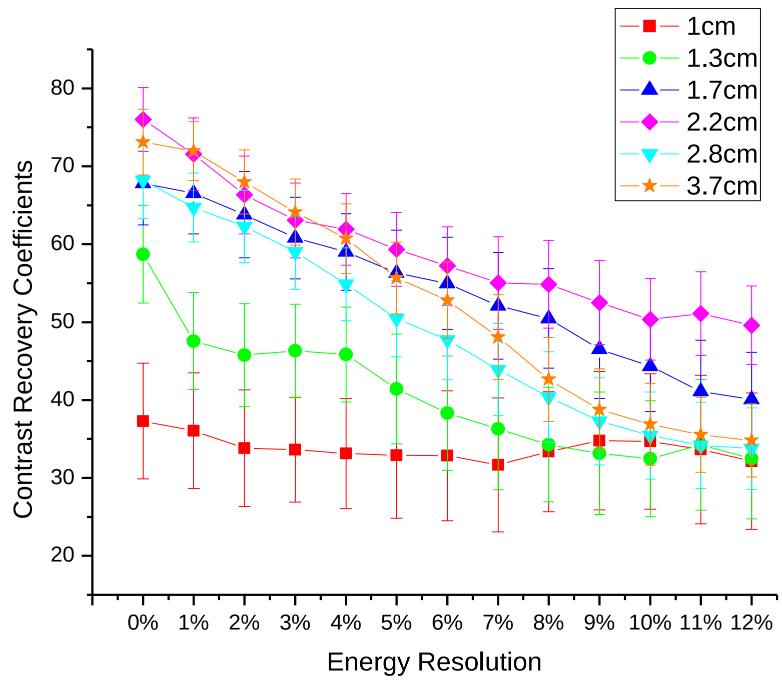

Figure 7.17 The contrast recovery coefficients and the relative standard deviation (represented by the error bar at each data point) for the spheres with different diameters reconstructed from 6×10^6 measured events with a scatter fraction of 50% by using the GS algorithm as a function of the energy resolution from ideal (0%) up to 12%. The scattered component was reconstructed using the inner outer arc method with one sigma deviation and patient outline constraints employed.

The contrast and noise properties for the four hot and two cold spheres in Figure 7.17 have been compared to their corresponding images that were reconstructed from the true events only, and the scattered correction based methods ignoring the energy resolution of the detectors. Figure 7.18, Figure 7.19, Figure 7.20, and Figure 7.21 show the comparisons for the four hot spheres with inner diameter 1 cm, 1.3 cm, 1.7 cm, and 2.2 cm respectively. Figure 7.22 and Figure 7.23 show the same comparisons for the two cold spheres with inner diameter 2.8 cm and 3.7 cm. For the 1 cm radius hot source as shown in Figure 7.18, the CRC is not sensitive to the energy resolution and fluctuates around that reconstructed from the true coincidences only, and is always higher than the scatter correction based method. This is because the smallest hot sphere contains only few pixels and suffers more statistical variations compared to the energy resolution impact. Except for the smallest hot source, the CRCs for the other three hot and two cold spheres, which are initially higher than that reconstructed from only true events, decrease with decreasing energy resolution. The CRC becomes lower than that reconstructed from only true events at the energy resolution of 1%-3% for the three larger hot spheres, and loses the benefits of incorporating scattered events into the reconstruction at an energy resolution around 8%-11% for the hot spheres. For the two cold spheres, the CRC tends to be worse than that reconstructed from only true events at the energy resolution of 2% and 4%, and inferior to the scatter correction based method at the energy resolution of 6% and 7% respectively.

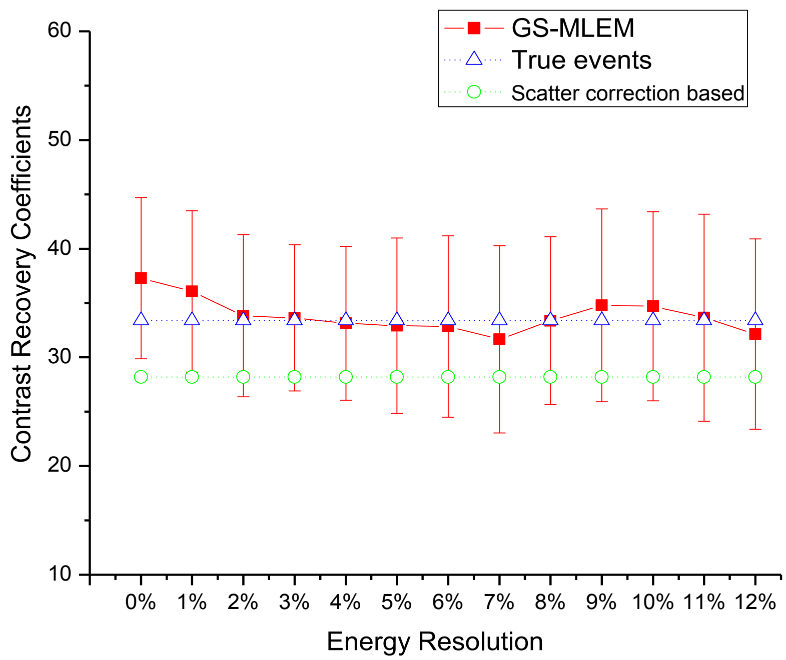

Figure 7.18 The contrast recovery coefficients and the relative standard deviation (represented by the error bar at each data point) for the smallest hot sphere with 1cm in diameter reconstructed from 6×10^6 measured events with a scatter fraction of 50% by using the GS algorithm as a function of the energy resolution from ideal (0%) up to 12%. The CRC for the reconstruction using the true events only, and the scatter correction based methods are also plotted in this figure as comparison.

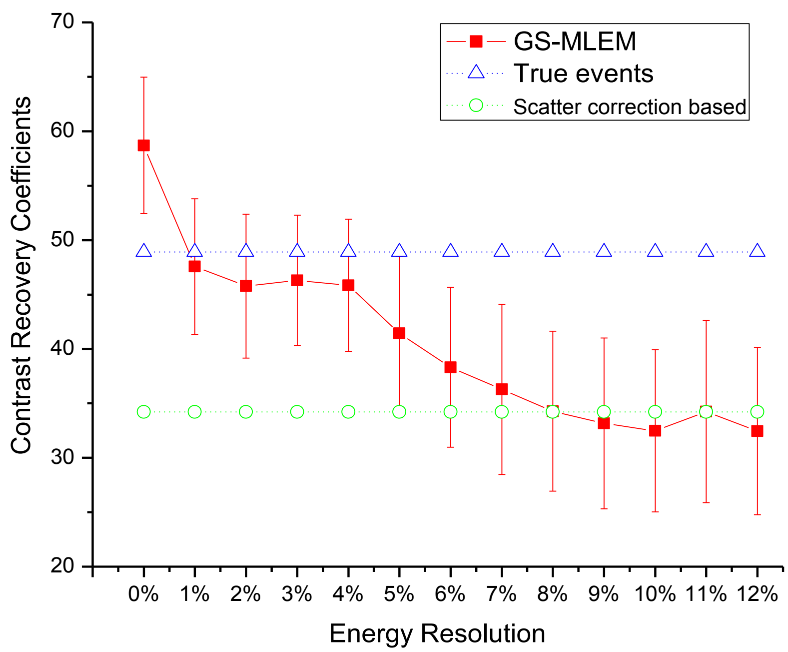

Figure 7.19 The contrast recovery coefficients and the relative standard deviation (represented by the error bar at each data point) for the hot sphere with 1.3 cm in diameter reconstructed from 6×10^6 measured events with a scatter fraction of 50% by using the GS algorithm as a function of the energy resolution from ideal (0%) up to 12%. The CRC for the reconstruction using the true events only, and the scatter correction based methods are also plotted in this figure as comparison.

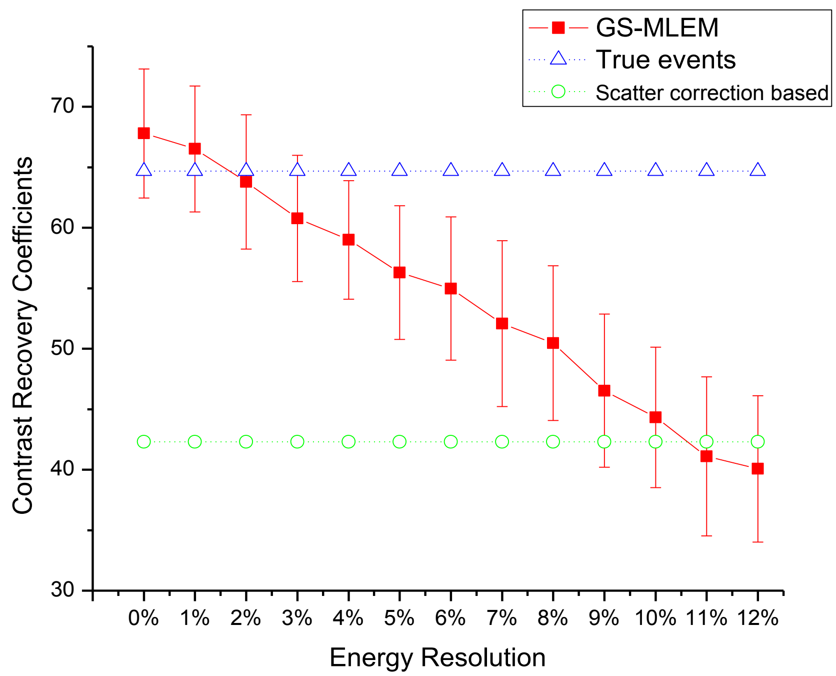

Figure 7.20 The contrast recovery coefficients and the relative standard deviation (represented by the error bar at each data point) for the hot sphere with 1.7 cm in diameter reconstructed from 6×10^6 measured events with a scatter fraction of 50% by using the GS algorithm as a function of the energy resolution from ideal (0%) up to 12%. The CRC for the reconstruction using the true events only, and the scatter correction based methods are also plotted in this figure as comparison.

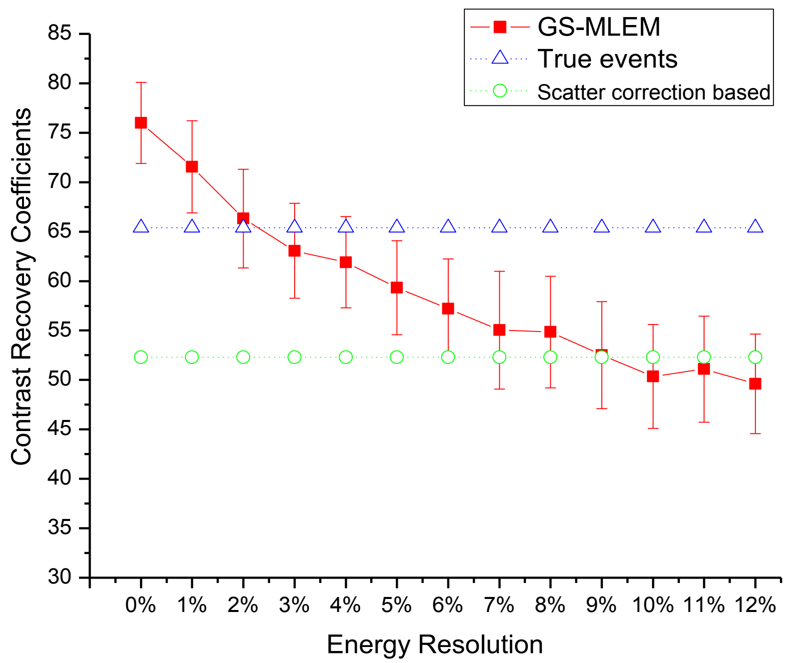

Figure 7.21 The contrast recovery coefficients and the relative standard deviation (represented by the error bar at each data point) for the hot sphere with 2.2 cm in diameter reconstructed from 6×10^6 measured events with a scatter fraction of 50% by using the GS algorithm as a function of the energy resolution from ideal (0%) up to 12%. The CRC for the reconstruction using the true events only, and the scatter correction based methods are also plotted in this figure as comparison.

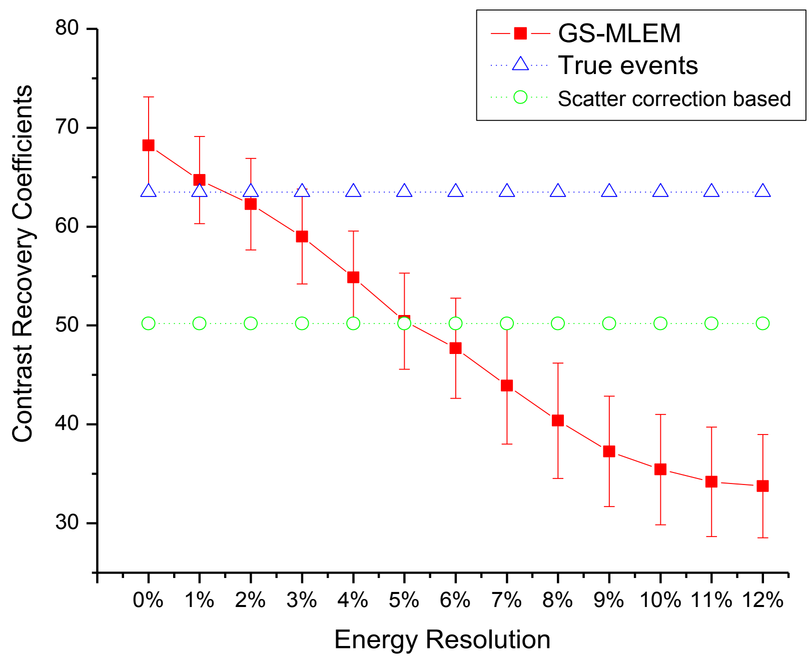

Figure 7.22 The contrast recovery coefficients and the relative standard deviation (represented by the error bar at each data point) for the cold sphere with 2.8 cm in diameter reconstructed from 6×10^6 measured events with a scatter fraction of 50% by using the GS algorithm as a function of the energy resolution from ideal (0%) up to 12%. The CRC for the reconstruction using the true events only, and the scatter correction based methods are also plotted in this figure as comparison.

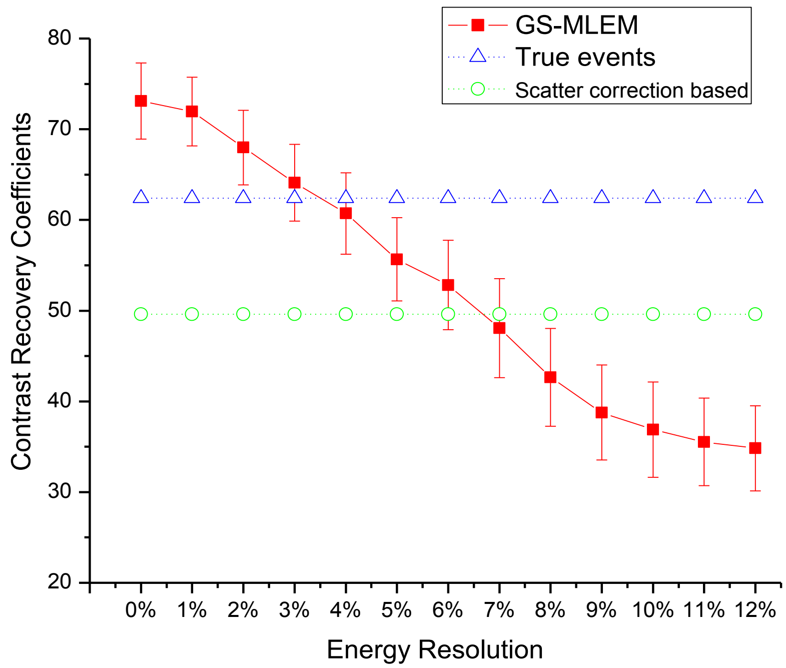

Figure 7.23 The contrast recovery coefficients and the relative standard deviation (represented by the error bar at each data point) for the largest cold sphere with 3.7 cm in diameter reconstructed from 6×10^6 measured events with a scatter fraction of 50% by using the GS algorithm as a function of the energy resolution from ideal (0%) up to 12%. The CRC for the reconstruction using the true events only, and the scatter correction based methods are also plotted in this figure as comparison.

7.5 Discussion

Reconstruction of the activity distribution from scattered coincidences by using the proposed method is mainly challenged by the non-ideal energy resolution of PET scanners in use today. When the photon energy is measured with large uncertainty, it will lead the defined TCA to deviate from its actual locus, which may result in the annihilation position being encompassed by a larger area or even lost within the area confined by TCA.

The outer-inner arcs method is trying to trade off this blurring and accuracy by modeling the scattered photon energy with a Gaussian distribution. By estimating the upper and lower energy limits with different standard deviations, a good trade-off can be achieved as illustrated in Figure 7.15. As expected, the spatial resolution and the image contrast reconstructed from only scattered coincidences will decrease as the energy resolution becomes worse. The blurred annihilation distribution method, as an alternative to the outer-inner arcs method, was also proposed and evaluated in this chapter. By characterizing the different probabilities of the annihilation position within the normalized TCA and built into the reconstruction, the contrast and noise properties of the reconstructed images in the ideal energy resolution scenario have been improved as demonstrated in Chapter 6. In the non-ideal energy resolution scenarios, the distribution of annihilation positions need to be blurred based on different energy resolution before being introduced into the reconstruction. The results shown in Figure 7.7 and Figure 7.8 indicate that the spatial resolution is independent of the energy resolution for a line source located at the center of a cylindrical phantom. The promising result is partially due to the narrow distribution in the normalized TCA for a line source located in the center of a cylindrical phantom. As for a distributed source, the results will be compromised at some degree as shown in Figure 7.14. The blurred annihilation distribution method can achieve better image correlation compared with that the outer-inner arcs method, which is, however, more sensitive to the energy resolution.

The GS reconstruction algorithm has been adapted to the non-ideal energy resolution scenario to incorporate both true and scatted events into reconstruction. Firstly, a measured event will be split into a true and a scattered component based on the position of the two measured photon energy in the energy spectrum. The energy spectrum depends on the energy resolution of the scanner and the scatter fraction, which can be estimated from Monte-Carlo simulations based on a raw reconstructed image as input. As expected, the image quality will decrease as the energy resolution of PET scanners becomes worse, which is as shown in Figure 7.17. The proposed algorithm can still achieve better contrast and noise properties compared with the scatter correction based method when the energy resolution is better than ~8% for hot spheres and ~6% for cold spheres. The core idea of this thesis is to extract the spatial information of annihilation position from the scattered coincidences by using the measured photon energy as a new parameter to improve PET image quality. As the energy resolution deteriorates, the uncertainty of the measured photon increases and the benefits of using the scattered photon energy as a new parameter in PET reconstruction are lost. Even though the GS reconstruction algorithm has been adapted to the non-ideal energy resolution, development of a PET scanner with higher energy resolution is still of paramount importance to fully exploit the benefits of scattered coincidences in PET.

7.6 Conclusion

A novel PET reconstruction algorithm, which can extract the radioactive distribution from both true and scattered coincidences, has been adapted to the limited energy resolutions of PET detectors. The proposed algorithm can achieve better contrast and noise properties compared with the scatter correction based method ignoring the energy resolution of the detectors up to the energy resolution of 8% and 6% for hot and cold spheres respectively. Development of PET with improved energy resolution is still highly demanded to fully exploit the benefits of scattered coincidences in PET.

Chapter 8: Summary and Future work

8.1 Summary

Quantitatively accurate PET images need to be corrected for scattered coincidences in the conventional PET reconstruction algorithms. Inaccuracy in the estimation of the scatter sinogram will introduce significant biases into the activity distribution. The subtraction based correction methods may destroy the Poisson nature of the measured data, reduce the system's sensitivity and amplify image noise.

In contrast to these scatter correction based methods, a novel PET reconstruction algorithm has been developed in this thesis, which can use both true and scattered coincidences to extract the radioactivity distribution in a consistent way. With the knowledge of the scattered photon energy and taking advantage of the kinematics of Compton scattering, the TCA can be identified to describe the locus of all the possible scattering positions and to encompass the annihilation position. As the scattering angle approaches zero, the shape of the TCA approaches the LOR for the true coincidences. Thus, true coincidences can be considered as the limit case of scattered events.

Chapter 3 has introduced the Generalized Scatter concept by taking the true coincidences as a subset of scattered coincidences and developed the Generalized Scatter reconstruction algorithm to incorporate both true and scattered coincidences into PET imaging reconstruction. This algorithm has been evaluated based on a simplified Deluxe Jaszczak phantom simulated by GATE [66, 67]. The results have demonstrated the feasibility of reconstructing PET activity distributions from only scattered coincidences. Compared with scatter correction based methods, the contrast and noise have improved by 3%-24.5% and 0.5%-12% respectively for a scatter fraction ranging from 10%-60%. Thus, incorporating scattered events into PET reconstruction eliminates the need for scatter correction, and also improves the system's sensitivity and image quality. The annihilation position within the TCA can be further confined by employing the patient outline as a constraint. As reported in Chapter 4, the contrast and noise of the reconstructed images improved by a further ~1%-11.6% and 05%-3.6% respectively, compared with that without using the patient outline as constraint.

Quantitative accuracy and artifact-free PET images need to account for photon attenuation. Chapter 5 has reported an effective and accurate attenuation correction method for scattered coincidences, which can be calculated by averaging the attenuation coefficient over all possible scattering positions along the TCA and weighted by the electron density and photon flux at each possible scattering position. The results have shown that the artefacts due to the photon attenuation have been removed, and the contrast and noise properties for the NEMA phantom have been improved by 9%-24% and 5%-6% respectively compared to scatter correction based methods.

In the first five chapters, the annihilation position was assumed uniformly distributed within the TCA. With this approximation, the activity distribution can be extracted from only scattered coincidences with acceptable degree, and both the contrast and noise properties of the reconstructed images have been improved when incorporating scattered coincidences into PET reconstruction. The uniform distribution of annihilation positions within the TCA is constrained by the radiopharmaceuticals' distribution and the scanned patients. To introduce this information into the GS algorithm, Chapter 6 has proposed a geometrical model in a normalized coordinate to characterize the distribution of annihilation positions associated with scattered coincidences. The proposed model can accurately reveal the dependence of the distribution of annihilation positions on the source distribution as well as the object sizes for scattered coincidences. When building this probability map of annihilation positions into the GS algorithm, it speeds up the reconstructed image convergence to the activity distribution and improves the image quality.

Precisely defining the TCA requires accurately measuring the scattered photon energy. However, this ability is compromised by the energy resolution achieved by the current PET scanners in use. In the non-ideal energy resolution scenarios, firstly the scattered coincidences cannot be distinguished from true events simply based on the measured photon energy. Secondly, the TCA cannot be determined accurately just based on the measured photon energy for a scattered coincidence. Chapter 7 has described two methods to address the scattered components in the non-ideal energy resolution situations. The outer-inner arcs method was proposed to trade off the accuracy and blurring when using TCA to confine the annihilation position. The blurred annihilation distribution method was developed based on the geometrical model proposed in Chapter 6, and adapted to the non-ideal energy resolution by only blurring the distribution of the annihilation positions in the vertical direction. The blurred annihilation distribution method can achieve better image correlation compared to the outer-inner arcs method, which is, however, more sensitive to the energy resolution. The results have shown that the proposed algorithm can achieve better contrast and noise properties compared with the scatter correction based method up to the energy resolution of 8% and 6% for the hot and cold spheres respectively. Development of PET scanners with high energy resolution is still highly demanded to fully exploit the benefits of scattered coincidences in PET imaging reconstruction.

8.2 Future work

This thesis has developed a Generalized Scatter PET reconstruction algorithm in 2D, which can use both true and scattered coincidences to extract radioactivity distribution in a consistent way. The benefits of including scattered coincidences into PET imaging reconstruction are twofold. Firstly, it eliminates the need for the scatter correction procedure carried out in the conventional PET reconstruction algorithms; Secondly, it improves the contrast and noise properties of reconstructed images, as well as the systems' sensitivity. However, to successfully implement the proposed reconstruction algorithm on clinical PET scanners, some issues still need to be addressed. Firstly, the TCA used to describe the scattered locus is closely related to the scattered photon energy. Even though Chapter 7 has developed two methods to deal with the non-ideal energy resolutions, the benefits of incorporating scattered events into reconstruction decreases as the energy resolution worsens. Developing high-energy resolution PET scanners is still paramount for fully exploiting the benefits of scattered coincidences. Commercially available PET scanners can only achieve the energy resolution of 10-20% [85-87], as most of the scintillators are based on gadolinium oxyorthosilicate (GSO) crystals or lutetium oxyorthosilicate (LSO) / lutetium-yttrium oxyorthosilicate (LYSO). Some research in developing new PET detectors with higher performance, especially better energy resolution, shows promise. It has been reported that the cerium-doped lanthanum bromide doped with Cesium ($LaBr_3$:Ce) as scintillators can achieve an energy resolution 4~5% [88]. The energy resolution averaged over all detector channels in a cadmium-tellurium

(CdTe) based PET scanner is 4.1% at 511 keV [89, 90]. It is worthy to mention that CdTe based brain PET scanner can achieve the energy resolution about 1.6% for 511 keV photons [91]. The performance of the proposed algorithm in this thesis was evaluated based on the GATE [67, 68, 92] simulation, and considering the improved energy resolution of some new scintillator based PET detectors. It is recommended to test this algorithm on these experimental and clinical high energy resolution PET scanners as future work.

It is possible that the annihilation photon undergoes multiple Compton interactions before escaping from the object. The scatter fraction for the multiple scattered coincidences accounts for about 12% of the measured events in a whole-body PET scanner [93]. Besides, when a 511 keV annihilation photon escapes from the object and interacts with a crystal/block, preferably it will deposit all of its energy within a crystal/block. However, it is possible that a photon only deposits part of its energy and then is scattered out of the crystal/block, then deposits the remaining energy in a neighboring crystal/block. Due to insufficient energy being deposited, the multiple scattered, the inter-crystal and inter-block scattered events are often rejected. However, the measured data is still contaminated by the inter-crystal, inter-block, and multiple scattered events, which cannot be distinguished from those single scattered within the object only based on the measured photon energy. The multiple scattered events can be reduced in the measured data by selecting a higher energy window. Besides, the information contributed from single scattered events becomes less as the scattering angle increases. Chapter 3 has investigated the trade-off between the available number of the scattered coincidences and the image quality as a function of the energy threshold, and concluded that ~350 keV as the low energy window can give a good trade-off. For the inter-crystal and inter-block scattered events, some research has demonstrated experimentally that inter-crystal and inter-block scattered events may be recovered as valid events with a corrected time stamp and estimated position of initial interaction [83, 94]. The sensitivity of the scanner can be improved by recovering the inter-crystal and inter-block scattered events. However, the accuracy of the recovery as indicated in [95-97] also depends on the detectors' geometry, the spatial and energy resolution, which needs further investigation.

Appendix A has investigated and demonstrated the feasibility of building the electron density map from scattered coincidences. However, the crosstalk between the activity and electron density map also appeared in the reconstructed images. This artifact arose because the scattered position cannot be accurately determined on the TCA, and the projection and backprojection in the reconstruction have to be along the entire TCA. Additional constraints need to be introduced into the reconstruction to remove this artifact, which is recommended as future work. Besides, the reconstruction of the activity distribution and the electron density map can be implemented in an iterative way: the electron density map provides the attenuation correction for the activity distribution reconstruction; the activity distribution will provide the probability of the scattered position along TCA for the electron density map reconstruction. Once these two reconstructions have been fully developed, the simultaneous reconstruction of activity and electron density should be addressed.

The GS reconstruction algorithm in this thesis is developed and tested based on 2D simulations. The ultimate goal is to implement this algorithm in a 3D PET scanner, where it will ultimately be of greater value. The implantation from 2D to 3D is straightforward, although the 3D geometry is more computationally complex. The projection and backprojection for the measured events in each iteration are carried out in parallel, which implies that the reconstruction can be sped up by using a graphics processing unit (GPU).

Appendix A: The Feasibility of Estimating the anatomical (electron density) map from Scattered coincidences in PET

A.1 Introduction

PET is a functional imaging modality, which lacks anatomical context. An anatomical image correlated with the functional image is required to account for the photon attenuation and to aid the interpretation of the activity distribution. Attenuation corrections are often carried out by using simplistic and often inaccurate approaches or by coupling a PET scanner to an x-ray CT or MRI system [98]. By assuming a regular geometric body outline and assigning constant tissue density within this object, the photon attenuation can be calculated using Equation (2.7). This method can produce images that are free of attenuation artifacts. However, it is prone to underestimate the attenuation [36]. Although the combination of PET and CT is used in commercial scanners, PET/CT has some limitations. Its major drawback is that the imaging is performed sequentially rather than simultaneously, which may introduce significant artifacts when registering the functional and anatomical imaging contents. In addition, CT is a snapshot of respiratory motion while PET is a time-averaged image, which may cause substantial artifacts in the reconstructed images. Due to the different energies used in PET and CT, the attenuation map measured at CT energies must be rescaled to the appropriate emission energy for PET attenuation correction [37]. In addition, radiation dose to patients is increased as a result of the CT scanning. Combining PET and MRI is challenging, as conventional PET systems use detectors that are sensitive to magnetic fields. However, there is not a simple energy scaling relationship from MR to PET to generate attenuation map due to MR measures aspects of protons while PET attenuation is affected by electron density [38].

The previous research has shown that it is possible to reconstruct anatomical images of electron density from scattered photons in CT [99-101]. As illustrated in Figure A.1, with knowledge of the incident photon energy, the TCA, as described in the previous chapters, can be identified based on the kinematics of Compton Scattering for a scattered coincidence in PET. These 2D circular arcs (or 3D surface by rotation of the 2D circular arcs around an axis connecting the two detectors), defined above, describe all the possible positions from which the coincident photons scattered. Different from the activity distribution reconstruction, the data will be projected or backprojected along the arcs (or surface in 3D) instead of over the area (or volume) confined by the arcs for the electron density map reconstruction.

The probability of a Compton interaction occurring is linearly proportional to the electron density at the scattering position. Backprojecting the scattered photons along the arcs connecting the two detectors will allow a Compton scattering probability map to be estimated. This map is a function of both radioactive tracer distribution and the electron density of materials. The influence of the varying photon fluence can be modeled by a sensitivity factor that varies for each pixel in the reconstruction algorithm.

In this appendix, it is assumed that the radioactive tracer distribution is already known. Once the two sets of reconstruction algorithms are fully developed, both the activity distribution and electron density map can be estimated simultaneously in an iterative manner, which will not be discussed here. This work has been presented, in part, at the 2014 IEEE Nuclear Science Symposium and Medical Imaging Conference [102]. The goal of this appendix is to investigate the feasibility of reconstructing the electron density map from scattered coincidences.

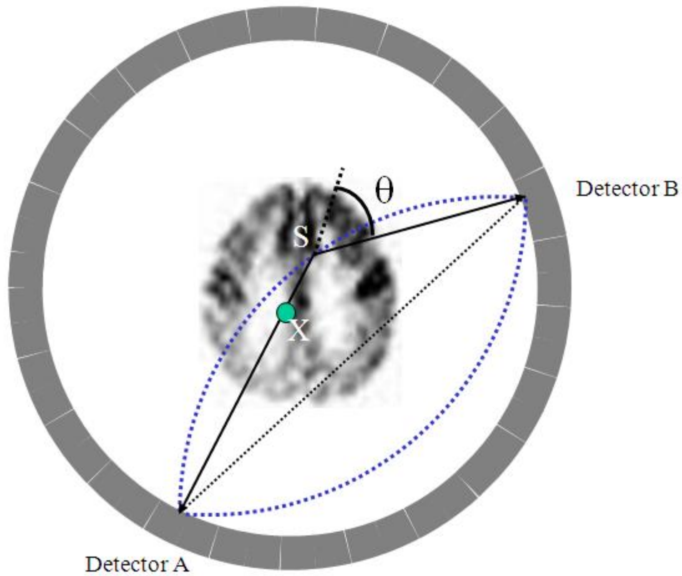

Figure A.1 A diagram of a Compton scattering event occurring in a patient. The two anti-parallel photons are generated at the annihilation position X shown by the green dot. The unscattered photon is observed by detector A while the other photon suffers a Compton scattering at S, deviates from its initial path by an angle θ and is detected by detector B. This figure also illustrates the two circular arcs (TCA), shown as blue dotted curves, which describe the locus of all possible scattering locations.

A.2 Methods and Materials

A.2.1 Reconstruction Theory

Firstly, the mean count of the single scattered coincidences with the unscattered photon observed at A and the scattered photon observed at B as shown in Figure A.1 can be calculated by the following expression:

$$\langle P_{\mathrm{AB}}(\theta)\rangle = \tau \oint_A^B \left[\int_A^S f_x \, dx\right] \cdot \rho_e(S) \cdot \frac{d\sigma_C^{KN}}{d\theta} \cdot \frac{1}{4\pi} e^{-\left(\int_A^S \mu dl + \int_S^B \mu' \, dl\right)} ds \ldots\ldots\ldots (\mathrm{A}.1)$$

where τ is the acquisition time, μ and μ' is the linear attenuation coefficients for the unscattered and scattered photons. The inner integral of source f_x from line segment A to S in the above expression represents the total photon fluence that can reach Point S. The possibility that the photons at S undergo a Compton scattering event is proportional to the electron density ρ_e at this point. The outer integral sums over all possible scattered points along the TCA.

Substitute Equation (A.1) into the system matrix and the ML-EM [43, 44, 65] in a list-mode form can be derived:

$$\overrightarrow{\rho_i}^{n+1} = \rho_i^n \frac{1}{\sum_{j'=1}^{N} a_{j',i}} \sum_{j=1}^{N} a_{j,i} \frac{1}{\sum_{i'=1}^{p} a_{j,i'} \rho_{i'}^n} \quad i = 1, \dots, p \ldots\ldots\ldots\ldots\ldots \text{(A.2)}$$

where p is the total number of pixels in the image, N is the total number of detected coincidences and $a_{j,i}$ is the element of system matrix representing the probability, weighted by the Compton differential cross section that the annihilation photons detected in the j^{th} coincidence were emitted from Pixel i.

The difference between this algorithm, which reconstructs the anatomical information, from the one that extracts the activity distribution in Chapter 3 and Chapter 4, is that the summation for each coincidence is along the arcs (or the surface in 3D) instead of over the area (or volume) confined by the arcs.

A.2.2 GATE simulation

To test the proposed method, a PET scanner with ideal energy resolution has been simulated by GATE [67]. The PET scanner is a 24 ring system with 35 detector block per ring; each block is a 12×24 LSO crystal array with dimensions of 6.3×6.3×30 mm^3. The detector covers a total 70 cm transaxial FOV and 15.7 cm axial FOV. Septa are also simulated in the system for 2D acquisition. The energy window was set to 170-511 keV in order to detect all single scatter coincidences.

Two water donut phantoms with inner and outer radii 10 and 20 cm, respectively, have been simulated, as shown in Figure A.2. The first one has a line source in the center. The other has two line sources, located 5 cm on the right and left of the center, respectively. The intensity ratio between the left and right line sources is set to 1:4.

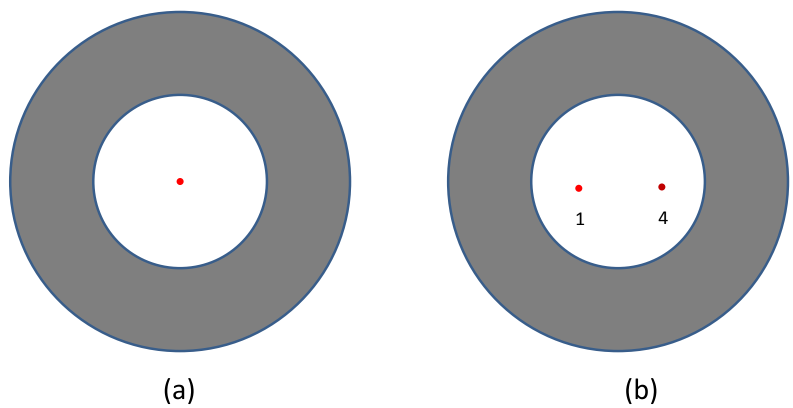

Figure A.2 The water donut-like phantom with inner and outer radii 10 and 20 cm, respectively, with (a) a line source in the center; and (b) two line sources located at 5 cm left and right of the center and with intensity ratio 1:4.

A.3 Results

Figure A.3 (a) shows the electron density map of a ring water phantom with a single source located in the center reconstructed from scattered coincidences by using the proposed method. The image demonstrates that the electron density map can be extracted from scattered coincidences for a single source. Figure A.3 (b) shows the electron density map of a ring water phantom with two, line sources located at 5 cm left and right to the center from scattered coincidences. When a phantom contains two sources or a distributed source, the crosstalk between the activity distribution, and electron density content began to appear. The area in the image near the sources looks brighter, which indicates that the crosstalk is highly related to the source distribution.

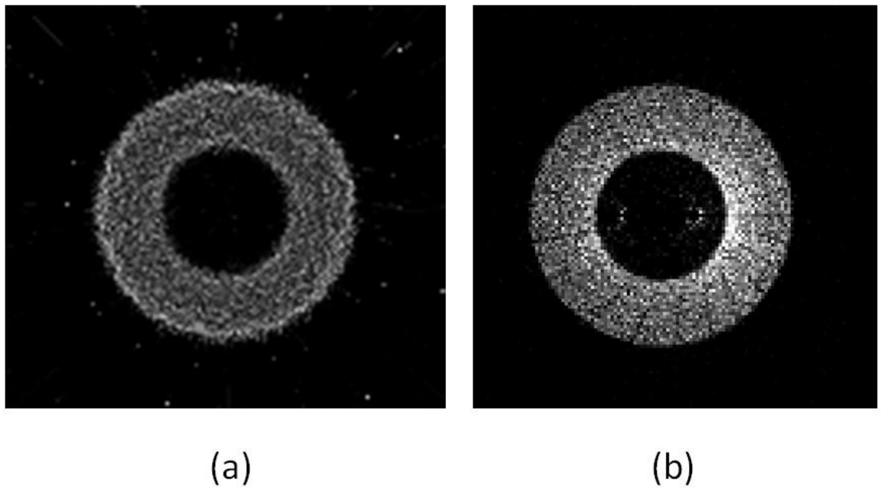

Figure A.3 The electron density map (anatomical image) of a circular ring uniform water phantom with (a) a single point source in the center; (b) two point sources with intensity ratio 1:4 were reconstructed from scattered coincidences.

A.4 Discussion

The feasibility of reconstructing the electron density map from scattered coincidences in PET has been investigated in this chapter. The results have showed that the electron density map can be extracted from scattered coincidences in a single source scenario. However, when two or more sources are involved, the crosstalk between the activity and the electron density began to appear. The reason for this phenomenon is that the scattered position along the TCA cannot be singularly determined in the two or more source scenarios. Instead, the algorithm projects and backprojects the data along the TCA and the weight assigned is proportional to the photon fluence that can reach each possible scattering position. This appendix only served as an initial feasibility study, and addressing the crosstalk is beyond the scope of this appendix and will be left as future work.

The reconstruction of electron density from scattered coincidences appears to be dependent on the energy resolution of the PET scanner, due to the TCA defined based on the scattering angle is closely related to the scattered photon energy. The uncertainty in the energy of the measured scattered photons can result in a large deviation of the TCA from its actual locus, and the electron density map is blurred as a result of the poor energy resolution.

A.5 Conclusion

A method for reconstructing the electron density map from scattered coincidences has been proposed, which has demonstrated the feasibility of extracting the electron density information from scattered coincidences. However, the crosstalk between the activity and the electron density map for two or more sources needs to be addressed for quantitatively accurate reconstruction of electron density in PET.

Appendix B: Equation for the TCA in the normalized coordinate

Figure B.1 shows half of the TCA for a scattered coincidence. One of the annihilation photons is detected at A, the other one undergoes a Compton scattering with the scattering angle θ and is detected at B. Suppose the distance between the two detectors A and B is d and take the center O of AB as the origin of the coordinate. Therefore, the radius of the circular curve TCA is:

$$R = \frac{d}{2\sin\theta} \ldots\ldots\ldots\ldots\ldots\ldots \text{(B.1)}$$

The equation for the circle to depict TCA is:

$$x^2 + (y + R\cos\theta)^2 = R^2 \ldots\ldots\ldots\ldots\ldots\ldots \text{(B.2)}$$

By solving y in this equation and only keeping the positive solution; we can get:

$$y = \sqrt{R^2 - x^2} - R\cos\theta \ldots\ldots\ldots\ldots\ldots\ldots \text{(B.3)}$$

The new coordinates (x′, y′) in the normalized coordinate can be obtained by normalizing x, y to the distance AB and OC respectively:

$$x' = \frac{x}{d} + \frac{d/2}{d} = \frac{x}{d} + \frac{1}{2} \ldots\ldots\ldots \text{(B.4a)}$$

$$y' = \frac{y}{R(1-\cos\theta)} \ldots\ldots\ldots\ldots\ldots\ldots \text{(B.4b)}$$

Substituting x′ and y′ into Equation (B.3), gives the equation for the TCA in normalized coordinates:

$$y' \cdot R(1-\cos\theta) = \sqrt{R^2 - d^2(x' - 0.5)^2} - R\cos\theta \ldots\ldots\ldots\ldots \text{(B.5)}$$

Using Equation (B.1), this can be reduced to:

$$y' = \frac{1}{1-\cos\theta}\left(\sqrt{1 - 4[(x' - 0.5)\sin\theta]^2} - \cos\theta\right) \ldots\ldots\ldots\ldots \text{(B.6)}$$

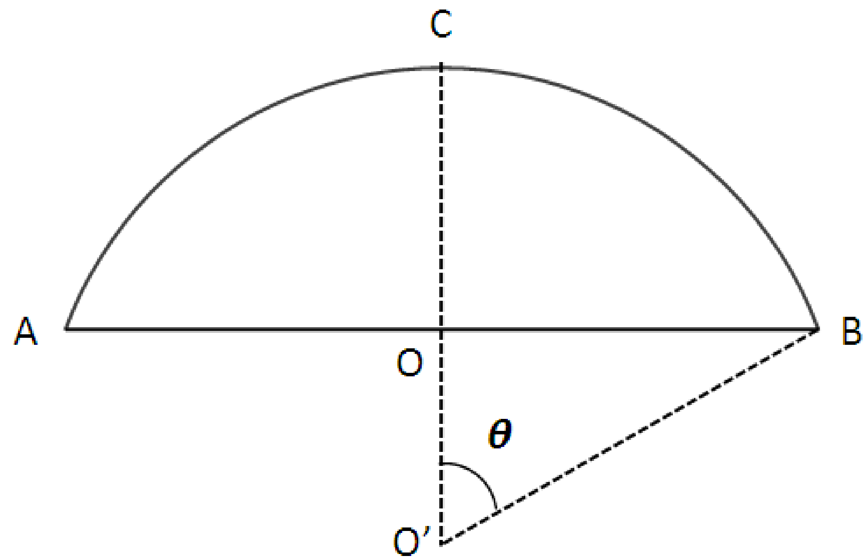

Figure B.1 A diagram of half of TCA associated with a scattered event. One of the two annihilation photons is detected at A, the other one undergoes a Compton scattering with the scattering angle θ and detected at B. O is the origin of the coordinate, and O′ is the center of the circle where TCA lies.

Appendix C: Publications and Communications

C.1 List of Patents

Stephen Pistorius, Hongyan Sun, "**Systems and Methods for Improving the Quality of Images in a PET Scan,**" (Note: the activity distribution reconstruction using scattered coincidences in PET)

PCT Publication No.: WO2013177661A1, Date of Publication: Dec 05, 2013

United States Patent Granted, No.: US-8866087, Date of Publication: Jun 12, 2014.

Stephen Pistorius, Hongyan Sun, "**Systems and Methods for Improving the Quality of Images in a PET Scan,**" (Note: the electron density reconstruction using scattered coincidences in PET)

United States Patent Pending, No.: US20140374607A1, Date of Publication: Dec 25, 2014.

C.2 List of Publications

H. Sun and S. Pistorius, "A Geometrical Model to describe Annihilation Positions associated with Scattered Coincidences in PET: A Simulation-based study," ***IEEE Transactions on Computational Imaging,*** submitted.

H. Sun and S. Pistorius, "Attenuation Correction for a PET Generalized Scatter Reconstruction Algorithm," drafted, 2014

H. Sun and S. Pistorius, "Evaluation of Image Quality Improvements When Adding Patient Outline Constraints into a Generalized Scatter PET Reconstruction Algorithm," ***ISRN Biomedical Imaging***, 2013.

H. Sun and S. Pistorius, "Evaluation of the Feasibility and Quantitative Accuracy of a Generalized Scatter 2D PET Reconstruction Method," ***ISRN Biomedical Imaging***, 2013.

C.3 List of Conference Publications

H. Sun, M. Teimoorisichani, B. McIntosh, G. Zhang, H. Ingleby, A. Goertzen, S. Pistorius, "Simultaneous estimation of the radioactivity distribution and electron density map from scattered coincidences in PET: A project overview", ***2015 World Congress on Medical Physics and Biomedical Engineering,*** Toronto, Canada, June 7-12, 2015.

H. Sun, S. Pistorius, "Extracting PET activity distribution from scattered coincidences for non-ideal energy resolutions by modeling the probabilities of annihilation positions within a generalized scattering reconstruction algorithm", ***2015 World Congress on Medical Physics and Biomedical Engineering,*** Toronto, Canada, June 7-12, 2015.

H. Sun, G. Zhang, S. Pistorius, "Turning Noise into Numbers: An investigation into the use of scattered photons to improve PET imaging quality", ***2015 Canadian Radiation Protection Association Conference,*** Winnipeg, Canada, 2015. (**The Winner of the Anthony J. MacKay Student Paper Contest)**

G. Zhang, H. Sun, S. Pistorius, "Electron Density Reconstruction from Scattered Coincidences for Attenuation Correction in Positron Emission Tomography", ***The 2015 Fully 3D Reconstruction Meeting***, Seattle, Washington, Newport, RI, USA June 1-4, 2015.

H. Sun, S. Pistorius, "A Generalized Scatter Reconstruction Algorithm for Limited Energy Resolution PET Detectors," ***IEEE Nuclear Science Symposium & Medical Imaging Conference (NSS-MIC)***, Seattle, Washington, Nov 8-15, 2014.

H. Sun, S. Pistorius, "Characterization the annihilation position distribution within a geometrical model associated with scattered coincidences in PET," ***IEEE Nuclear Science Symposium & Medical Imaging Conference (NSS-MIC)***, Seattle, Washington, Nov 8-15, 2014.

G. Zhang, H. Sun, S. Pistorius, "Feasibility of Scatter Based Electron Density Reconstruction for Attenuation Correction in Positron Emission Tomography," ***IEEE Nuclear Science Symposium & Medical Imaging Conference (NSS-MIC)***, Seattle, Washington, Nov 8-15, 2014.

H. Sun, S. Pistorius, "Simultaneous reconstruction of both true and scattered coincidences using a Generalized Scatter reconstruction algorithm in PET," ***The Canadian Organization of Medical Physicists (COMP) 60th Annual Scientific Meeting,*** Banff, Canada, July 9-12, 2014.

H. Sun, S. Pistorius, "Simultaneous reconstruction of both true and scattered coincidences in PET," ***16th Annual CancerCare Manitoba Research Day for Trainees in Clinical & Basic Sciences***, Winnipeg, Manitoba, Canada, May 8, 2014.

H. Sun, S. Pistorius, "Attenuation Correction for a Generalized Scatter Reconstruction Algorithm in PET," ***IEEE Nuclear Science Symposium & Medical Imaging Conference (NSS-MIC)***, Seoul, South Korea, Oct27-Nov2, 2013.

H. Sun, S. Pistorius, "An investigation into the use of scattered photons to improve 2D PET functional imaging quality," ***15th Annual CancerCare Manitoba Research Day for Trainees in Clinical & Basic Sciences***, Winnipeg, Manitoba, Canada, May 7, 2013 (oral).

H. Sun, S. Pistorius, "Improvements in Image Quality When Using Patient Outline Constraints with a Generalized Scatter PET Reconstruction Algorithm," ***IEEE Nuclear Science Symposium & Medical Imaging Conference (NSS-MIC)***, Anaheim, CA, USA, October 29- November 3, 2012.

H. Sun, S. Pistorius, "A Novel Scatter Enhanced PET Reconstruction Algorithm," ***2012 World Congress on Medical Physics and Biomedical Engineering***, Beijing, China, May 26-31, 2012.

References:

General references:

1. D. L. Bailey, et al., eds., “Positron emission tomography: basic sciences,” ***Springer***, 2005.
2. M. E. Phelps, S. R. Cherry, and M. Dahlbom, “PET: physics, instrumentation, and scanners,” ***Springer***, 2006.

Cited references:

1. D. L. Bailey, et al., eds., “Positron emission tomography: basic sciences,” ***Springer***, 2005.
2. S. Dorbala, et al., “Prognostic value of stress myocardial perfusion positron emission tomography: results from a multicenter observational registry,” ***Journal of the American College of Cardiology***, vol. 61, pp. 176-184, 2013.
3. S. Kim, et al., “PET imaging in pediatric neuroradiology: current and future applications,” ***Pediatr. Radiol***., vol. 40, pp. 82-96, 2010.
4. H. Zaidi and M.-L. Montandon, “Scatter compensation techniques in PET,” ***PET Clin.***, vol. 2, pp. 219-234, 2007.
5. A. Konik, M. T. Madsen and J. J. Sunderland, “GATE simulations of human and small animal PET for determination of scatter fraction as a function of object size,” ***IEEE Trans. Nucl. Sci.***, vol. 57, 2010.
6. B. Guérin and G. El Fakhri, “Novel scatter compensation of list-mode PET data using spatial and energy dependent corrections,” ***IEEE Trans. Med. Imag.***, vol. 30, 2011.
7. D. L. Bailey, “Quantitative procedures in 3D PET,” ***The Theory and Practice of 3D PET***, pp. 55-109, 1998.
8. H. Zaidi and K. F. Koral, “Scatter modelling and compensation in emission tomography,” ***European Journal of Nuclear Medicine and Molecular Imaging***, vol. 31, pp. 761-782, 2004.

9. H. Zaidi, "Scatter modelling and correction strategies in fully 3-D PET," ***Nucl.Med. Commun.***, vol. 22, pp. 1181-1184, 2001.

10. B. Bendriem, R. Trebossen, V. Frouin and A. Syrota, "A PET scatter correction using simultaneous acquisitions with low and high lower energy thresholds," ***IEEE Nuclear Science Symposium and Medical Imaging Conference***, *San Francisco, CA*, pp. 1779-1783, 1993.

11. S. Grootoonk, T. J. Spinks, D. Sashin, N. M. Spyrou and T. Jones, "Correction for scatter in 3D brain PET using a dual energy window method," ***Phys. Med. Bio.***, vol. 41, pp. 2757-2774, 1996.

12. R. L. Harrison, D. R. Haynor and T. K. Lewellen, "Dual energy window scatter corrections for positron emission tomography," ***IEEE Nuclear Science Symposium & Medical Imaging Conference***, *Santa Fe*, pp. 1700-1704, 1992.

13. V. Sossi, J. S. Barney and T. J. Ruth, "Noise reduction in the dual energy window scatter correction approach in 3D PET," ***IEEE Nuclear Science Symposium and Medical Imaging Conference***, *Norfolk, VA, USA*, 1995.

14. L.-E. Adam, J. S. Karp and R. Freifelder, "Scatter correction using a dual energy window technique for 3D PET with NaI(Tl) detectors," ***IEEE Nuclear Science Symposium & Medical Imaging Conference***, *Toronto, Canada*, pp. 2011-2018, 1998.

15. L. Shao, R. Freifelder and J. S. Karp, "Triple energy window scatter correction technique in PET," ***IEEE Trans. Med. Imag.***, vol. 13, pp. 641-648, 1994.

16. M. Bentourkia, P. Msaki, J. Cadorette and R. Lecomte, "Energy dependence of scatter components in multispectral PET imaging," ***IEEE Trans. Med. Imag.***, vol. 14, pp. 138-145, 1995.

17. H. Zaidi, and K. F. Koral, "Scatter correction strategies in emission tomography," ***Quantitative Analysis in Nuclear Medicine Imaging,*** pp.205-235, ***Springer***, 2006.

18. D. L. Bailey and S. R. Meikle, "A convolution-subtraction scatter correction method for 3D PET," ***Phys. Med. Bio.***, vol. 39, pp. 411-424, 1994.

19. C. S. Levin, M. Dahlbom and E. J. Hoffman, "A Monte Carlo correction for the effect of Compton scattering in 3-D pet brain imaging," ***IEEE Trans. Nucl. Sci.***, vol. 42, pp. 1181-1185, 1995.

20. H. Zaidi, A. Herrmann Scheurer, and C. Morel, "An object-oriented Monte Carlo simulator for 3D cylindrical positron tomographs," ***Comput. Meth. Prog. Bio.***, vol. 58, pp. 133-145, 1999.

21. O. Barret, T. A. Carpenter, J. C. Clark, R. E. Ansorge and T. D. Fryer, "Monte Carlo simulation and scatter correction of the GE Advance PET scanner with SimSET and Geant4," ***Phys. Med. Bio.***, vol. 50, pp. 4823-4840, 2005.

22. C.H. Holdsworth, C.S. Levin, T.H. Farquhar, M. Dahlbom, E.J. Hoffman, "Investigation of Accelerated Monte Carlo Techniques for PET Simulation and 3D PET Scatter Correction," ***IEEE Trans. Nucl. Sci.***, vol. 48, pp. 74-81, 2001.

23. C.S. Levin, M. Dahlbom, E.J. Hoffman, "A Monte Carlo correction for the effect of Compton scattering in 3-D PET brain imaging," ***IEEE Trans. Nucl. Sci.***, vol. 42, pp. 1181-1185, 1995.

24. C. C. Watson, D. Newport, M. E. Casey, R. A. deKemp, R. S. Beanlands, and M. Schmand, "Evaluation of Simulation-Based Scatter Correction for 3-D PET Cardiac Imaging," ***IEEE Trans. Nucl. Sci.***, vol. 44, pp. 90-97, 1997.

25. C. C. Watson, "New, Faster, Image-Based Scatter Correction for 3D PET," ***IEEE Trans. Nucl. Sci.***, vol. 47, pp. 1587-1594, 2000.

26. V. Bettinardi, L. Presotto, E. Rapisarda, M. Picchio, L. Gianolli, and M. C. Gilardi, "Physical Performance of the new hybrid PET⁄CT Discovery-690," ***Med. Phys.***, vol. 38, pp. 5394, 2011.

27. M. S Judenhofer, et al., "Simultaneous PET-MRI: a new approach for functional and morphological imaging," ***Nature Medicine***, vol. 14, pp. 459-465, 2008.

28. T. Ido, et al., "Labeled 2-deoxy-D-glucose analogs. ^{18}F-labeled 2-deoxy-2-fluoro-D-glucose, 2-deoxy-2-fluoro-D-mannose and ^{14}C-2-deoxy-2-fluoro-D-glucose," ***Journal of Labelled Compounds and Radiopharmaceuticals,*** vol. 14, pp. 175–183, 2006.

29. M. E. Phelps, S. R. Cherry, and M. Dahlbom, "PET: physics, instrumentation, and scanners," ***Springer***, 2006.

30. P. E. Christian, "Physics of Nuclear Medicine," ***Nuclear medicine and PET/CT: Technology and techniques***, 2007

31. P. Zanzonico, "Positron Emission Tomography: A Review of Basic Principles, Scanner Design and Performance, and Current Systems," ***Seminars in Nuclear Medicine***, vol. XXXIV, pp. 87-111, 2004.

32. S. R. Cherry, J. A. Sorenson and M. E. Phelps, "Physics in nuclear medicine, 2.1.2, 2.1.3.1, 2.3.2, 2.4.2, 2.5, 2.7," Fourth edition, ***Elsevier Inc***., 2003.

33. J. M. Ollinger, "Model-based scatter correction for fully 3D PET," ***Phys. Med. Biol.***, vol. 41, pp.153-176, 1996.

34. A. Kolb, E. Lorenz, M. S. Judenhofer, D. Renker, K. Lankes and B. J. Pichler, "Evaluation of Geiger-mode APDs for PET block detector designs," ***Phys. Med. Biol.,*** vol. 55, pp.1815-1832, 2010.

35. J. S. Karp, et al., "Continuous-Slice PENN-PET: A Positron Tomography with Volume Imaging Capability," ***J. Nucl. Med.***, vol.31, pp. 617-627, 1990.

36. P. K. Hooper, S. R. Meikle, S. Eberl, and M. J. Fulham, "Validation of post injection transmission measurements for attenuation correction in neurologic FDG PET studies," ***J. Nucl. Med.***, vol. 37, pp. 128–136, 1996.

37. C. Burger, G. Goerres, S. Schoenes, A. Buck, A. H. Lonn, and G. K. Von Schulthess, "PET attenuation coefficients from CT images: experimental evaluation of the

transformation of CT into PET 511-keV attenuation coefficients," ***Eur. J. Nucl. Med. Mol. Imaging***, vol. 29, pp. 922-927, 2002.

38. B. K. Navalpakkam, H. Braun, T. Kuwert, and H. H. Quick, "Magnetic Resonance-Based Attenuation Correction for PET/MR Hybrid Imaging Using Continuous Valued Attenuation Maps," ***Investigative Radiology***, vol. 48, pp. 323-332, 2013.

39. K. S. Kim and J. C. Ye, "Fully 3D iterative scatter-corrected OSEM for HRRT PET using a GPU," ***Phys. Med. Biol.***, vol. 56, pp. 4991-5009, 2011.

40. S. R. Cherry, S.-C. Huang, "Effects of Scatter on Model Parameter Estimates in 3D PET Studies of the Human Brain," *IEEE* ***Trans. Nucl. Sci.***, vol. 42, pp.1174-1179, 1995.

41. O. G. Rousset, Y. Ma, A. C. Evan, "Correction for partial volume effects in PET: principle and validation," ***J. Nucl. Med.***, vol. 39, pp. 904-911, 1998.

42. X. Ouyang, W. H. Wong, V. E. Johnson, X. Hu, C.-T. Chen, "Incorporation of correlated structural images in PET images reconstruction," ***IEEE Trans. Med. Imag.***, vol. 13, pp. 627-640, 1994.

43. L. A. Shepp and Y. Vardi, "Maximum likelihood reconstruction for emission tomography," ***IEEE Trans. Med. Imag.***, vol. MI-1, 1982.

44. G. Kontaxakis and L. G. Strauss, "Maximum likelihood algorithms for image reconstruction in Positron Emission Tomography," ***Radionuclides for Oncology - Current Status and Future Aspects***, pp. 73-106, 1998.

45. M. E. Daube-Witherspoon and G. Muehllehner, "Treatment of Axial Data in Three-Dimensional PET," ***J. Nucl. Med.***, vol. 28, pp. 1717-1724, 1987.

46. K. Erlandsson, P. D. Esser, S.-E. Strand and R. L. van Heertum, "3D reconstruction for a multi-ring PET scanner by single-slice rebinning and axial deconvolution," ***Phys. Med. Biol.***, vol. 39, pp. 619-629, 1994.

47. E. Tanaka and Y. Amo, "A Fourier rebinning algorithm incorporating spectral transfer efficiency for 3D PET," ***Phys. Med. Biol.***, vol. 43, pp. 739-746, 1998.

48. R. M. Lewitt, G. Muehllehner and J. S. Karp, “Three-dimensional image reconstruction for PET by multi-slice rebinning and axial image filtering,” ***Phys. Med. Biol.***, vol. 39, pp. 321-339, 1994.

49. M. Defrise, P. E. kinahan, D. W. Townsend, C. Michel, M. Sibomana and D. F. Newport, “Exact and Approximate Rebinning Algorithms for 3-D PET Data,” ***IEEE Trans. Med. Imag.***, vol. 16, pp. 145-158, 1997.

50. S. Basu, H. Zaidi, S. Holm and A. Alavi, “Quantitative techniques in PET-CT imaging,” ***Current Medical Imaging Reviews***, vol. 7, pp. 216-233, 2011.

51. F. J. Beekman, C. Kamphuis and E. C. Frey, “Scatter compensation methods in 3D iterative SPECT reconstruction: A simulation study,” ***Phys. Med. Biol.***, vol. 42, pp. 1619–1632, 1997.

52. M. Tamal, A. J. Reader, P. J. Markiewicz, P. J. Julyan, and D. L. Hastings, “Noise properties of four strategies for incorporation of scatter and attenuation information in PET reconstruction using the EM-ML algorithm,” ***IEEE Trans. Nucl. Sci.***, vol. 53, pp. 2778-2786, 2006.

53. J. Qi, R. M. Leahy, C. Hsu, T. H. Farquhar, and S. R. Cherry, “Fully 3D Bayesian image reconstruction for the ECAT EXACT HR+,” ***IEEE Trans. Nucl. Sci.***, vol. 45, pp. 1096 – 1103, 1998.

54. J. E. Bowsher, V. E. Johnson, T. G. Turkington, R. J. Jaszczak, C. E. Floyd, Jr., and R. Edward Coleman, “Bayesian reconstruction and use of anatomical a priori information for emission tomography,” ***IEEE Trans. Med. Imag.***, vol. 15, pp. 673-686,1996.

55. H. Zaidi, “Relevance of accurate Monte Carlo modeling in nuclear medical imaging,” ***Med. Phys.***, vol. 26, pp. 574-608, 1999.

56. R. Levkovitz, D. Falikman, M. Zibulevsky, A. Ben-Tal, and A. Nemirovski, “The Design and implementation of COSEM, an iterative algorithm for fully 3-D list mode data,” ***IEEE Trans. Med. Imag.***, vol. 20, pp. 633-642, 2001.

57. H. T. Chen, C.-M. Kao and C. T. Chen, "A fast, energy-dependent scatter reduction method for 3D-PET imaging," ***IEEE Nuclear Science Symposium & Medical Imaging Conference***, pp. 2630-2634, 2003.

58. L. M. Popescu, R. M. Lewitt, S. Matej, and J. S. Karp, "PET energy-based scatter estimation and image reconstruction with energy-dependent corrections," ***Phys. Med. Biol.***, vol. 51, pp. 2919-2937, 2006.

59. L. M. Popescu, "PET energy-based scatter estimation in the presence of randoms, and image reconstruction with energy-dependent scatter and randoms corrections," ***IEEE Trans. Nucl. Sci.***, vol. 59, pp. 1958-1966, 2012.

60. M. Conti, I. Hong, and C. Michel, "Reconstruction of scattered and unscattered PET coincidences using TOF and energy information," ***Phys. Med. Biol.***, vol. 57, pp. N307-317, 2012.

61. M. Conti, "Why is TOF PET reconstruction a more robust method in the presence of inconsistent data?," ***Phys. Med. Biol.***, vol. 56, pp. 155-168, 2011.

62. H. Sun and S. Pistorius, "A novel scatter enhanced PET reconstruction algorithm," ***World Congress Medical Physical and Biomedical Engineering***, Beijing, 2012.

63. H. Zaidi, M.-L. Montandon, and S. Meikle, "Strategies for attenuation compensation in neurological PET studies," ***NeuroImage***, vol. 34, pp. 518-541, 2007.

64. E. V. Uytven, S. Pistorius, and R. Gordon, "An iterative three-dimensional electron density imaging algorithm using uncollimated Compton scattered x-rays from a polyenergetic primary pencil beam," ***Med. Phys.***, vol. 34, pp. 256-265, 2007.

65. C. Byrne, "Likelihood Maximization for List-Mode Emission Tomographic Image Reconstruction," ***IEEE Trans. Med. Imag.***, vol. 20, 2001.

66. GATE: Simulations of Preclinical and Clinical Scans in Emission Tomography, Transmission Tomography and Radiation Therapy, January 02, 2011; Available at: http://www.opengatecollaboration.org/

67. S. Jan et al., "GATE: A simulation toolkit for PET and SPECT," ***Phys. Med. Biol.***, vol. 49, 2004.

68. K. Assie et al., "Monte Carlo simulation in PET and SPECT instrumentation using GATE," ***Nuclear Instruments and Methods in Physics Research Section A: Accelerators, Spectrometers, Detectors and Associated Equipment***, vol. 527, pp. 180-189, 2004.

69. R. J. Jaszczak, K. L. Greer, C. E. Floyd, Jr., C. C. Harris and R. E. Coleman, "Improved SPECT quantification using compensation for scattered photons," ***The Journal of Nuclear Medicine***, vol. 25, pp. 893-900,1984.

70. Jaszczak Phantoms, *May 06, 2011; Available at:* *http://www.spect.com/pub/Flanged_Jaszczak_Phantoms.pdf*

71. H. Sun and S. Pistorius, "Evaluation of image quality improvements when adding patient outline constraints into a Generalized Scatter PET reconstruction algorithm," ***ISRN Biomedical Imaging***, 2013.

72. H. Sun, S. Pistorius, "Improvement in image quality when using patient outline constraints within a Generalized Scatter PET reconstruction algorithm," ***IEEE Nuclear Science Symposium & Medical Imaging Conference***, Anaheim, USA, 2012.

73. H. Sun and S. Pistorius, "Evaluation of the feasibility and quantitative accuracy of a Generalized Scatter 2D PET reconstruction method," ***ISRN Biomedical Imaging***, 2013.

74. Y. Yang, S. R. Cherry, "Observations Regarding Scatter Fraction and NEC Measurements for Small Animal PET," ***IEEE Trans. Nucl. Sci.***, vol. 53, pp.127-132, 2006.

75. L.-T. Chang, "A method for attenuation correction in radionuclide Computed Tomography," ***IEEE Trans. Nucl. Sci.***, vol. NS-25, pp.638-643, 1978.

76. S. Pistorius, H. Sun, "Systems and Methods for Improving the Quality of Images in a PET Scan," United States Patent Granted, No.: US-8866087, Date of Publication: Jun 12, 2014.

77. H. Zaidi, M.-L. Montandon, and A. Alavi, "Advances in Attenuation Correction Techniques in PET," ***PET Clinics***, vol. 2, pp. 191-217, 2007.

78. J. Nuyts, G. Bal, F. Kehren, M. Fenchel, C. Michel, and C. Watson, "Completion of a Truncated Attenuation Image from the Attenuated PET Emission Data," ***IEEE Trans. Med. Imag.***, vol. 32, pp.237-246, 2013.

79. A. Werling, O. Bublitz, J. Doll, L.-E. Adam and G. Brix, "Fast implementation of the single scatter simulation algorithm and its use in iterative image reconstruction of PET data," ***Phys. Med. Biol***., vol. 47, pp. 2947-2960, 2002.

80. J. H. Hubbell, S. M. Seltzer, "Tables of X-ray mass attenuation coefficients and mass energy-absorption coefficients from 1 keV to 20 MeV for elements Z=1 to 92 and 48 additional substances of dosimetric interest," ***The National Institute of Standards and Technology (NIST)***, 2004.

81. K. Kitamura, K. Tanaka, T. Sato, "Implementation of continuous 3D whole-body PET scanning using on-the-fly Fourier rebinning," ***Phys. Med. Biol.***, vol. 47, pp. 2705-2712, 2002.

82. N. E. M. Association, "NEMA standards publication NU2-2012: Performance measurements of Positron Emission Tomographs (PETs)," Rosslyn, VA, USA, 2012

83. A. A. Wagadarikar, A. Ivan, S. Dolinsky, and D. L. McDaniel, "Sensitivity Improvement of Time-of-Flight (ToF) PET Detector Through Recovery of Compton Scattered Annihilation Photons," ***IEEE Trans. Nucl. Sci.***, vol. 61, pp. 121-125, 2014.

84. I. G. Kazantsev, S. Matej, R. L. Lewitt "Geometric model of single scatter in PET," ***IEEE Nuclear Science Symposium & Medical Imaging Conference Record***, M11-334, 2006.

85. M. I. Freedenberg, R. D. Badawi, A. F. Tarantal, S. R. Cherry, "Performance and limitations of positron emission tomography (PET) scanners for imaging very low activity sources," ***Physics Media***, vol. 30, 2014.

86. B. W. Jakoby, Y. Bercier, M. Conti, M. Casey, T. Gremillion, C. Hayden, B. Bendriem, D. W. Townsend, "Performance Investigation of a Time-of-Flight PET/CT Scanner," ***IEEE Nuclear Science Symposium & Medical Imaging Conference Record***, M06-39, 2008.

87. S. Surti, A. Kuhn, M. E. Werner, A. E. Perkins, J. Kolthammer, and J. S. Karp, "Performance of Philips Gemini TF PET/CT Scanner with Special Consideration for Its Time-of-Flight Imaging Capabilities," ***J. Nucl. Med.***, vol. 48, pp. 471-480, 2007.

88. M. E. Daube-Witherspoon, S. Surti, A. Perkins, C. C. M. Kyba, R. Wiener, M. E. Werner, R. Kulp, and J. S. Karp, "The imaging performance of a LaBr3-based PET scanner," ***Phys. Med. Biol***, vol. 55, pp. 45-64, 2010.

89. Y. Morimoto, Y. Ueno, W. Takeuchi, S. Kojima, K. Matsuzaki, T. Ishitsu, K. Umegaki, Y. Kiyanagi, N. Kubo, C. Katoh, T. Shiga, H. Shirato, and N. Tamaki, "Development of a 3D Brain PET Scanner Using CdTe Semiconductor Detectors and Its First Clinical Application," ***IEEE Trans. Nucl. Sci.***, vol. 58, pp. 2181-2189, 2011.

90. T. Shiga, Y. Morimoto, N. Kubo, N. Katoh, C. Katoh, W. Takeuchi, R. Usui, K. Hirata, S. Kojima, K. Umegaki, H. Shirato, and N. Tamaki, "A New PET Scanner with Semiconductor Detectors Enables Better Identification of Intratumoral Inhomogeneity," ***J. Nucl. Med.***, vol. 50, pp.148-155, 2009.

91. E. Mikhaylova, G. D. Lorenzo, M. Chmeissani, M. Kolstein, M. Cañadas, P. Arce, Y. Calderón, D. Uzun, G. Ariño, J. G. Macias-Montero, R. Martinez, C. Puigdengoles, and E. Cabruja, "Simulation of the Expected Performance of a Seamless Scanner for Brain PET Based on Highly Pixelated CdTe Detectors," ***IEEE Trans. Med. Imag.***, vol. 33, pp. 332-339, 2014.

92. F. Lamare, A. Turzo, Y. Bizais, C. C. L. Rest, and D. Visvikis, “Validation of a Monte Carlo simulation of the Philips Allegro/GEMINI PET systems using GATE,” ***Phys. Med. Biol.***, vol. 51, pp. 943-962, 2006.

93. T. Ye, P. Chai, J. Gao, M.-K. Yun, S.-Q. Liu, B.-C. Shan, and L. Wei, “Investigation of scatter from out of the field of view and multiple scatter in PET using Monte Carlo simulations,” ***Chinese Physics C***, vol. 35, pp. 1166-1171, 2011.

94. E. Yoshida, H. Tashima, T. Yamaya, “Sensitivity booster for DOI-PET scanner by utilizing Compton scattering events between detector blocks,” ***Nuclear Instruments and Methods in Physics Research A***, vol. 763, pp. 502-509, 2014.

95. Y. Shao, Si. R. Cherry, S. Siegel, R. W. Silverman, “A Study of Inter-Crystal Scatter in Small Scintillator Arrays Designed for High Resolution PET Imaging,” ***IEEE Trans. Nucl. Sci.***, vol. 43, pp.1938-1944, 1996.

96. K. A. Comanor, P.R. G. Virador and W. W. Moses, “Algorithms to Identify Detector Compton Scatter in PET Modules,” ***IEEE Trans. Nucl. Sci.***, vol. 43, pp. 2213-2218, 1996.

97. M. Rafecas, G. Boning, B. J. Pichler, E. Lorenz, M. Schwaiger and S. I. Ziegler, “Inter-crystal scatter in a dual layer, high resolution LSO-APD positron emission tomograph,” ***Phys. Med. Biol.***, vol. 48, pp. 821-848, 2003.

98. C. Buchbender, V. Hartung-Knemeyer, M Forsting, G Antoch, T. A Heusner, “Positron emission tomography (PET) attenuation correction artefacts in PET/CT and PET/MRI,” ***Br. J. Radiol.***, 2013.

99. J. E. Alpuche Aviles, S. Pistorius, R. Gordon and I. A. Elbakri, “A novel hybrid reconstruction algorithm for first generation incoherent scatter CT (ISCT) of large objects with potential medical imaging applications,” ***Journal of X-Ray Science and Technology***, vol. 18, pp.1-22, 2010.

100. J. E. Alpuche Aviles, S. Pistorius, “A 1st generation scatter CT algorithm for electron density breast imaging which accounts for bound incoherent, coherent and multiple scatter: A Monte Carlo study,” ***Journal of X-Ray Science and Technology***, vol.19, pp. 477-499, 2011.

101. R. Masuji, K. Watanabe, A. Yamazaki, and A. Uritani, “A study on electron density imaging using the Compton scattered X-ray CT technique,” ***Nuclear Instruments and Methods in Physics Research Section A: Accelerators, Spectrometers, Detectors and Associated Equipment***, vol. 652, pp. 620-624, 2011.

102. G. Zhang, H. Sun, S. Pistorius, “Feasibility of Scatter Based Electron Density Reconstruction for Attenuation Correction in Positron Emission Tomography,” ***IEEE Nuclear Science Symposium & Medical Imaging Conference***, Seattle, 2014.